Aquaporin-1 sustains lymphangiogenic responses in hyperosmotic inflammatory microenvironments

Irena Roci[1], Jaeryung Kim[1#&], Kelly de Korodi[1&], Tania Wyss[1], Jeremiah Bernier-Latmani[1], Silvia Arroz-Madeira[1#], Alejandra González-Loyola[1#], Esther Bovay[1#], Nadia Grenningloh[1#], Hans Schoofs[2#], Noo Li Jeon[3,4], Costanza Giampietro[5,6], Taija Mäkinen[2,7,8], Agnès Noël[9,10], Tatiana V. Petrova[1,11]*

[1] Department of Fundamental Oncology, University of Lausanne, and Ludwig Institute for Cancer Research Lausanne, CH-1066 Epalinges, Switzerland.
[2] Department of Immunology, Genetics and Pathology, Uppsala University, Uppsala, Sweden.
[3] Department of Mechanical Engineering, Seoul National University, Seoul, Republic of Korea.
[4] Institute of Advanced Machinery and Design, Seoul National University, Seoul, Republic of Korea
[5] Department of Mechanical and Process Engineering, ETH Zurich, Zurich, Switzerland.
[6] Swiss Federal Laboratories for Materials Science and Technology, Dübendorf, Switzerland.
[7] Wihuri Research Institute, Biomedicum Helsinki, Helsinki, Finland.
[8] Faculty of Medicine, University of Helsinki, Helsinki, Finland.
[9] Laboratory of Tumor and Development Biology, GIGA, University of Liège (ULiège), Sart-Tilman, 4000 Liège, Belgium
[10] WELBIO Department, WEL Research Institute, Avenue Pasteur, 6, 1300 Wavre, Belgium
[11] Swiss Institute for Experimental Cancer Research (ISREC), School of Life Sciences, École Polytechnique Fédérale de Lausanne (EPFL), CH-1015 Lausanne, Switzerland.

[#] Current address: Jaeryung Kim, Department of Ophthalmology, Samsung Medical Center, Sungkyunkwan University School of Medicine, Seoul, Republic of Korea; Silvia Arroz-Madeira, Católica Biomedical Research Centre, Universidade Católica Portuguesa, Oeiras, Portugal; Alejandra González-Loyola, Aragon Health Research Institute, (IISA) Zaragoza, Spain; Aragonese Agency Foundation for Research and Development (ARAID), Zaragoza, Spain; Esther Bovay, Max Planck Institute for Molecular Biomedicine, Department of Tissue Morphogenesis, D-48149 Münster, Germany; Nadia Grenningloh, Institute of Bioengineering, School of Life Sciences, Ecole Polytechnique Fédérale de Lausanne (EPFL), Lausanne, Switzerland; Hans Schoofs, Division of Molecular Pathology, Oncode Institute, The Netherlands Cancer Institute, Plesmanlaan 121, 1066 CX Amsterdam, the Netherlands.

[&] Contributed equally.

*Corresponding author: Tatiana V. Petrova, Department of Oncology, Ludwig Institute for Cancer Research Lausanne and University of Lausanne, Chemin des Boveresses 155, CH-1066 Epalinges, Switzerland. Phone: +41 21 314 2968; E-mail: tatiana.petrova@unil.ch

Abstract

Intestinal lymphatic vessels are essential for dietary lipid absorption and immune cell trafficking. Villus lymphatic capillaries, lacteals, undergo continuous VEGF-C–dependent renewal to function in a hyperosmolar, inflammatory environment exposed to dietary and microbial by-products. To define mechanisms underlying this adaptation, we integrated new and published single-cell RNA-sequencing datasets of murine small-intestinal lymphatic endothelial cells (LECs). Lacteal LECs resembled *Ptx3*$^{+}$ immune-interacting LECs and were characterized by high expression of water channel AQP1. LEC-

specific *Aqp1* deletion reduced lacteal length, impaired lipid uptake, and limited weight gain on a high-fat diet, while mosaic deletion revealed a cell-autonomous requirement for AQP1 in LEC positioning at hyperosmolar tip regions. AQP1 promoted LEC migration under hyperosmotic stress by preserving cytoskeletal and junctional remodeling and alleviating osmotic stress-induced transcriptional programs. AQP1 was upregulated during inflammatory remodeling in lymphedema and lymphatic malformations, but not during embryonic lymphangiogenesis. These findings link lacteal regeneration to inflammatory lymphatic remodeling and highlight tissue osmolarity as a biophysical determinant of postnatal lymphangiogenesis.

Keywords: AQP1, lacteals, osmotic stress, lymphangiogenesis, *Ptx3*+ LECs, lymphedema, lymphatic malformation

Running title: AQP1 sustains stress-adaptive lymphangiogenesis

Non-standard abbreviations: **AQP1**, aquaporin-1; **AQP1^{OE}**, AQP1-overexpressing; **BRB-seq**, bulk RNA barcoding and sequencing; **EBFP**, enhanced blue fluorescent protein; **EBM-2**, endothelial basal medium-2; **EC**, endothelial cells; **EYFP**, enhanced yellow fluorescent protein; **FDR**, false discovery rate; **GEO**, Gene Expression Omnibus; **GO**, gene ontology; **HFD**, high-fat diet; **JAIL**, junction-associated intermittent lamellipodia; **LD**, lymphedema; **LEC**, lymphatic endothelial cell; **NCD**, normal chow diet; PI3K, phosphoinositide 3-kinase; **PLA**, proximity ligation assay; **RPMI**, Roswell Park Memorial Institute medium; **RT-qPCR**, quantitative real-time PCR; **SCENIC**, single-cell regulatory network inference and clustering; **scRNA-seq**, single-cell RNA sequencing; **TG**, triglyceride; **UMAP**, uniform manifold approximation and projection; **UMI**, unique molecular identifier; **VEGF-C**, vascular endothelial growth factor C; **VEGFR3**, VEGF receptor 3; **VPT**, Vascular Phenotypic and Proteomic

Introduction

The lymphatic vascular system plays a crucial role in fluid homeostasis, lipid absorption, and immune surveillance (Petrova and Koh, 2018; Ulvmar and Mäkinen, 2016; Oliver et al., 2020). Interstitial fluid and immune cells are first taken up by blind-ended lymphatic capillaries, from which lymph is transported through valved collecting vessels to lymph nodes and eventually returned to the bloodstream. Recent single-cell RNA sequencing (scRNA-seq) studies have revealed distinct molecular profiles of capillary, pre-collecting, and valve lymphatic endothelial cells (LECs), reflecting their functional specialization (Norrmén et al., 2010; Petkova et al., 2023; Xiang et al., 2020; González-Loyola et al., 2021). Similarly, blood endothelial cells (ECs) exhibit transcriptional heterogeneity reflecting their functions into arteries, veins, and capillaries. Additionally, multiple organ-specific blood EC subsets, such as blood-brain barrier ECs, liver sinusoidal ECs, lung aerocytes, and lipid-processing ECs, have been described (Augustin and Koh, 2017; Geldhof et al., 2022). However, while lymph node

LECs display notable specialization (Xiang et al., 2020; Takeda et al., 2019; Fujimoto et al., 2020), LECs across different organs, including the small intestine, appear to be more homogeneous than blood ECs (Kalucka et al., 2020; Trimm and Red-Horse, 2023).

The primary functions of small intestinal lymphatics include dietary lipid absorption and regulation of immune responses to gut microbiota and dietary antigens (Bernier-Latmani and Petrova, 2017; Bernier-Latmani et al., 2024). Lacteals, the lymphatic capillaries located in small intestinal villi, serve as the main sites of dietary lipid uptake. Unlike other adult lymphatic vessels, lacteal LECs maintain a pro-lymphangiogenic phenotype (Bernier-Latmani et al., 2015; Nurmi et al., 2015) in a hyperosmolar microenvironment, with villus tip osmolarity reaching ~600 mOsm during nutrient absorption (Hallbäck et al., 1991). During fat absorption, chylomicron accumulation and increased solute concentration generate osmotic gradients that acutely alter lacteal junction configuration (Zarkada et al., 2023). Following absorption, lymph is transported through submucosal vessels to the mesenteric collecting vessels for systemic distribution. Beyond their role in nutrient transport, LECs from crypt-associated lymphatic vessels secrete factors such as R-SPONDIN-3 and reelin, which promote intestinal stem cells and intestinal regeneration upon injury (Goto et al., 2022; Palikuqi et al., 2022; Niec et al., 2022).

Although these findings highlight intestinal lymphatics as critical for lipid uptake and tissue repair, the adaptation of lacteals to the distinct, high-osmolarity (Hallbäck et al., 1991) and hypoxic (Singhal and Shah, 2020) environment of small intestinal villi has yet to be fully explored. Therefore, we aimed to refine the characterization of murine intestinal LECs by integrating scRNA-seq data from new and published datasets. Our results reveal a distinct transcriptional program distinguishing lacteal from submucosal and serosal intestinal LECs and show that lacteals closely resemble a recently identified subset of *Ptx3*$^{+}$ immune-interacting LECs (Petkova et al., 2023). We identify *Aqp1,* encoding a highly conserved water channel (Agre et al., 1993, 2002), as a member of the *Ptx3*$^{+}$ gene signature and demonstrate that AQP1 is necessary for lacteal maintenance and efficient dietary lipid uptake. Using mosaic deletion, we show that AQP1 is required cell-autonomously for LECs to occupy high-osmolarity lacteal tip positions. We explore the regulatory mechanisms controlling AQP1 expression, including its modulation by VEGFR3 signaling and microbial cues, and demonstrate that AQP1 facilitates junctional and cytoskeletal remodeling, rescuing hyperosmotic stress-induced junctional tightening and transcriptional programs. We further examine AQP1 expression during development and under inflammatory conditions, such as in lymphatic malformations, immunization and lymphedema, revealing that AQP1 expression distinguishes stress-adaptive from embryonic lymphangiogenesis. Altogether, our findings establish AQP1 as a mediator of stress-adaptive lymphatic remodeling, connect lacteal regeneration to inflammatory remodeling of the lymphatic vasculature and highlight tissue osmolarity as a key biophysical factor in postnatal lymphangiogenesis.

Results

Characterization of small intestinal LEC subsets

To explore the heterogeneity of LECs in the mouse small intestine, we conducted an integrated scRNA-seq analysis by combining datasets from our current study (samples 1-5) and three published datasets (samples 6-8) (Kalucka et al., 2020; Niec et al., 2022; Wiggins et al., 2023)(Fig. 1A and Table S1). We identified 6802 LECs based on the expression of the pan-endothelial marker *Pecam1*, lymphatic markers *Prox1* and *Vegfr3* (*Flt4*), and the absence of the blood endothelial marker *Flt1* (Tacconi et al., 2021). Visualization of the integrated intestinal LEC datasets using Uniform Manifold Approximation and Projection (UMAP) revealed a single, continuous grouping of cells, indicating overall transcriptional similarity (Fig. S1A). However, unsupervised clustering separated the cells into three subclusters, revealing underlying heterogeneity within this population (Fig. 1B). Among the cluster defining markers, Cluster 0 showed elevated expression of *Aqp1*, *Fabp4*, and *Itih5*; Cluster 1 was enriched for *Clca3a1*, *Fxyd6*, and *Klhl4*; and Cluster 2 displayed higher levels of *Isg15*, *Itih3*, and *Irf7* (Fig. 1C, Table S1).

To validate scRNA-seq analyses and spatially localize the identified clusters, we performed immunofluorescence staining on small intestine tissues. AQP1 was highly expressed in lacteal LECs with low to no expression in submucosal and serosal LECs (Fig. 1D and Fig. S1B), consistent with previous findings (Nielsen et al., 1993; Gannon and Carati, 2003; Ma et al., 2001). In addition, fatty acid-binding protein 4 (FABP4), associated with lipid transport and metabolism (Furuhashi and Hotamisligil, 2008), was prominently expressed in lacteal LECs and neighboring LYVE1^{-} blood vessels, while staining was almost absent in submucosal LECs (Fig. 1E). In contrast, calcium-activated chloride channel regulator 3A-1 (CLCA3A1, formerly mCLCA1) implicated in Ca^{2+}-dependent chloride conductance and leukocyte adhesion and migration (Sala-Rabanal et al., 2015; Gandhi et al., 1998; Furuya et al., 2010), was strongly expressed in serosal LECs and sporadically detected in submucosal LECs, but not in lacteal LECs (Fig. 1F). Based on these spatial expression patterns and prior anatomical characterizations (Unthank and Bohlen, 1988; Bernier-Latmani et al., 2015), we designated Cluster 0 as lacteal LECs and Cluster 1 as submucosal and serosal (S/S) LECs (Fig. 1G). Cluster 2 was characterized by increased expression of interferon-stimulated genes, suggesting a role in immune response. Both lacteal and S/S markers were moderately expressed in these IFN cluster cells (Fig. 1C), raising the possibility that tissue-processing stress upregulated interferon signaling transcripts. We therefore removed IFN markers (Fig. 1C) and performed a new clustering analysis, which yielded two clusters, with former IFN cluster cells redistributing to cluster 0 or 1, while retaining expression of their original cluster markers (Fig. S1, C and D). scRNA-seq data from Wiggins et al. (Wiggins et al., 2023) identified four LEC clusters (LEC1, LEC2a, LEC2b, and IFN; spatial localization undetermined), with only the IFN cluster showing transcriptional similarity to our IFN LECs (Fig. 1A,

Table S1). Differences from Wiggins et al. likely stem from methodological factors: LEC-only versus LEC/BEC clustering, clustering parameters, and sample size (839 versus 6802 cells from 1 versus 8 mice). Taken together, our results reveal defining transcriptional profiles and spatial organization among intestinal LECs subpopulations.

To characterize the functional roles of gut LEC subsets, we performed overrepresentation analysis of Gene Ontology (GO) pathways (Fig. S1E, Table S1). Lacteal LECs were enriched in gene sets associated with cytoskeleton organization, growth factor responses and cell migration, consistent with previous studies showing continuous lacteal regeneration (Bernier-Latmani et al., 2015; Nurmi et al., 2015). S/S LECs showed enrichment for RNA processing and translation, suggesting increased protein synthesis requirements. Exposure to higher mechanical stress in the submucosal and muscularis layers (Egorov et al., 2002) potentially drives enhanced protein synthesis to preserve vessel integrity. As expected, IFN LECs were enriched for pathways associated with immune responses and viral defense mechanisms.

In addition, we employed SCENIC (Aibar et al., 2017), a bioinformatics pipeline based on co-expression and motif enrichment, to evaluate transcription factor activity in the LEC subsets. Lacteal LECs displayed higher activity of SOX4, MXD4, NR2F2 (COUP-TFII), HEYL, IRF8, and HMG20b, although only *Sox4*, *Mxd4*, and *Nr2f2* transcripts were clearly detected in lacteal LECs (Fig. S1, F and G, Table S1). NR2F2 is essential for initiating and maintaining *Prox1* expression during LEC specification (Srinivasan et al., 2010), while SOX4 and MXD4 have not been previously linked to lymphatic development or function. S/S LECs were enriched in regulons of FOXC1, FOXC2, FOXP1, FOXP2, TBX1, EBF1, and FOXN3 (Fig. S1F), while expression of *Foxp1*, *Foxp2*, *Tbx1*, and *Ebf1* was also higher in this subset (Fig. S1F, Table S1). FOXC1/2, FOXP2, and TBX1 control collecting lymphatic vessel development and function (Norden et al., 2020; Hernández Vásquez et al., 2021; Chen et al., 2010), suggesting a transcriptional similarity of S/S LECs with pre-collecting and collecting lymphatics. Finally, IFN LECs displayed enrichment of regulons for key interferon response transcription factors (Fig. S1, F and G) (Platanitis et al., 2019). Overall, these analyses confirm the specialized identities of the gut LEC subsets.

All gut LECs express LYVE1 and lack SMC coverage, suggesting they are lymphatic capillaries (Schulte-Merker et al., 2011). However, lacteal and S/S LECs display distinct transcriptional characteristics. To compare transcriptomes of intestinal LECs and those of other organs, we examined cluster-specific markers of intestinal LECs with those in dermal (Petkova et al., 2023), lymph node (Xiang et al., 2020), and mesenteric LECs (González-Loyola et al., 2021) (Fig. 1H). S/S LECs most closely resembled collecting and capillary dermal LECs; pre-collecting, valve, and proliferating mesenteric LECs; and ceiling lymph node LECs (Fig. 1H), which originate from afferent collecting lymphatic vessels (Bovay et al., 2018). These findings reinforce the idea that submucosal lymphatics are pre-collectors. In contrast, lacteal LECs matched capillary LECs from the mesentery, but showed

closer alignment with *Ptx3*$^{+}$ capillary LECs, a subset found in inflamed skin and non-inflamed LNs (Petkova et al., 2023; Xiang et al., 2020), rather than non-inflamed *Ptx3*$^{-}$ capillaries from these organs (Fig. 1H). The lacteal signature encompassed genes specific to *Ptx3*$^{+}$ LECs including *Itih5, Mrc1, Igfbp4, Aqp1, Ccnd2, Stab1, Mest, Tspan18* (Table S1). *Mrc1* and *Aqp1* were also identified as top markers of *Ptx3*+ lung LECs (Fernandes et al., 2025). Notably, *Ptx3* was expressed in lacteal LECs, although it did not appear among the top genes because its expression was confined to a minor subset (likely tip LECs, Fig. S1H), which can be overlooked in scRNA-seq analysis (Sibler et al., 2021; Xiang et al., 2020). Altogether, these results show that intestinal LECs comprise two main populations: 1) lacteal LECs in villi, which are transcriptionally similar to *Ptx3*$^{+}$ immune-interacting LECs, and 2) S/S LECs that display transcriptional signatures of pre-collector lymphatics.

AQP1 promotes lacteal maintenance and dietary lipid uptake

Among genes enriched in lacteal LECs, *Aqp1* ranked as one of the most defining markers (Fig. 1C). AQP1 is a tetrameric integral membrane protein in which each monomer serves as an osmotically driven, water-selective pore (Agre et al., 1993). Although extensively studied in the kidney epithelial cells, AQP1 is also expressed in multiple other cell types (Agre et al., 2002), including blood ECs, where it regulates angiogenic sprouting, cell migration, and permeability, particularly in response to osmotic stress (Saadoun et al., 2005; Carter et al., 1998; Kondrychyn et al., 2025). Lacteals must sustain their pro-lymphangiogenic phenotype (Bernier-Latmani et al., 2015; Nurmi et al., 2015) in an osmotically challenging environment (Hallbäck et al., 1991). Given the established role of AQP1 in angiogenesis and its exclusive expression among aquaporins in lacteal LECs (Table S1), we hypothesized that AQP1 is essential for lacteal function. Consistently, AQP1 was expressed in lacteals throughout all regions of the small intestine (Fig. S2A), with significantly higher levels at the lacteal tip compared to the base (Fig. 2A). In contrast, lymphatic vessels in the colon, where bulk water absorption occurs but villus architecture and steep osmotic gradients are absent, showed no detectable AQP1 expression (Fig. S2B).

To directly assess the functional role of AQP1 in lacteal physiology, we generated a conditional knockout mouse model (*Aqp1*$^{i\Delta LEC}$) by crossing *Aqp1*$^{fl/fl}$ mice (Zhang et al., 2016), in which exons 2 and 3 of *Aqp1* are flanked by loxP sites, with *Prox1-CreERT2* mice (Bazigou et al., 2011), enabling tamoxifen-inducible LEC-specific deletion of *Aqp1* (Fig. 2B). Immunofluorescence staining showed a marked reduction of AQP1 in lacteal LECs of *Aqp1*$^{i\Delta LEC}$ mice (Fig. 2C), validating the deletion. Scattered AQP1-positive puncta 3-4 μm in size appeared along the lacteals of *Aqp1*$^{i\Delta LEC}$ mice, although their origin and significance remain unclear. We also confirmed efficient *Aqp1* deletion at the mRNA level by isolating LECs from the small intestine using fluorescence-activated cell sorting (FACS) and performing quantitative PCR targeting exons 2 and 3 of *Aqp1* (Fig. S2, C and D).

To assess the impact of *Aqp1* deletion on lacteal morphology, we measured the relative lacteal length, calculated as the ratio of lacteal length to blood vessel length within the same villus. The distribution of relative lacteal length intervals revealed a significant shift toward shorter lacteals in $Aqp1^{i\Delta LEC}$ mice (Fig. 2D). These findings indicate that *Aqp1* is essential for maintaining normal lacteal length. To assess whether other lacteal markers were affected, we examined PTX3 and FABP4. Expression of PTX3 was preserved, while the intracellular fatty acid transporter FABP4 (Furuhashi and Hotamisligil, 2008) was reduced ~50% (Fig. S2, E-H). As PTX3 is a secreted protein, we verified lacteal origin by re-analyzing published scRNA-seq data of lamina propria stromal cells (Fig. S2I) (Bernier-Latmani et al., 2022) and published bulk RNA-seq of intestinal epithelium (Fig. S2J) (González-Loyola et al., 2022), and found no *Ptx3* expression in either.

To determine if lacteal function is hampered by loss of *Aqp1* we performed lipid tolerance tests in control and $Aqp1^{i\Delta LEC}$ mice. We measured serum triglyceride (TG) levels over time following oral administration of a bolus of olive oil (Fig. 2E). $Aqp1^{i\Delta LEC}$ mice showed significantly lower serum TG levels at two hours post-gavage compared to controls (Fig. 2E), suggesting impaired uptake of dietary lipids. To eliminate confounding effects from differential peripheral TG clearance, we performed lipid absorption assays in the presence of the lipoprotein lipase inhibitor Tyloxapol (Fig. 2F). Under these conditions, plasma TG levels reflect chylomicron entry from lacteals into circulation, independent of peripheral metabolism. $Aqp1^{i\Delta LEC}$ mice showed 1.6-fold lower plasma TG at 2 hours and 4.4-fold lower at 3 hours post-gavage (Fig. 2F), establishing that reduced lipid absorption in $Aqp1^{i\Delta LEC}$ mice results from reduced chylomicron entry into the lymphatic system rather than altered peripheral metabolism.

To assess chronic consequences of lymphatic *Aqp1* deficiency, we subjected mice to a high-fat diet (HFD) for three weeks (Fig. 2G). Under standard diet, body weight was comparable between control and $Aqp1^{i\Delta LEC}$ mice. However, under HFD, $Aqp1^{i\Delta LEC}$ mice exhibited significantly reduced weight gain compared to controls (Fig. 2G). This metabolic phenotype is consistent with reduced chylomicron uptake resulting from shortened lacteal length. Thus, AQP1 is required for lacteal maintenance and efficient lipid absorption.

Lacteal AQP1 is induced by microbiota and VEGFR3 signaling

To elucidate the mechanisms regulating *Aqp1* expression in LECs, we investigated its expression during early postnatal development when lymphatic vessels actively sprout and migrate in a VEGF-C/VEGFR3-dependent manner to form lacteals (Tammela et al., 2008; Kim, Sung and Koh, 2007). At P1 AQP1 expression in lacteals was low, sporadic and predominantly confined to the lacteal base (Fig. 3A and B). As development progressed, AQP1 expression extended along the lacteal, with a marked increase at the tip by P5, resembling the spatial distribution observed in adult mice (Fig. 3, A and B). These findings suggest that AQP1 expression in LECs is closely linked to postnatal intestinal

maturation, possibly reflecting enhanced functional requirements for lipid absorption as the neonatal gut transitions to enteral feeding (Knight et al., 1986). This transition coincides with the onset of intestinal colonization, when the bacterial load increases dramatically in the first days of the postnatal period (Hasegawa et al., 2010). To assess whether microbial signals modulate AQP1 expression, we treated mice with broad-spectrum antibiotics. AQP1 expression in lacteals was significantly reduced in antibiotic-treated mice (Fig. 3, C and D), while lymphatic LYVE1 staining was unchanged. These data indicate that microbial cues directly or indirectly contribute to the upregulation of AQP1 in lacteal LECs. Lacteal length and FABP4 expression were unaffected by antibiotic treatment (Fig. S3, A-F), while PTX3 showed a trend toward reduction (Fig. S3F), indicating selective effects on AQP1 rather than global disruption of lacteal identity.

VEGF-C/VEGFR3 signaling drives the postnatal expansion of lacteals and their maintenance in adults (Bernier-Latmani et al., 2015; Nurmi et al., 2015; Tammela et al., 2008). To investigate whether VEGFR3 signaling regulates AQP1 expression in lacteal LECs we administered control IgG or VEGFR3-blocking antibodies (mF4-31C1) (Pytowski et al., 2005) to mice at P4, P6, and P8 and analyzed AQP1 expression at P10 (Fig. 3E). As expected, the treatment stunted postnatal lacteal expansion. In addition, mice treated with mF4-31C1 exhibited a significant reduction in AQP1 expression in remaining lacteals compared to IgG2a-treated controls (Fig. 3F), while VEGFR3 staining increased, likely due to decreased internalization (Deng et al., 2015). Collectively, these findings demonstrate that both microbial colonization and VEGFR3 signaling contribute to AQP1 expression in lacteals.

AQP1 enhances VEGF-C-induced LEC migration under osmotic stress

AQP1 is enriched at the lacteal tip where osmolarity is nearly twice that of the normosmotic villus base and undergoes further fluctuations during nutrient absorption (Hallbäck et al., 1991). To test whether AQP1 enables LEC migration under osmotic stress we employed *in vitro* functional assays using *AQP1*-overexpressing cells. We generated *AQP1*-overexpressing ($AQP1^{OE}$) and control LECs expressing enhanced blue fluorescent protein ($EBFP^{OE}$) via lentiviral transduction (Fig. 4A). Western blot analysis confirmed AQP1 overexpression, displaying distinct bands corresponding to glycosylated and non-glycosylated forms (Denker et al., 1988), while control cells lacked detectable AQP1 expression (Fig. 4B). Immunofluorescence staining showed prominent membrane, junctional and cytoplasmic localization of AQP1 in $AQP1^{OE}$ LECs (Fig. 4C).

To assess the impact of AQP1 on lymphangiogenic responses, we employed a spheroid sprouting assay (Zheng et al., 2011). LEC spheroids were embedded in fibrin gel and cultured in the presence or absence of VEGF-C in normosmotic (~300 mOsm) or hyperosmotic (~500 mOsm) conditions, reflecting osmolarity observed at the villus tip (Hallbäck et al., 1991) (Fig. 4, D and E).

While VEGF-C stimulation promoted sprouting overall, this effect was significant only in *AQP1*^{OE} cells, which formed significantly more sprouts per spheroid than control cells under both normosmotic and hyperosmotic conditions (Fig. 4, E and F, Table S2). Hyperosmotic stress suppressed sprouting in both cell types relative to normosmotic conditions, however, *AQP1*^{OE} LECs maintained significantly higher sprout numbers and total sprout length as compared to controls (Fig. 4, F and G, Table S2). LECs exposed to hypoosmotic conditions showed a tendency towards increased sprouting even without VEGF-C, although AQP1 overexpression did not affect sprouting under these conditions (Fig. S4A). The number of nuclei per 100 μm sprout length remained comparable between *AQP1*^{OE} and control cells under all conditions (Fig. S4B), indicating that AQP1 promotes sprout formation independently of altered proliferation or cell density within established sprouts.

To examine the cellular composition of sprouts we quantified nucleated sprouts (containing ≥1 nucleus) versus nuclei-free protrusions (Fig. S4C). Under VEGF-C stimulation at normosmotic conditions, *AQP1*^{OE} spheroids generated more nucleated sprouts (Fig. 4F) without significant differences in total protrusion number (Fig. S4C). Under hyperosmotic stress with VEGF-C, both cell types formed similar numbers of protrusions (Fig. S4C), but *AQP1*^{OE} cells generated substantially more sprouts (Fig. 4F).

Interstitial flow is an important parameter for lymphatic endothelial junctions and sprouting (Lee et al., 2023). Therefore, we validated our findings in spheroids using a microfluidic sprouting assay, the Vascular Phenotypic and Proteomic (VPT) platform in which LECs are also exposed to interstitial flow (Jung et al., 2024). *AQP1*^{OE} LECs similarly showed increased sprout number under hyperosmotic stress (500 mOsm) in the VPT device without changes in nuclei per sprout (Fig. S4, D and E). Collectively, our results demonstrate that AQP1 sustains lymphangiogenic sprouting under osmotic stress, by enhancing both the number of sprout initiations and, specifically under osmotic stress, the extent of their elongation, consistent with its known role in facilitating rapid cell volume changes required for membrane protrusion and motility (Papadopoulos et al., 2008; Karlsson et al., 2013).

Aqp1-deficient LECs fail to occupy lacteal tip positions

Having shown that AQP1 promotes LEC migration under hyperosmotic stress *in vitro*, we tested the cell-autonomous AQP1 requirement *in vivo*. We generated *Rosa26-EYFP;Aqp1*^{iΔLEC} mice and administered reduced tamoxifen dosing to achieve mosaic Cre activation, for simultaneous *Aqp1* deletion and YFP expression in LECs (Fig. 4H), enabling tracking of *Aqp1*-deficient cells. Three weeks post-injection, whole-mount staining revealed significantly fewer YFP^{+} LECs in *Aqp1*^{iΔLEC} lacteals compared to controls (Fig. 4, H and I), indicating depletion of *Aqp1*-deficient cells. Spatial analysis revealed that this depletion was position dependent: YFP^{+} cells were enriched at the base (0-20% lacteal length) and progressively depleted toward the tip (80-100%) (Fig. 4, J and K). This spatial exclusion

validates our *in vitro* finding that AQP1 enables migration under hyperosmotic conditions and explains the shortened lacteal phenotype observed with tissue-wide deletion (Fig. 4L).

AQP1 modulates cytoskeletal dynamics through β-catenin interaction

Hyperosmotic stress induces cortical actin formation and junction stabilization as a protective response to prevent membrane deformation (Di Ciano et al., 2002), but these changes also limit protrusion formation and reduce EC migration (Abu Taha and Schnittler, 2014). To investigate how AQP1 facilitates LEC migration under these conditions, we examined cytoskeletal and junctional architecture by F-actin and β-catenin staining. In control LECs, hyperosmotic stress induced the formation of a cortical actin cytoskeleton and thin, linear adherens junctions (Fig. 5A). In contrast, *AQP1*-overexpressing LECs maintained overlapping, reticular adherens junctions reminiscent of junction-associated intermittent lamellipodia (JAIL) (Cao et al., 2017) and displayed prominent stress fiber formation rather than cortical actin, even under hyperosmotic stress. These features, characteristic of actively remodeling endothelium, were already evident in AQP1-overexpressing LECs under normosmotic conditions (Fig. 5A). This pattern was confirmed by quantitative analysis of F-actin intensity from cell periphery to center (Fig. 5B). *AQP1* overexpression also increased total β-catenin protein levels (Fig. 5, A, C and D), suggesting that AQP1 stabilizes β-catenin. Proximity ligation assays (PLA) confirmed AQP1-β-catenin interaction *in situ*, with signal significantly enhanced under hyperosmotic compared to control conditions (Fig. 5, E and F).

Lymphatic vessels experience estimated physiological hydrostatic pressures of 0.3-2.6 mmHg (Sloas et al., 2016). To test whether the effects of AQP1 extend to other mechanical stresses, we examined LEC responses at 2 mmHg hydrostatic pressure. AQP1-overexpressing cells showed similar F-actin redistribution (Fig. S4, F-H), indicating that AQP1 promotes adaptive cytoskeletal remodeling across multiple mechanical stress modalities. Thus, AQP1 counteracts the stabilizing effects of hyperosmolarity on the actin cytoskeleton and cell-cell junctions, preserving JAIL-like junctional structures and stress fibers, characteristic of dynamic endothelial remodeling. This cytoskeletal adaptation aligns with the enhanced sprouting capacity of AQP1 LECs in vitro and in vivo, highlighting AQP1 as a regulator of lymphangiogenic response under osmotic stress.

AQP1 alleviates osmotic stress-induced transcriptional programs

Osmotic stress triggers a rapid and coordinated transcriptional response in mammalian cells to elicit osmolyte regulation, cytoskeletal adaptation, and stress resilience, enabling cells to withstand osmotic challenges (Burg et al., 2007). To define the transcriptional landscape of LECs under osmotic stress and identify AQP1-dependent rescue pathways, we performed RNA sequencing of control and $AQP1^{OE}$

LECs cultured under normosmotic (300 mOsm) and hyperosmotic (500 mOsm) conditions (Fig. 6A). In control cells hyperosmotic stress induced extensive transcriptional reprogramming, with 1593 differentially expressed genes (Fig. 6B). Upregulated genes included osmotic stress response factors (e.g., *SGK1*, *NFAT5*), pro-inflammatory chemokines (e.g., *CCL2*, *CXCL10*), and transcripts linked to DNA damage response pathways. Downregulated genes included cell cycle regulators (e.g., *CCNB1*), DNA replication machinery, and metabolic enzymes involved in nucleotide and lipid biosynthesis (Fig. 6B). This transcriptional profile reflects a shift from proliferation and biosynthesis toward stress protection, with suppression of cytoskeletal and cell cycle genes that would impair migration and remodeling capacity. We validated key differentially expressed genes by qPCR, including *SGK1* (osmotic stress response), *ZFP36L1* (mRNA stability under stress), and *PKN1* (cytoskeletal regulation) (Fig. S5A).

AQP1 overexpression rescued nearly half (46%, 724 genes) of the osmotic stress-induced transcriptional changes, maintaining their expression near baseline levels even under hyperosmotic conditions (Fig. 6, D and E; Table S3). These rescued genes included multiple pathways involved in cytoskeletal organization, including actin-binding proteins, focal adhesion components, and regulators of membrane protrusions (Fig. 6F). Together with the cytoskeletal and junctional remodeling data (Fig. 5), these findings establish that AQP1 enables LEC migration under osmotic stress through coordinated structural and transcriptional mechanisms.

AQP1 is induced during inflammatory but not embryonic lymphangiogenesis

Having established that AQP1 enables LEC migration by alleviating osmotic stress-induced cytoskeletal and transcriptional changes, we next asked whether AQP1 induction and function extend to other postnatal contexts in which lymphatic remodeling occurs in inflammatory, osmotically challenging microenvironments. Inflammation and impaired lymphatic drainage promote accumulation of extracellular proteins and Na^+, thereby elevating tissue osmolarity (Jantsch et al., 2015; Karlsen et al., 2006), conditions that parallel the hyperosmotic challenge experienced by lacteals. We therefore examined PIK3CA-driven lymphatic malformations, inflamed lymph nodes and secondary lymphedema.

Activating mutations in *PIK3CA* underlie development of lymphatic vascular malformations in humans (Alitalo, 2011; Luks et al., 2015; Castel et al., 2016; Petkova et al., 2024). Signaling through the VEGF-C/VEGFR3 axis activates the PI3K-AKT pathway, promoting LEC survival, proliferation, and migration (Mäkinen et al., 2001). Abnormal dermal lymphatic vascular growth in *Pik3ca*^{H1047R} mutant mice is sustained by accumulation of VEGF-C-producing macrophages, which selectively expand *Ptx3*-high immune-interacting LECs by paracrine signaling (Martinez-Corral et al., 2020; Petkova et al., 2023). Given that *Aqp1*-high lacteals share transcriptional similarities with *Ptx3*-high

dermal capillary LECs (Fig. 1H), we examined *Aqp1* expression in dermal LECs from *Pik3ca*^{H1047R} mice. Re-analysis of scRNA-seq data from the dermal LECs of *Pik3ca*^{H1047R}*; Cdh5-CreERT2* mice (Petkova et al., 2023) revealed that *Ptx3*$^{+}$ capillary LECs in mutants exhibited a higher proportion of cells in the highest *Aqp1* expression quartile compared to other capillary populations (Fig. 7A). At the protein level, AQP1 was absent in lymphatic vessels of control ears but markedly increased in hypersprouting VEGFR3^{+} LECs of mutant *Pik3ca*^{H1047R}*; Vegfr3-CreERT2* mice (Fig. 7B). Similarly, medullary sinus LECs in normal and inflamed lymph node, which share the *Ptx3*$^{+}$ gene signature (Xiang et al., 2020) (Fig. 1H), showed prominent AQP1 expression (Fig. 7C and Fig. S5B), whereas subcapsular sinus LECs showed low or undetectable AQP1 under control and inflammatory conditions (Fig. S5, B and C).

To determine whether AQP1 induction is a general feature of inflammatory lymphangiogenesis, we examined a mouse model of secondary lymphedema (Buntinx et al., 2022). In this model, hindlimb lymphatic injury is induced by combining local irradiation of the inguinal region with surgical ablation of the inguinal lymph node, followed by ligation of surrounding lymphatic vessels. This procedure results in impaired lymphatic drainage, vessel dilation, and remodeling, tissue fibrosis and inflammation (Buntinx et al., 2022; Rockson et al., 2019). Lymphatic injury triggers an inflammatory response, involving macrophages, T-helper and CD8^{+} T cells, neutrophils, and pro-inflammatory cytokines and lipids, such as TNFα, and LTB_4, which drive acute and chronic inflammation (Bowman and Rockson, 2024). Lymphedematous skin showed a significant increase in CSF1R^{+} macrophages (Ghanta et al., 2015) and CD4^{+} T cells (Zampell et al., 2012) compared to controls (Fig. S5D). Similar to lymphedematous skin, CSF1R^{+} macrophages were abundant in the intestinal villi, where they were in direct contact with AQP1^{+} lacteals (Fig. S5E). In contrast, macrophages were sparse and remained detached from AQP1^{-} submucosal lymphatic vessels.

Immunofluorescence analysis revealed markedly dilated VEGFR3^{+} lymphatic vessels in lymphedematous skin, with strong AQP1 expression, while lymphatic vessels in control samples (Fig. 7D) were thin, collapsed, and AQP1-negative. AQP1-high and AQP1-low areas were detected within the same lymphatic vessel, suggesting local cues drive AQP1 expression (Fig. 7D and S5F). Additionally, uniform AQP1 upregulation was observed in EMCN^{+} blood vessels within lymphedema tissues (Fig. S5G). To address the potential function of lymphatic AQP1 in lymphedema, we analyzed the correlation between its expression and LEC proliferation. Immunostaining for AQP1, PROX1, and proliferation marker Ki67 revealed an absence of proliferation in control skin samples and pronounced overall increase in Ki67^{+} LECs and stromal cells in lymphedema samples (Fig. 7E). Importantly, the proportion of proliferating Ki67^{+} cells was significantly higher in AQP1^{+} LECs compared to AQP1^{-} population, suggesting that AQP1 may be important for lymphatic vessel remodeling under inflammatory conditions.

The consistent AQP1 induction across postnatal pathological contexts, all characterized by inflammatory remodeling and elevated tissue osmolarity (Bowman and Rockson, 2024; Jantsch et al., 2015), raised the question of whether AQP1 is also expressed during embryonic lymphangiogenesis, which proceeds through VEGF-C/VEGFR3 signaling but lacks inflammatory and osmotic stresses (Hallbäck et al., 1991; Tammela et al., 2008; Gordon et al., 2010). We examined dermal skin at E16.5, and found that AQP1 was expressed in $CD31^+$ blood vessels and structures consistent with peripheral nerves (Ma et al., 2011), but not in $VEGFR3^+$ sprouting lymphatic vessels (Fig. 8A). Similarly, embryonic lymph nodes (E17.5-E18.5) showed no AQP1 expression in developing $LYVE1^+PROX1^+$ LECs despite active lymphangiogenesis (Fig. 8B). Collectively, our findings in lymphatic malformations, secondary lymphedema and inflamed lymph nodes demonstrate that AQP1 expression is induced during proinflammatory postnatal lymphatic remodeling but not during embryonic lymphangiogenesis.

AQP1 facilitates postnatal compensatory lymphangiogenesis

The absence of AQP1 during embryonic lymphangiogenesis, despite active VEGF-C/VEGFR3 signaling, raised the question of whether AQP1 is merely associated with inflammatory contexts or functionally required for stress-adaptive remodeling. To address this, we used the *Foxc2*^{lecko} model, which recapitulates lymphedema-distichiasis, a hereditary late-onset lymphedema (Petrova et al., 2004; Sabine et al., 2015). We have previously shown that loss of *Foxc2* triggers degeneration of lymphatic valves, causing lymph reflux and stasis within mesenteric collecting vessels, followed by accumulation of protein- and solute-rich chyle in surrounding tissue (González-Loyola et al., 2021; Sabine et al., 2015), likely elevating local osmolarity. Consistent with this, postnatal *Foxc2*-deficient LECs showed a significant increase in AQP1 expression (González-Loyola et al., 2021) (Fig. 8C), mirroring our findings in secondary lymphedema, inflamed lymph node, and lymphatic malformations. In contrast, in E18.5 *Foxc2*^{lecko} embryos, mesenteric lymphatic vessels showed no AQP1 expression despite active remodeling (Fig. 8D).

We observed that lymphatic valve degeneration was frequently associated with both marked AQP1 induction at valve sinuses and sprouting at the site of disappearing valves, indicating the formation of a compensatory collateral lymphatic network (Sabine et al., 2015) (Fig. 8E). To determine whether AQP1 plays a functional role in this process, we generated *Aqp1;Foxc2*^{lecko} double knockout mice. *Aqp1* deletion significantly reduced collateral sprout formation by ~40% compared to control *Foxc2*^{lecko} mice (Fig. 8, D-F). This demonstrates that AQP1 functionally contributes to postnatal pathological lymphatic remodeling, although the absence of direct tissue osmolarity measurements represents a limitation that should be addressed in future work. Together, these findings establish a model in which AQP1 is dispensable for developmental lymphangiogenesis but becomes essential when

LECs must migrate and remodel within hyperosmotic or inflammatory microenvironments (Fig. 9). Previous studies have shown that AQP1's water transport function facilitates lamellipodia extension and endothelial migration by enabling rapid volume changes at the leading edge (Kondrychyn et al., 2025). Based on our data, we now propose that AQP1 maintains β-catenin-dependent junctional dynamics and cytoskeletal architecture, enabling LECs to overcome the inhibitory effects of hyperosmotic stress on migration.

Discussion

We identified the water channel AQP1 as a functionally significant marker of lacteal LECs, required for lacteal maintenance and efficient dietary lipid absorption. Lacteal LECs display a transcriptional signature resembling *Ptx3*$^{+}$ immune-interacting LECs, with *Aqp1* as a core component of this program. Extending beyond the intestine, we show that AQP1 is induced during inflammatory lymphatic remodeling in lymphatic malformations, lymph nodes, and lymphedema but absent during embryonic lymphangiogenesis, distinguishing stress-adaptive from developmental lymphatic responses.

In scRNAseq analysis of intestinal LECs we identified three subpopulations of murine intestinal LECs, including lacteal, S/S (submucosal and serosal), and IFN subtypes, defined by characterizing markers and AQP1 expression as a specialized lacteal adaptation. Comparison of intestinal LECs with LECs from other organs shed new light on lacteal LECs, demonstrating their similarity to *Ptx3*$^{+}$ inflammatory LECs, while S/S LECs bear transcriptional traits characteristic of pre-collector lymphatics, allowing a clearer understanding of their distinct roles.

Lacteal LECs experience fluctuating osmotic conditions due to nutrient absorption, with tip osmolarities reaching ~600 mOsm (Hallbäck et al., 1991). During fat absorption, chylomicron accumulation and increased solute concentration in the lamina propria generate osmotic gradients that acutely alter lacteal junction configuration to allow chylomicron and nutrient entry (Zarkada et al., 2023). These conditions require rapid water movement; therefore, we propose that AQP1 is essential for swift adaptation of LECs to osmotic changes (Thiagarajah and Verkman, 2002). Accordingly, *Aqp1* deletion in LECs caused lacteal shortening and decreased fat absorption, matching prior findings for shorter lacteals (Bernier-Latmani et al., 2015; Nurmi et al., 2015; Hong et al., 2020). This suggests that AQP1 promotes lacteal integrity, by facilitating LEC migration through volume regulation necessary for protrusion formation (Saadoun et al., 2005; Papadopoulos et al., 2008; Karlsson et al., 2013). Supporting this notion, overexpression of *AQP1* enhanced LEC migration in a spheroid sprouting assay under hyperosmotic conditions in the presence of VEGF-C. Lacteal shortening and reduced fat absorption in *Aqp1*$^{i\Delta LEC}$ likely explain attenuated weight gain on HFD. While the fate of unabsorbed lipids and broader metabolic adaptations remain to be characterized, the metabolic phenotype of

Aqp1$^{i\Delta LEC}$ mice resembled that of mice with germline *Aqp1* deletion, which also display reduced weight gain on a high-fat diet and decreased serum triglycerides, with body weight normalizing on a low-fat diet (Ma et al., 2001), indicating a primary contribution of lacteal AQP1.

The role of AQP1 in cell migration has been attributed to its facilitation of rapid water fluxes at the leading edge of migrating cells, where local osmotic gradients drive membrane protrusion as demonstrated in blood endothelial and cancer cells (Saadoun et al., 2005; Papadopoulos et al., 2008). Our findings reveal a distinct aspect of this function. When the bulk extracellular environment is hyperosmotic, cells reinforce cortical actin and stabilize junctions, a protective response that restricts motility (Di Ciano et al., 2002). AQP1 counteracts this response, maintaining stress fibers and junctional dynamics characteristic of migrating cells. The interaction with β-catenin, enhanced under osmotic stress, may coordinate this response by linking water transport to junctional regulation. β-catenin serves dual roles in adhesion and signaling (Nelson and Nusse, 2004), and its stabilization by AQP1 could simultaneously preserve junctional plasticity and activate pro-migratory transcriptional programs. Indeed, transcriptional profiling revealed that AQP1 rescues a substantial fraction of osmotic stress-suppressed genes, particularly those governing cytoskeletal dynamics. This suggests that AQP1 does not merely enable cells to tolerate osmotic stress passively, but actively maintains the molecular machinery required for migration. This is evident in mosaic deletion experiments: *Aqp1*-deficient LECs are excluded from tip positions, consistent with a model in which cells compete for position based on their local fitness (Jakobsson et al., 2010).

We observed a dynamic pattern of AQP1 expression in lacteals, with intensity increasing after birth, peaking at the lacteal tip around P5 and persisting into adulthood. This timing coincides with the onset of milk intake (Knight et al., 1986) and a sharp increase in intestinal bacterial load (Hasegawa et al., 2010), both likely contributing to osmolarity fluctuations. Concurrently, macrophages gather in the lamina propria, providing a source of VEGF-C (Suh et al., 2019). For instance, F4/80^{+} macrophages, concentrated at the villus base in 2-day-old neonates, expand dramatically over the next 12 days to reside predominantly near capillaries, with occasional presence in the submucosa (Cecchini et al., 1994). Increased macrophage density parallels lacteal growth, underscoring how immune-derived VEGF-C fosters functional lacteals. Alongside smooth muscle cells and fibroblasts, these macrophages constitute major VEGF-C sources in the gut (Nurmi et al., 2015; Hong et al., 2020; Suh et al., 2019). Gut microbiota also shape the distribution and morphology of intestinal CX3CR1^{+} macrophages, with antibiotic treatment reducing their presence in the lamina propria but not in the submucosa (Honda et al., 2020). Consistent with the essential role of VEGF-C/VEGFR3 signaling in lacteal development and maintenance (Bernier-Latmani et al., 2015; Nurmi et al., 2015; Tammela et al., 2008) both antibiotic treatment and VEGFR3 blockade diminished AQP1 expression. Reduced AQP1 levels under antibiotic treatment likely reflect lower VEGF-C in the lamina propria, aligning with evidence that gut microbiota modulates VEGF-C levels via macrophage-dependent mechanisms (Suh et al., 2019). Nevertheless,

absence of AQP1 expression during VEGFR3-VEGF-C-dependent embryonic lymphangiogenesis suggests that additional immune-derived signals or osmotic factors are necessary for robust AQP1 induction.

To further contextualize our findings, lacteal LECs showed highest similarity with the *Ptx3*$^{+}$ LEC subset, with elevated expression of *Ptx3*, *Itih5*, and *Mrc1* (Table S1), genes associated with immune cell interactions. Specifically, MRC1 binds CD44^{+} lymphocytes (Salmi et al., 2013), PTX3 increases responses to inflammatory signals (Garlanda et al., 2005), and ITIH5 interacts with PTX3 (Scarchilli et al., 2007). This immune-interactive profile aligns with the known biology of lacteals, which are surrounded by macrophages in the lamina propria (Fig. S5D) (Cecchini et al., 1994) and continuously exposed to damage- and pathogen-associated molecular patterns derived from food and microbiota (Bernier-Latmani et al., 2024). Similarly, PTX3^{+} dermal LECs expand under inflammatory lymphangiogenesis and interact with macrophages (Petkova et al., 2023). In lymph nodes, *Ptx3*$^{+}$ LECs populate the medullary sinus, a region rich in F4/80^{+} macrophages (Louie and Liao, 2019) and dense with lymphocyte-macrophage clusters following immunization (Friess, 1977). These similarities suggest that local immune cues and tissue-specific signals may shape specialized LEC states adapted to distinct tissue environments.

The similarity to immune-interacting LECs, together with our previous finding that AQP1 is strongly induced in mesenteric LECs in hereditary lymphedema-distichiasis (González-Loyola et al., 2021), led us to explore the role of AQP1 in inflammatory conditions more broadly. Here, we show that AQP1 is markedly induced in LECs in secondary lymphedema, lymphatic malformations driven by hyperactive PI3K signaling (*Pik3ca*^{H1047R}) and immunized lymph nodes. During inflammatory lymphangiogenesis, macrophages secrete lymphangiogenic factors such as VEGF-C (Cursiefen et al., 2004; Kataru et al., 2009), potentially promoting both lymphatic vessel proliferation and AQP1 upregulation. Elevated AQP1 levels correlate with increased proliferative activity in these inflamed vessels, suggesting that AQP1 may drive, or at least mark, remodeling processes in lymphedema and lymphatic malformations. In contrast, embryonic dermal lymphangiogenic vessels exhibit robust sprouting and proliferation without AQP1 induction, indicating that while embryonic LECs rely on VEGF-C/VEGFR3 signaling, they lack the inflammatory, metabolic or osmotic cues needed for AQP1 upregulation. Even embryonic *Foxc2*^{lecko} lymphatic vessels, despite active pathological remodeling, showed no AQP1 expression, whereas adult *Foxc2*^{lecko} mice displayed marked AQP1 induction at the same anatomical sites. This developmental difference likely reflects the distinct cellular environments: embryonic lymphangiogenesis proceeds independently of macrophages (Gordon et al., 2010), whereas postnatal inflammatory remodeling is macrophage-driven, providing both VEGF-C and inflammatory cues that induce AQP1. Consistent with this, AQP1 protein was not detected in normal dermal LECs, despite the presence of *Aqp1* transcripts, possibly due to additional posttranscriptional mechanisms that regulate AQP1 protein stability. Indeed, osmolarity rises in lymphedema (Karlsen et al., 2006), and

concurrent AQP1 induction may accommodate rapid water flux and enhanced cell migration. The functional requirement for AQP1 in the *Foxc2*^{lecko} lymphedema model, where its deletion reduces compensatory collateral, indicates that AQP1 is not merely induced as a stress marker but actively contributes to the remodeling response. That substantial collateral formation still occurred suggests redundant mechanisms exist, yet AQP1 clearly provides an adaptive advantage under pathological stress. Direct measurement of tissue osmolarity in the pathological contexts examined remains a study limitation; the documented inflammation and impaired lymphatic drainage in these models nonetheless point to osmotically challenging microenvironments.

Collectively, our findings establish AQP1 as a marker of actively remodeling postnatal LECs within inflammatory microenvironments (Fig. 9). The common thread linking lacteals, lymphatic malformations, and lymphedema is the convergence of osmotic stress and inflammatory signaling, conditions absent from embryonic lymphangiogenesis even under pathological conditions. Inflammation and lymphatic dysfunction promote accumulation of extracellular proteins and Na^+, thereby elevating tissue osmolarity (Jantsch et al., 2015; Karlsen et al., 2006). Although acute increases in osmolarity support immune cell activation and help combat infections, we propose that in lymphedema, chronic inflammation combined with impaired lymphatic drainage elevates osmolarity to levels that prevent regenerative lymphangiogenesis, even in the presence of abundant VEGF-C. Under these conditions AQP1 enables LECs to overcome this osmotic barrier. These insights suggest therapeutic opportunities: enhancing AQP1 function or reducing pathological tissue osmolarity may improve lymphatic regeneration in lymphedema, while in hyperproliferative conditions such as lymphatic malformations, AQP1 inhibition could be evaluated as an additional treatment option.

Materials and methods

Animal studies

All animal care and experimental procedures were performed in accordance with relevant national and institutional guidelines, following approval by the Animal Ethics Committee of Vaud (Switzerland), the Uppsala Animal Experiment Ethics Board (Sweden), or the local Animal Ethical Committee at the University of Liège (Belgium). Mice were on C57BL/6J background and were maintained under specific pathogen-free conditions with a 12-hour light/dark cycle and *ad libitum* access to food and water. Unless otherwise specified, experiments were conducted using age- and sex-matched cohorts of adult mice aged 8-12 weeks. Littermate controls were used for all experiments.

Generation of inducible Aqp1 knockout mice. To generate tamoxifen-inducible, LEC-specific *Aqp1* knockout mice ($Aqp1^{i\Delta LEC}$), $Aqp1^{fl/fl}$ mice (Zhang et al., 2016) were crossed with *Prox1-CreERT2* (Bazigou et al., 2011) mice. To induce *Aqp1* deletion, tamoxifen (T5648, Sigma-Aldrich) was dissolved by sequentially adding 100% ethanol, Kolliphor EL (Sigma-Aldrich, Cat# C5135), and phosphate buffer saline (PBS) in a 1:1:8 ratio, with thorough mixing after each addition, to prepare a stock solution at a concentration of 10 mg/ml. Control $Aqp1^{fl/fl}$ and $Aqp1^{i\Delta LEC}$ mice received intraperitoneal injections of 50 µg/g body weight tamoxifen. Injections were administered to adult mice (as specified per experiment) three times every other day during the first week, followed by one injection per week until sacrifice.

For mosaic deletion experiments, *Rosa26-EYFP* reporter mice (Srinivas et al., 2001) were crossed with $Aqp1^{fl/fl;}$ *Prox1-CreERT2* mice to generate *Rosa26-EYFP*; $Aqp1^{i\Delta LEC}$ mice. To achieve sparse Cre recombination and simultaneous YFP expression in individual LECs, a single low-dose tamoxifen injection (7.5 µg/g body weight) was administered intraperitoneally at 8 weeks of age. Mice were sacrificed three weeks post-injection.

Foxc2-deficient lymphatic models. $Foxc2^{fl/fl}$ mice were crossed with *Prox1-CreERT2* mice to generate $Foxc2^{lecko}$ ($Foxc2^{fl/fl}$;*Prox1-CreERT2*) mice (González-Loyola et al., 2021). To generate $Aqp1^{fl/fl}$;$Foxc2^{fl/fl}$;*Prox1-CreERT2* $Aqp1^{fl/fl}$ mice were crossed with $Foxc2^{lecko}$ mice. For analysis of AQP1 expression in embryonic *Foxc2*-deficient lymphatics, pregnant $Foxc2^{fl/fl}$ dams crossed with $Foxc2^{lecko}$ male mice were injected subcutaneously with 100 µL of tamoxifen/progesterone solution (50 mg/mL in Kolliphor EL) at E13.5 and E14.5. Embryos were harvested at E18.5. For collateral sprouting analysis in neonatal *Aqp1;Foxc2* double knockout mice, a single dose of tamoxifen (62.5 µL from 2 mg/mL stock, 125 µg total) was administered intraperitoneally at P4, and mice were analyzed at P8. For AQP1 induction in adult $Foxc2^{lecko}$ mice, tamoxifen was administered intraperitoneally at 50 µg/g body weight three times every other day starting at 5 weeks of age, as described above. Mice were analyzed at 22 weeks of age.

***R26-Pik3ca^{H1047R}*; *Vegfr3-CreERT2* mice** were generated by crossing of *R26-Pik3ca^{H1047R}* (Eser et al., 2013) with *Vegfr3-CreERT2* mice (Martinez-Corral et al., 2016). Dermal lymphatic malformations were induced as previously described (Martinez-Corral et al., 2020). Briefly, 50µg of 4-hydroxy-tamoxifen dissolved in acetone was applied topically to the ear of 3-week-old mice. Mice were sacrificed 3 weeks later, and the dorsal ear skin was dissected from underlying cartilage and fixed in 4% (paraformaldehyde) PFA in PBS for 2 hours at room temperature. Tissue was subsequently washed twice with PBS before proceeding to immunostaining.

Secondary lymphedema model. The hindlimb lymphedema model combined local irradiation and surgical intervention as previously described (Buntinx et al., 2022). Lymphedema was induced in the left limb, with the right limb serving as an internal control. For irradiation, mice were anesthetized with 2% isoflurane and positioned ventrally inside a precision X-ray irradiator. To accurately target the inguinal region, X-ray radiography (40 kV, 0.5 mA) was performed. A 20 mm-square collimator was placed over the targeted area to deliver a single 30 Gy dose (225.0 kV, 13.00 mA) in an anteroposterior direction. The left limb was irradiated for 317 seconds on the ventral side and an additional 317 seconds on the dorsal side. One week later, surgery was performed under 2% isoflurane anesthesia on a 37°C heating pad within a horizontal airflow hood. The left hindlimb was shaved, disinfected with dermal isobetadine, and injected with 5 µL of 2% Evans Blue dye between the footpads to visualize lymphatic structures. Lymphatic injury was induced through a three-steps surgery: i) a circumferential skin incision at the inguinal level, ii) excision of the inguinal and popliteal lymph nodes, and iii) ligation of collecting lymphatic vessels parallel to the ischial vein with three separate 7/0 non-absorbable polypropylene sutures under a 10x binocular magnifier. Finally, the skin was sutured with 5/0 non-absorbable silk stitches.

Antibiotic treatment. Wild-type (*Aqp1$^{fl/fl}$*) and *Aqp1^{iΔLEC}* mice were co-housed from weaning to minimize microbiota differences. Three weeks after tamoxifen administration, adult mice were treated with a broad-spectrum antibiotic cocktail in their drinking water for four weeks. The treatment consisted of enrofloxacin (2.5 mg/ml; Baytril 10%, Bayer) for the first two weeks, followed by amoxicillin (0.8 mg/ml) and clavulanic acid (0.114 mg/ml; Co-Amoxi-Mepha, Mepha) for the subsequent two weeks (González-Loyola et al., 2021). Control mice received regular drinking water.

High-fat diet (HFD) feeding. After inducing *Aqp1* deletion with tamoxifen over a two-week period - three doses administered every other day during the first week and one dose during the second week - the mice were fed either a HFD (D12492i, Research Diets: 60 kcal% fat, 20 kcal% protein, 20 kcal% carbohydrate) or a matched normal chow diet (NCD; D12450Bi, Research Diets: 10 kcal% fat, 20 kcal% protein, 70 kcal% carbohydrate) for three weeks. Mice were randomly assigned to either the HFD or NCD group, and diets were provided ad libitum. Body weights were recorded weekly.

VEGFR3 signaling blockade. Neonatal mice were administered subcutaneous injections of the VEGFR3-blocking antibody mF4-31C1 (Pytowski et al., 2005) (Table S4) or isotype-matched IgG2a antibody at P4, P6, and P8 at dose of 40 µg/g body weight using 30G needle. Tissues were harvested on P10 for analysis.

Lipid absorption assay. Mice were fasted for 6 hours and then orally gavaged with olive oil (O1514, Sigma-Aldrich) at a dose of 10 µl/g body weight using a 20G, 60 mm gavage needle. Blood samples were collected from the tail vein at baseline (0 hours) and at 1, 2 and 3 hours post-gavage into lithium heparin-coated tubes (Microvette CB 300 Hep-Lithium, Sarstedt). Samples were kept on ice for 30 minutes and centrifuged at 14,000 × g for 15 minutes at 4 °C to obtain plasma, which was stored at -80 °C until analysis. Plasma triglyceride levels were measured on diluted samples (1:1 plasma to diluent ratio) using the Dimension® Xpand Plus system (Siemens Healthcare Diagnostics AG, Düdingen, Switzerland) according to the manufacturer's protocol for triglyceride measurement (Siemens Healthcare, DF69A).

For experiments with the lipoprotein lipase inhibitor, mice received intraperitoneal injection of Tyloxapol (Lucerna-Chem, HY-B1068-1G, at 500mg/kg body weight) 30 minutes before oral gavage, followed by the olive oil gavage protocol and blood sampling as described above.

Lymph node analyses. Embryonic (E17.5-E18.5) and young adult male (9 weeks) inguinal lymph nodes were used for control stainings. For immunization, 16-17-weeks old females were injected with oligodeoxynucleotides CpG (Microsynth) and keyhole limpet hemocyanin (NP-KLH) (10 µg each in 10 µl) into the footpads. On day 7 mice were sacrificed, and inguinal lymph nodes were harvested and processed for cryosections.

Isolation and FACS sorting of mouse intestinal LECs

Tissue processing. Small intestinal segments (excluding the duodenum) were collected using curved scissors and washed by gently vortexing in 50 ml Falcon tubes containing cold PBS, followed by a second wash in cold PBS. To remove epithelial cells, the tissues were incubated at 37 °C and 150 rpm in Hank's Balanced Salt Solution (HBSS) containing 5 mM EDTA, 1 mM DTT, and 20 µM HEPES for 15–20 minutes, briefly vortexed, rinsed in HBSS until the supernatant was clear, and then enzymatically digested in HBSS containing Liberase TL at a final concentration of 0.9 U/ml and DNase I at 0.1 mg/ml for 60 minutes at 37 °C, 180 rpm. Every 20 minutes, tissues were pipetted up and down to promote dissociation; the resulting supernatant was passed through a 70 µm strainer into 10 ml cold HBSS with 10% FBS. The remaining tissue fragments were returned to fresh digestion medium. After three rounds of digestion, cell suspensions were centrifuged at 1200 rpm for 5 minutes at 4 °C.

For scRNAseq experiments, we obtained intestinal tissues from three female and two male C57Bl/6 mice (9-10 weeks old), whereas for qPCR analyses we utilized samples from three $Aqp1^{fl/fl}$ and three $Aqp1^{i\Delta LEC}$ mice.

Cell staining and FACS sorting. Cells were resuspended in PBS containing 5% FBS and incubated with anti-CD16/32 (2.4G2) hybridoma supernatant to block non-specific IgG binding. Cells were stained with conjugated antibodies: for scRNA-seq, CD45-FITC, CD31-BV421, and PDPN-PE; for qPCR, EpCAM-BV421, CD45-PE-Cy7, CD31-PE, and PDPN-APC. Before sorting, 0.1 µg/ml DAPI and RedDot1 were added for 5 minutes at room temperature to exclude dead cells and debris. LECs were gated as $DAPI^-$ $redDot^+$ $CD45^-$ $CD31^+$ $PDPN^+$ cells. For qPCR samples, an additional exclusion of $EpCAM^+$ cells ($EpCAM^-$) was applied. Cells were sorted into HBSS containing 30% FBS at 4 °C on a Beckman Coulter MoFlo Astrios EQ cell sorter equipped with a 70 µm nozzle, operating at 60 psi. The sort precision was set to "enrich" to maximize yield. On average, 23,000 LECs were sorted per sample, and sorting experiments were performed in three independent replicates.

Lymphatic endothelial cell (LEC) culture systems and experimental manipulations

Isolation and culture of LECs. Human intestinal_LECs were isolated from discarded surgical specimens with informed consent and institutional approval, as described in (Norrmén et al., 2010). Intestinal segments were washed in PBS, incubated in RPMI + 10% FCS overnight at 4°C to facilitate epithelial cell removal, and the epithelium was scraped off using a cell scraper. The mucosal layer was carefully dissected, cut into small pieces, and subjected to enzymatic digestion with collagenase A (1 mg/ml) and dispase II (2 mg/ml) supplemented with DNase I (20 µg/ml) in RPMI at 37°C for two sequential 30-minute incubations with magnetic stirring. The cell suspension was filtered through a 200 µm metal sieve, and cells were seeded on fibronectin-coated flasks (5 µg/cm²; 10838039001, Roche, Basel, Switzerland) at 1×10^6 cells/cm². Contaminating fibroblasts were depleted by negative selection using magnetic-activated cell sorting (MACS) with anti-human CD44 antibody (Clone F10-44-2, 9400-01, Southern Biotech, Birmingham, AL, USA) coupled to sheep anti-mouse IgG-coated paramagnetic beads (SAM beads, 110.02, Dynal/Thermo Fisher Scientific). LECs were subsequently enriched by positive selection using anti-CD31-coated magnetic beads (Dynabeads CD31 Endothelial Cell, 111.55D, Dynal/Thermo Fisher Scientific) and re-plated on fibronectin-coated flasks in EBM™-2 Endothelial Cell Growth Basal Medium-2 (EBM-2) medium (Lonza, CC-3156) supplemented with growth factors (EGM-2 Endothelial SingleQuots Kit, Lonza, CC-4176) and 1% fetal bovine serum (FBS) at 37°C in a humidified atmosphere with 5% CO_2.

Human dermal LECs (Innoprot, P10862, Lot#2841959) were cultured in VascuLife VEGF-MV Microvascular Endothelial Cell Growth Medium (Cell Systems, LL-0005) at 37°C in a humidified atmosphere with 5% CO_2.

Intestinal LECs were used for AQP1 overexpression and CTNNB1 knockdown, spheroid sprouting assays and proximity ligation assays. Dermal LECs were used for AQP1 overexpression, VPT assays, bulk RNA barcoding and sequencing (BRB-seq), β-catenin immunofluorescence staining, and F-actin distribution analysis.

Generation of AQP1-overexpressing LECs. Cells were transduced with lentiviral particles containing human *AQP1* cDNA under the EF1α promoter (pLV[Exp]-Puro-EF1A>FLAG/hAQP1[NM_198098.4], VectorBuilder). Control cells were transduced with lentiviral particles encoding enhanced blue fluorescent protein (*EBFP*). Briefly, LECs were seeded in 6-well plates (0.2×10^6 cells/well), and when they reached 70% confluency, they were first starved for FBS and growth factors for 2 hours, then incubated overnight with lentivirus at a multiplicity of infection 15 (MOI). The virus-containing medium was replaced with complete medium the following day. Stable cell lines were selected using puromycin (350 ng/ml; Sigma-Aldrich, P7255) for 3-5 days. Transduction efficiency of *AQP1* was confirmed by fluorescence microscopy and western blot.

CTNNB1 knockdown by siRNA transfection. Intestinal LECs were seeded on fibronectin-coated coverslips, allowed to attach overnight, and transfected with 30 nM CTNNB1-targeting siRNA (Stealth RNAi CTNNB1, VHS50822, Thermo Fisher Scientific, Waltham, MA, USA) or scrambled control siRNA using Lipofectamine RNAimax (Thermo Fisher Scientific) in Opti-MEM (Thermo Fisher Scientific) according to the manufacturer's instructions. The transfection mix was prepared by combining siRNA and Lipofectamine RNAimax in Opti-MEM, incubating for 20 minutes at room temperature, then adding to cells in EBM-2 medium without antibiotics. Six hours post-transfection, the medium was replaced with complete EBM-2 medium. Knockdown efficiency was validated by Western blot analysis 48 hours post-transfection.

Osmotic stress treatments. Normosmotic medium was standard EBM-2 complete medium (~300 mOsm/kg). Hyperosmotic medium was prepared by adding D-sorbitol (200 mM; Sigma-Aldrich, S1876) to EBM-2 complete medium, increasing the osmolality by 200 mOsm/kg to achieve final osmolality of ~500 mOsm/kg, approximating the osmotic conditions at the villus tip during nutrient absorption (Hallbäck et al., 1991). Hypoosmotic medium was prepared by 30% dilution of complete EBM-2 with sterile distilled water.

Hydrostatic pressure experiments. Dermal LEC responses to mechanical stress, were assessed by subjecting cells to hydrostatic pressure using a custom-built pressure bioreactor system (Al-Nuaimi et al., 2024). The setup consisted of columns of cell culture medium connected to the culture chamber to generate static pressure of 2 mmHg, a value consistent with physiological pressure in lymphatic vessels

due to gravity (Sloas et al., 2016). LEC monolayers were subjected to pressure stimulation for 24 hours at 37°C with 5% CO_2, with 0 mmHg (atmospheric pressure) serving as control. Following pressure treatment, cells were either extracted for RNA to assess *AQP1* levels or fixed and processed for immunofluorescence staining as described in the immunofluorescence microscopy section.

Western blot **analysis.** Cells (*EBFP*^{OE} control and *AQP1*^{OE}) were lysed in RIPA buffer with protease inhibitors, and protein concentration was determined by BCA assay. Equal amounts of protein (10 µg) were separated by SDS-PAGE (4–15% Mini-PROTEAN® TGX™ Precast Protein Gels, 15-well, 15 µl, BioRad, 4561086) and transferred to PVDF membranes using Fast Blotter (Thermo Scientific Pierce G2). Membranes were blocked with 5% BSA in TBST for 1 hour at RT, then incubated with primary antibodies against β-catenin (BD Biosciences, 610154; 1:1,000) or histone H3 (Cell Signaling Technologies, 9715) overnight at 4°C. After washing, membranes were incubated with HRP-conjugated goat anti-rabbit IgG (Dako, P0448; 1:10,000) for1 hour at RT. Protein bands were visualized using Super signal West Femto Max sensitivity substrate (Thermo Fischer, 34096). Band intensities were quantified using ImageJ/Fiji. β-catenin levels were normalized to histone H3 loading control.

Lymphangiogenic sprouting assays

Spheroid sprouting assay

Spheroid formation. The spheroid sprouting protocol was adapted from (Korff and Augustin, 1999). LECs were suspended at 800 cells per spheroid in a mixture of 72% EBM-2 complete medium, 8% FBS, and 20% methylcellulose stock solution (2% methylcellulose (Sigma-Aldrich, M7027) in Medium 199 with GlutaMAX™). Aliquots of 100 µl were dispensed into each well of non–tissue culture-treated 96-well round-bottom plates and incubated overnight at 37 °C with 5% CO_2 to form spheroids.

Fibrin gel embedding and culture. After 20 hours, 5-7 spheroids were collected and mixed in a fibrin gel composed of 2.5 mg/ml fibrinogen (Sigma, F8630) in EBM-2 complete medium, supplemented with aprotinin (final concentration 0.1 U/ml; Sigma, A1153) and either bovine serum albumin (BSA) or VEGF-C at 100 ng/ml. Gelation was initiated by adding 30 µl thrombin (final concentration 0.625 U/ml; Sigma, T9549) to the spheroid-fibrinogen mixture (570 µl) in pre-warmed 24-well plates. The mixture was gently mixed and incubated for 10-15 minutes at room temperature and 37 °C for 45 minutes. After gel formation, 600 µl of EBM-2 medium with 30,000 human intestinal fibroblasts was added per well, and plates were incubated for 48 hours at 37°C with 5% CO_2. To minimize variability, spheroids for all conditions within each replicate were embedded in the same 24-well plate using the same batch of fibrin gel. Normosmotic, hyperosmotic, and hypoosmotic conditions were established by adjusting the osmolality of the added culture medium (600 µl) as described in the osmotic stress treatments section above.

Staining, imaging and analysis. After 48 hours, spheroids were fixed with 4% PFA for 15 minutes, permeabilized with 0.3% Triton X-100 in PBS for 10 minutes, and stained with Alexa Fluor 488-phalloidin (1:400; Invitrogen) and Hoechst dye (1 μg/ml; Sigma-Aldrich) to visualize F-actin and nuclei. Spheroids were imaged with a Nikon Ti2 confocal laser scanning microscope equipped with a 20x objective.

Images were analyzed in ImageJ by measuring the distance from the spheroid core edge to the sprout tip. For each replicate, the mean sprout length was calculated from 3-6 spheroids, and this mean value was used as a single measurement per replicate (n=4 replicates). The mean sprout length was normalized to the control condition ($EBFP^{OE}$, normosmotic, BSA-treated). For detailed morphological analysis, sprouting responses were categorized into nucleated sprouts (containing ≥1 nucleus, indicating cellular migration) and anucleated protrusions (membrane extensions without nuclear content). Nuclei were identified by Hoechst staining, and each protrusion was classified based on the presence or absence of nuclear material along its length. Cell density within established sprouts was assessed by quantifying the number of nuclei per 100 μm sprout length. For this analysis, only nucleated sprouts were measured. The number of Hoechst-positive nuclei within each sprout was counted, and the sprout length measured from core to tip. Cell density was calculated as: (number of nuclei / sprout length in μm) x 100. Total sprout length per spheroid was calculated by summing the lengths of all nucleated sprouts originating from a single spheroid core.

VPT sprouting assay

To validate sprouting responses in the presence of interstitial flow, we used Vascular Phenotypic and Proteomic (VPT) devices as described (Jung et al., 2024). Microscale fluid patterning within the microfluidic devices was initiated immediately following air plasma treatment, proceeding sequentially through the center channel (channel C), side channel (channel S), and open channel (channel O). All solutions were introduced via spontaneous capillary flow. To generate stable fibrin hydrogels for the 3D sprouting assay, human fibrinogen (10 mg/mL, Sigma-Aldrich, F4883) was supplemented with aprotinin (0.1 U/mL, Sigma-Aldrich, A1153) at a 25:4 (v/v) ratio to prevent proteolytic degradation during culture. For channel C, 2.0 μL of an acellular fibrinogen and thrombin (Sigma-Aldrich, 605195) mixture was introduced, yielding a final fibrinogen concentration of 5 mg/mL. The hydrogel was allowed to polymerize for 13 min prior to patterning channel S. Channel S was subsequently patterned along the inner edge with 7.5 μL of a cellular fibrinogen-thrombin mixture containing human fibroblasts ($6x10^6$ cells/mL) at a final fibrinogen concentration of 2.5 mg/mL. For channel O, 30 μL of a cell suspension (control $EBFP^{OE}$ or $AQP1^{OE}$ human dermal LECs, 30,000 cells per device) was injected through the inlet to promote cell attachment at the hydrogel interface. Culture medium was then added with final volumes of up to 200 μL and 140 μL per reservoir on the channel S and channel O sides,

respectively. Hydrostatic pressure–driven flow was established by maintaining a media height difference between opposing reservoirs. Devices were cultured for 48 hours under either normosmotic (300 mOsm) or hyperosmotic (500 mOsm) conditions. Following culture, samples were fixed in 4% paraformaldehyde for 30 min and stained with phalloidin and Hoechst. Confocal microscopy was used for image acquisition, and sprout number, sprout length, and nuclei per sprout were quantified from three independent experiments (n = 3).

Proximity ligation assay (PLA)

PLA was performed according to the manufacturer's protocol (Duolink Proximity Ligation Assay, Sigma-Aldrich, DUO92008). Intestinal LECs were seeded on glass coverslips in 24-well plates and cultured in normosmotic (300 mOsm) or hyperosmotic (500 mOsm) medium for 48 hours. Cells were fixed with 4% paraformaldehyde (PFA) in PBS containing 0.1% $CaCl_2$ and 0.05% $MgCl_2$ for 15 minutes at room temperature, permeabilized with 0.1% Triton X-100 in PBS for 10 minutes, and blocked with 0.5% BSA and 0.1% Triton X-100 in PBS for 1 hour at room temperature.

Cells were incubated overnight at 4°C with primary antibodies against AQP1 (Sigma-Aldrich, AB3272) and β-catenin (BD Biosciences, 610154). After washing with PBS, PLA probes anti-rabbit Minus (Sigma-Aldrich, DUO92005) and anti-mouse Plus (Sigma-Aldrich, DUO92003) were applied according to the manufacturer's protocol. Ligation and amplification reactions were performed following the kit instructions. Negative controls included: (1) single primary antibody only (AQP1 alone or β-catenin alone) with both PLA probes, (2) no primary antibodies with PLA probes, and (3) unstimulated cells (no osmotic stress) to establish baseline interaction levels. Nuclei were counterstained with DAPI (0.2 μg/ml) for 5 minutes. Coverslips were washed and mounted using (Sigma-Aldrich, DUO82040). PLA signals appear as discrete red fluorescent puncta when the two proteins are within <40 nm proximity.

Quantification: PLA signals were imaged using confocal microscopy. Images were processed in ImageJ/Fiji. For automated counting of PLA puncta, a threshold was applied to the PLA channel, and puncta were counted using the "Analyze Particles" function with size constraints to exclude background noise and cell debris. The number of PLA puncta per cell was quantified and averaged across all cells for each condition.

Gene expression analysis by RT-qPCR

Total RNA was isolated using the RNeasy Micro Kit (Qiagen, 74034). The concentration and quality of the isolated RNA were assessed using an Agilent 2100 Bioanalyzer. For samples with low RNA

input from FACS sorted LECs, mRNA was amplified using the Ovation Pico WTA System V2 (NuGEN) prior to cDNA synthesis. Reverse transcription was performed using the Transcriptor First Strand cDNA Synthesis Kit (Roche Diagnostics, 04379012001).

Quantitative real-time PCR (RT-qPCR) analyses were conducted using the StepOnePlus Real-Time PCR System (Applied Biosystems) with SYBR Green PCR Master Mix (Thermo Fisher Scientific). Primers were used at a final concentration of 100 nM. For validation of Aqp1 deletion in intestinal LECs, primers flanking exons 2 and 3 of the *Aqp1* gene (Zhang et al., 2016) (Table S4) were employed to confirm the deletion of this region in tamoxifen-induced $Aqp1^{i\Delta LEC}$ samples. For validation of bulk RNA-sequencing results, gene-specific primers targeting SGK1, ZFP36L1, and PKN1 were used (Table S4). The housekeeping genes 18S or RPL27 were used as an internal control, and results were presented as relative expression levels normalized to control samples using the $2^{-\Delta\Delta Ct}$ method.

Bulk RNA barcoding and sequencing (BRB-seq) analysis

Experimental design and sample preparation. Human dermal LECs were transduced with lentiviral vectors expressing either enhanced blue fluorescent protein (EBFP, control) or human *AQP1* ($AQP1^{OE}$). Cells were cultured under normosmotic (300 mOsm) or hyperosmotic (500 mOsm) conditions for 8 hours prior to harvest, washed twice with PBS and harvested for RNA isolation. Two biological replicates were prepared per condition.

RNA isolation and quality control. Total RNA was isolated using the RNeasy Mini Kit (QIAGEN, Hilden, Germany, 74104) following the manufacturer's instructions. RNA quantity and quality were assessed using a NanoDrop spectrophotometer, and RNA concentration was normalized to 100 ng/µl prior to library preparation.

Library preparation and sequencing. Alithea Genomics SA (Lausanne, Switzerland) prepared libraries and sequenced samples using highly multiplexed 3′-end bulk RNA barcoding and sequencing (MERCURIUS™ BRB-seq service) (Alpern et al., 2019). BRB-seq libraries were generated using the MERCURIUS™ BRB-seq library preparation kit for Illumina (v5D barcode set for 96 samples, 10813, Alithea Genomics) following the manufacturer's protocol and sequenced on an AVITI sequencing platform in paired-end mode (Element Biosciences, San Diego, CA, USA).

Read alignment, demultiplexing, and quantification. Raw sequencing reads were processed using STARsolo v2.7.9a for sample demultiplexing, alignment to the human reference genome (GRCh38, Ensembl release 104), and gene expression quantification. Alignment was performed using the parameters "--soloUMIdedup NoDedup", "1MM_Directional" and "-- quantMode GeneCounts" to generate count matrices of both raw reads and of reads deduplicated using Unique Molecular Identifiers (UMI).

Differential gene expression analysis. Raw UMI count matrices were imported into R version 4.3.0 for statistical analysis. Differential gene expression analysis was performed using DESeq2 v1.40.2 (Love et al., 2014). Genes with adjusted p-value < 0.05 and |log2 fold change| > 0.6 were considered differentially expressed.

Definition of rescued genes. Genes dysregulated by hyperosmotic stress (500 mOsm vs 300 mOsm in EBFP control cells) that showed restored expression upon *AQP1* overexpression under hyperosmotic conditions were defined as "rescued genes." Specifically, genes were classified as rescued if: (1) they were significantly altered (|log2 fold change| > 0.6 and adjusted p < 0.05) by hyperosmotic treatment in control cells, and (2) their expression in $AQP1^{OE}$ cells under hyperosmotic conditions was not significantly different (adjusted p > 0.05) and/or |log2 fold change| < 0.6 from control cells under normosmotic conditions. Genes showing partial rescue (25-99% normalization in absolute fold-change toward baseline) were categorized separately.

Single-cell transcriptomic analysis

scRNA-seq library preparation, sequencing and pre-processing. Sorted LECs (~10,000 cells per sample) were loaded into the Chromium Controller (10x Genomics) using the Single Cell 3' Library & Gel Bead Kit v3. Libraries were prepared following the manufacturer's protocol. Paired-end sequencing was performed on Illumina HiSeq 2500 (150 cycles) and Illumina NovaSeq 6000 (100 cycles) devices at the Lausanne Genomics Technology Facility to achieve a depth of at least 50,000 reads per cell. Raw sequencing reads were aligned to the mm10 mouse reference genome (v. mm10-3.1-0 of the transcriptome reference provided by 10x Genomics), number of reads were summarized per gene, and cells were called using Cell Ranger software (v3.1.0, 10x Genomics).

Data acquisition and integration. Our scRNA-seq data (samples 1–5) was integrated with three publicly available datasets (samples 6-8, Table S1). Raw count matrices of all datasets were imported into R v4.1.2 for further analysis. Each dataset was ln-normalized with a scale factor of 10,000, followed by variable gene detection using the Seurat package v4.3.0 (Hao et al., 2021). LECs were identified based on the expression of canonical markers ($Flt1^-$, $Pecam1^+$, $Prox1^+$, and $Flt4^+$). To ensure data quality, cells with mitochondrial gene expression exceeding 5% and dissociation-related genes (van den Brink et al., 2017) exceeding 6% were filtered out. Integration of retained cells was performed using the anchor correspondence method implemented in the Seurat package v4.3.0, using 30 dimensions and 60 nearest neighbours as input parameters (Hao et al., 2021; Stuart et al., 2019).

Unsupervised clustering and visualization. Dimensionality reduction was performed using principal component analysis (PCA) on the top 2000 variable genes, followed by Uniform Manifold Approximation and Projection (UMAP) for visualization, using 25 principal components as input.

Clustering was achieved using a shared nearest neighbour (SNN), Louvain modularity optimization-based clustering algorithm, with 25 principal components, 20 nearest neighbours and a resolution of 0.3 as input. Cell types were annotated based on the expression of canonical markers, identifying three distinct LEC populations (Table S1).

Differential gene expression, pathway and similarity analysis. Differential gene expression within each cluster compared to all other cells was assessed using the FindAllMarkers function of the Seurat package, which implements a Wilcoxon rank-sum test with Bonferroni correction for multiple comparisons. Genes with adjusted p-values < 0.05 were considered significantly differentially expressed. Visualization tools within Seurat, such as dot plots and violin plots, were used to display gene expression patterns. Over-representation analysis of Gene Ontology (GO) Biological Process terms was performed by separating the significantly up- and down-regulated genes in each cluster with the enrichGO function of the clusterProfiler package v4.2.2 (Ashburner et al., 2000; Yu et al., 2012; The Gene Ontology Consortium, 2019). We manually parsed the list of significant GO terms to remove terms that had redundant gene content, or shared ancestor terms, and calculated a module score of the genes of each selected GO term per cell, using the AddModuleScore (Tirosh et al., 2016) function of the Seurat package. The average module score per cluster per GO term was calculated and displayed as a heatmap using the ComplexHeatmap package v2.10.0 (Gu et al., 2016) for R.

We investigated whether intestinal LECs expressed gene signatures of LECs from other organs such as the mesentery, the skin and the lymph node. To this end, we obtained transcriptomics data from the respective organs. For each mesenteric (González-Loyola et al., 2021) or dermal LEC subtype (Petkova et al., 2023), the FindAllMarkers function was used to define a signature consisting of 50 marker genes up-regulated in each LEC subtype. For lymph node LEC gene signatures, we used the marker genes described in Figure 5B from Xiang et al. (Xiang et al., 2020). The AddModuleScore function was used to evaluate the expression magnitude of the mesenteric, dermal or lymph node LEC marker genes per cell, and the median module score per gene signature per cluster displayed using the ComplexHeatmap package. Finally, we assessed transcription factor activity per cell using the SCENIC implementation for R v.1.3.1, using default parameters (Aibar et al., 2017).

Immunohistochemistry and imaging

Tissue preparation and staining. Mice were terminally sedated and intracardially perfused first with PBS and then with 4% PFA (158127, Sigma-Aldrich) to fix the tissues. Preparation of whole-mounted tissues, cryosections, and paraffin sections were performed as previously described in (Bernier-Latmani and Petrova, 2016). In brief, the small intestine was dissected between the stomach and cecum, flushed with cold PBS, opened longitudinally, and pinned flat. Tissues were fixed in 4% PFA (paraffin sections) or 0.5% PFA with picric acid and sodium phosphate (whole-mounts and cryosections) overnight at 4°C.

For embryonic tissues, skin (E16.5) and mesenteries (E18.5) were fixed in 4% PFA for 2 hours at room temperature, washed three times with PBS, and immediately proceeded to immunostaining. Cryosections were cut at 10 µm (gut) or 8 µm (LN), and paraffin sections at 4 µm. Sections were permeabilized with 0.3% Triton X-100, blocked with 0.5% BSA, and incubated with primary antibodies (Table S4) overnight at 4°C. After PBS washes, sections were stained with Alexa Fluor-conjugated secondary antibodies for 1 hour (sections) or overnight (whole-mounts). DAPI was added for nuclear staining. Samples were mounted in Fluoromount-G (sections) or Histodenz (whole-mounts).

Multiplex immunohistochemistry. Multiplex immunohistochemistry was performed on paraffin-embedded tissue sections. After the initial round of primary antibody staining and imaging, coverslips were removed by incubating the sections in PBS 1x with gentle rocking and sections were incubated with elution buffer composed of 0.5 M glycine, 3 M guanidinium chloride, 3 M urea and 40 mM tris(2-carboxyethyl) phosphine in distilled water for 4 min at RT. Following elution and washes, sections were incubated with a second set of primary antibodies for a second round of staining.

Immunostaining of cells. LECs seeded on glass coverslips in 24-well plates, were fixed with 4% PFA in PBS containing 0.1% $CaCl_2$ and 0.05% $MgCl_2$, permeabilized with 0.1% Triton X-100 (AppliChem, A1388) in PBS and blocked with a solution of 0.5% BSA (AppliChem, A1391) and 0.1% Triton X-100 in PBS for 1 hour at room temperature. Coverslips were incubated with primary antibodies (Table S4) incubated overnight at 4 °C, washed with PBS, incubated with Alexa Fluor-conjugated secondary antibodies (Thermo Fisher Scientific) supplemented with DAPI (0.2 µg/ml) for 1 hour on a shaking platform at room temperature, washed and mounted using Fluoromount-G mounting medium.

Imaging and analysis. Confocal imaging was performed using Zeiss LSM 880 with Airyscan (Zen Black software), Nikon Ti2 Yokogawa CSU-W1 Spinning Disk (Nikon NIS-Elements AR 5.0 software), Zeiss Imager Z1 (Zeiss Axiovision SE64 rel 4.9.1 software), and Hamamatsu NanoZoomer S60 (NDP.view2 software). We used ImageJ Fiji for image analysis.

Collateral vessel quantification in mesenteric lymphatics. Mesenteric collecting lymphatic vessels from *Foxc2*^{lecko} and *Aqp1;Foxc2*^{lecko} mice, were prepared as described above. Lymphatic valves were identified by PROX1high valve cells. Collateral vessels were defined as PROX1+ cellular protrusions extending from the valve region. The percentage of valves with one or more collateral sprouts was quantified.

Quantification of YFP+ cells in mosaic lacteals. For mosaic *Aqp1* deletion analysis, whole-mount intestinal tissues from *Rosa26-EYFP; Aqp1*$^{i\Delta LEC}$ and control mice were processed as described above. The total number of LECs per lacteal was determined by counting PROX1+ nuclei within the LYVE1+ lacteal boundary. YFP+ LECs were identified by co-localization of YFP signal with PROX1+ nuclei, and the percentage of YFP+ LECs was calculated as: (number of YFP+ PROX1+ cells / total PROX1+ cells) x 100 for each lacteal. For spatial distribution analysis, each lacteal was segmented into five equal

positional bins (0-20%, 20-40%, 40-60%, 60-80%, and 80-100% of total lacteal length from base to tip). Lacteal length was measured from base (crypt-associated region) to tip (villus apex) along the vessel centerline. Each YFP+ PROX1+ cell was assigned to the corresponding bin based on its position along the base-to-tip axis. The proportion of YFP+ cells in each positional bin was calculated as: (number of YFP+ cells in bin / total YFP+ cells in the entire lacteal) x 100.

F-actin distribution analysis. For each cell, a straight line was drawn from the cell edge to the center, and F-actin fluorescence intensity along this line was measured using the "Plot Profile" function in ImageJ (NIH, Bethesda, MD, USA). The line length was normalized to 100 arbitrary units, and intensity values were extracted at regular intervals every 5% of the normalized distance. Intensity profiles from multiple cells were averaged to generate a mean F-actin distribution curve for each condition.

β-catenin quantification. An identical intensity threshold was applied across all conditions to define β-catenin-positive signal. Total β-catenin-positive area was measured and normalized to cell number. Values were normalized to the control condition (*EBFP*^{OE}, 300 mOsm).

Lymphatic malformation analysis. To quantify AQP1 and VEGFR3 co-expression, a threshold was first set on the VEGFR3 channel to delineate the total lymphatic vessel area, followed by a separate threshold for the AQP1 channel. The area of double-positive (AQP1^{+}VEGFR3^{+}) regions was then measured and divided by the total VEGFR3^{+} area. The same approach was used to determine the percentage of AQP1^{+}EMCN^{+} area. For LEC proliferation, thresholds were set for both PROX1 and KI67, and the number of double-positive PROX1^{+}KI67^{+} cells was normalized to the total number of PROX1^{+} cells. A threshold based on the Otsu algorithm was applied to the AQP1 channel to classify proliferating LECs (PROX1^{+}KI67^{+}) as AQP1^{+} or AQP1^{-}, based on whether the measured mean AQP1 intensity in each cell exceeded this threshold. Macrophages were quantified by applying a threshold to the CSF1R channel and counting the number of CSF1R^{+} cells, which was subsequently normalized to the total tissue area.

Statistical analysis

Data were analysed using Wolfram Mathematica (13.0), R (v4.1.2) and GraphPad Prism (8). All plotted values are presented as mean ± standard deviation (SD). For two-group comparisons, a one-sample, paired, Student's or Welsh's t-test was performed, as appropriate. For comparisons involving more than two groups, one-way ANOVA or two-way repeated-measures ANOVA was used, followed by Tukey's post hoc test or p-value corrections (Benjamini-Hochberg, Holm–Sidak, or Benjamini-Krieger-Yekutieli). The specific test used for each experiment are indicated in the figure legends. A p value <0.05 was considered statistically significant.

Online supplemental material

Fig. S1 is related to Fig. 1 and contains scRNA-seq integration, re-clustering details, and GO term enrichment for intestinal LEC subsets. Fig. S2 is related to Fig. 2 and provides AQP1 distribution across intestinal regions, validation of *Aqp1* deletion via FACS and qPCR, and re-analysis of published stromal and epithelial datasets. Fig. S3 is related to Fig. 3 and details the impact of antibiotic treatment on lacteal morphology and marker expression. Fig. S4 is related to Fig. 4 and Fig. 5 and describes in vitro LEC responses to osmotic and hydrostatic stress, including detailed spheroid and VPT sprouting assay quantifications. Fig. S5 is related to Fig. 6 and Fig. 7 and contains qPCR validation of transcriptomics, characterization of lymph node LEC subpopulations, and macrophage infiltration in lymphedema. Table S1 is related to Fig. 1 and lists scRNA-seq datasets and markers. Table S2 is related to Fig. 4 and provides comprehensive statistical comparisons for sprouting assays. Table S3 is related to Fig. 6 and includes BRB-seq differential gene expression data. Table S4 lists primers and antibodies. Source data for Fig. 4 and Fig. 5 are provided as separate files.

Data availability

The single-cell RNA sequencing data generated and analyzed in this study are available in the Gene Expression Omnibus (GEO) under accession numbers GSE288670 (cells from samples 1-3, Table S1) and GSE288925 (cells from samples 4 and 5, Table S1). The bulk RNA sequencing (BRB-seq) data are available in GEO under accession number GSE312554 (Table S3).

Acknowledgements

We thank Vedat Schwenger and Andreas Wagner for providing the *Aqp1*$^{fl/fl}$ mice, Kari Alitalo for generously sharing VEGF-C, Werner Held for providing anti-CD16/32 (2.4G2) hybridoma supernatant and Barbara Garmy-Susini for helpful discussions. We are grateful to Céline Beauverd for mouse genotyping and assistance with immunohistochemistry, to Katerina Pandeva for assistance with lentiviral transductions, and to Lucas Münzenmaier for technical assistance. We gratefully acknowledge the Histology, Flow Cytometry, Genomic Technologies, Animal, and Cellular Imaging Facilities at the University of Lausanne for their assistance. We also acknowledge the administrative support from the SOFT Foundry Institute at Seoul National University.

This work was supported by the European Union's Horizon 2020 research and innovation program Theralymph (grant agreement no. 847939) to TVP, AN and TM; the Swiss National Science Foundation (30105_156266 and 30105_212387) to TVP; Human Frontier Science Program (LT000074/2019-L) to

JK; the Muschamps Foundation and the Swiss National Science Foundation (CRSK-3_190435) to JBL; Human Frontier Science Program (LT000633/2020-L) to SA-M; European Union's Horizon 2020 research and innovation programme under the Marie Skłodowska-Curie grant agreement No 814316 to HS and TM; and the Fonds de la Recherche Scientifique-FNRS (F.R.S.-FNRS, Belgium) to AN. The authors have no conflicts of interest to declare.

Author contributions: I. Roci: conceptualization, data curation, formal analysis, investigation, methodology, software, validation, visualization, writing — original draft, writing — review and editing. J. Kim: conceptualization, investigation, visualization, writing — original draft, writing — review and editing. K. de Korodi: data curation, formal analysis, investigation, writing — review and editing. T. Wyss: formal analysis, visualization, writing — original draft, writing — review and editing. J. Bernier-Latmani: investigation, writing — original draft, writing — review and editing. S. Arroz-Madeira: investigation, writing — review and editing. A. González-Loyola: investigation, visualization, writing — review and editing. E. Bovay: investigation, writing — review and editing. N. Grenningloh: investigation, writing — review and editing. H. Schoofs: resources, , writing — review and editing. N.L. Jeon: methodology, writing — review and editing. C. Giampietro: formal analysis, investigation, writing — review and editing. T. Mäkinen: funding acquisition, resources, writing — review and editing. A. Noël: funding acquisition, methodology, resources, writing — review and editing. T.V. Petrova: conceptualization, funding acquisition, project administration, resources, supervision, writing — original draft, writing — review and editing.

References

Abu Taha, A., and H.-J. Schnittler. 2014. Dynamics between actin and the VE-cadherin/catenin complex. *Cell Adh. Migr.* 8:125–135. doi:10.4161/cam.28243.

Agre, P., L.S. King, M. Yasui, W.B. Guggino, O.P. Ottersen, Y. Fujiyoshi, A. Engel, and S. Nielsen. 2002. Aquaporin water channels – from atomic structure to clinical medicine. *J. Physiol.* 542:3–16. doi:10.1113/jphysiol.2002.020818.

Agre, P., G.M. Preston, B.L. Smith, J.S. Jung, S. Raina, C. Moon, W.B. Guggino, and S. Nielsen. 1993. Aquaporin CHIP: the archetypal molecular water channel. *American Journal of Physiology-Renal Physiology*. 265:F463–F476. doi:10.1152/ajprenal.1993.265.4.F463.

Aibar, S., C.B. González-Blas, T. Moerman, V.A. Huynh-Thu, H. Imrichova, G. Hulselmans, F. Rambow, J.-C. Marine, P. Geurts, J. Aerts, J. van den Oord, Z.K. Atak, J. Wouters, and S. Aerts. 2017. SCENIC: single-cell regulatory network inference and clustering. *Nat. Methods*. 14:1083–1086. doi:10.1038/nmeth.4463.

Alitalo, K. 2011. The lymphatic vasculature in disease. *Nat. Med.* 17:1371–1380. doi:10.1038/nm.2545.

Al-Nuaimi, D.A., D. Rütsche, A. Abukar, P. Hiebert, D. Zanetti, N. Cesarovic, V. Falk, S. Werner, E. Mazza, and C. Giampietro. 2024. Hydrostatic pressure drives sprouting angiogenesis via adherens junction remodelling and YAP signalling. *Commun. Biol.* 7:940. doi:10.1038/s42003-024-06604-9.

Alpern, D., V. Gardeux, J. Russeil, B. Mangeat, A.C.A. Meireles-Filho, R. Breysse, D. Hacker, and B. Deplancke. 2019. BRB-seq: ultra-affordable high-throughput transcriptomics enabled by bulk RNA barcoding and sequencing. *Genome Biol.* 20:71. doi:10.1186/s13059-019-1671-x.

Ashburner, M., C.A. Ball, J.A. Blake, D. Botstein, H. Butler, J.M. Cherry, A.P. Davis, K. Dolinski, S.S. Dwight, J.T. Eppig, M.A. Harris, D.P. Hill, L. Issel-Tarver, A. Kasarskis, S. Lewis, J.C. Matese, J.E. Richardson, M. Ringwald, G.M. Rubin, and G. Sherlock. 2000. Gene Ontology: tool for the unification of biology. *Nat. Genet.* 25:25–29. doi:10.1038/75556.

Augustin, H.G., and G.Y. Koh. 2017. Organotypic vasculature: From descriptive heterogeneity to functional pathophysiology. *Science (1979).* 357. doi:10.1126/science.aal2379.

Bazigou, E., O.T.A. Lyons, A. Smith, G.E. Venn, C. Cope, N.A. Brown, and T. Makinen. 2011. Genes regulating lymphangiogenesis control venous valve formation and maintenance in mice. *Journal of Clinical Investigation*. 121:2984–2992. doi:10.1172/JCI58050.

Bernier-Latmani, J., C. Cisarovsky, C.S. Demir, M. Bruand, M. Jaquet, S. Davanture, S. Ragusa, S. Siegert, O. Dormond, R. Benedito, F. Radtke, S.A. Luther, and T. V. Petrova. 2015. DLL4 promotes continuous adult intestinal lacteal regeneration and dietary fat transport. *Journal of Clinical Investigation*. 125:4572–4586. doi:10.1172/JCI82045.

Bernier-Latmani, J., A. González-Loyola, and T. V. Petrova. 2024. Mechanisms and functions of intestinal vascular specialization. *Journal of Experimental Medicine*. 221. doi:10.1084/jem.20222008.

Bernier-Latmani, J., C. Mauri, R. Marcone, F. Renevey, S. Durot, L. He, M. Vanlandewijck, C. Maclachlan, S. Davanture, N. Zamboni, G.W. Knott, S.A. Luther, C. Betsholtz, M. Delorenzi, C. Brisken, and T. V. Petrova. 2022. ADAMTS18+ villus tip telocytes maintain a polarized VEGFA signaling domain and fenestrations in nutrient-absorbing intestinal blood vessels. *Nat. Commun.* 13:3983. doi:10.1038/s41467-022-31571-2.

Bernier-Latmani, J., and T. V Petrova. 2016. High-resolution 3D analysis of mouse small-intestinal stroma. *Nat. Protoc.* 11:1617–1629. doi:10.1038/nprot.2016.092.

Bernier-Latmani, J., and T. V. Petrova. 2017. Intestinal lymphatic vasculature: structure, mechanisms and functions. *Nat. Rev. Gastroenterol. Hepatol.* 14:510–526. doi:10.1038/nrgastro.2017.79.

Bovay, E., A. Sabine, B. Prat-Luri, S. Kim, K. Son, A.-H. Willrodt, C. Olsson, C. Halin, F. Kiefer, C. Betsholtz, N.L. Jeon, S.A. Luther, and T. V. Petrova. 2018. Multiple roles of lymphatic vessels in peripheral lymph node development. *Journal of Experimental Medicine*. 215:2760–2777. doi:10.1084/jem.20180217.

Bowman, C., and S.G. Rockson. 2024. The Role of Inflammation in Lymphedema: A Narrative Review of Pathogenesis and Opportunities for Therapeutic Intervention. *Int. J. Mol. Sci.* 25:3907. doi:10.3390/ijms25073907.

van den Brink, S.C., F. Sage, Á. Vértesy, B. Spanjaard, J. Peterson-Maduro, C.S. Baron, C. Robin, and A. van Oudenaarden. 2017. Single-cell sequencing reveals dissociation-induced gene expression in tissue subpopulations. *Nat. Methods*. 14:935–936. doi:10.1038/nmeth.4437.

Buntinx, F., A. Lebeau, L. Gillot, L. Baudin, R. Ndong Penda, F. Morfoisse, F. Lallemand, G. Vottero, C. Nizet, J.L. Nizet, S. Blacher, and A. Noel. 2022. Single and combined impacts of irradiation and surgery on lymphatic vasculature and fibrosis associated to secondary lymphedema. *Front. Pharmacol.* 13. doi:10.3389/fphar.2022.1016138.

Burg, M.B., J.D. Ferraris, and N.I. Dmitrieva. 2007. Cellular Response to Hyperosmotic Stresses. *Physiol. Rev.* 87:1441–1474. doi:10.1152/physrev.00056.2006.

Cao, J., M. Ehling, S. März, J. Seebach, K. Tarbashevich, T. Sixta, M.E. Pitulescu, A.-C. Werner, B. Flach, E. Montanez, E. Raz, R.H. Adams, and H. Schnittler. 2017. Polarized actin and VE-cadherin dynamics regulate junctional remodelling and cell migration during sprouting angiogenesis. *Nat. Commun.* 8:2210. doi:10.1038/s41467-017-02373-8.

Carter, E.P., B.P. Ölveczky, M.A. Matthay, and A.S. Verkman. 1998. High Microvascular Endothelial Water Permeability in Mouse Lung Measured by a Pleural Surface Fluorescence Method. *Biophys. J.* 74:2121–2128. doi:10.1016/S0006-3495(98)77919-6.

Castel, P., F.J. Carmona, J. Grego-Bessa, M.F. Berger, A. Viale, K. V. Anderson, S. Bague, M. Scaltriti, C.R. Antonescu, E. Baselga, and J. Baselga. 2016. Somatic PIK3CA mutations as a driver of sporadic venous malformations. *Sci. Transl. Med.* 8. doi:10.1126/scitranslmed.aaf1164.

Cecchini, M.G., M.G. Dominguez, S. Mocci, A. Wetterwald, R. Felix, H. Fleisch, O. Chisholm, W. Hofstetter, J.W. Pollard, and E.R. Stanley. 1994. Role of colony stimulating factor-1 in the establishment and regulation of tissue

macrophages during postnatal development of the mouse. *Development*. 120:1357–1372. doi:10.1242/dev.120.6.1357.

Chen, L., A. Mupo, T. Huynh, S. Cioffi, M. Woods, C. Jin, W. McKeehan, L. Thompson-Snipes, A. Baldini, and E. Illingworth. 2010. Tbx1 regulates *Vegfr3* and is required for lymphatic vessel development. *Journal of Cell Biology*. 189:417–424. doi:10.1083/jcb.200912037.

Di Ciano, C., Z. Nie, K. Szászi, A. Lewis, T. Uruno, X. Zhan, O.D. Rotstein, A. Mak, and A. Kapus. 2002. Osmotic stress-induced remodeling of the cortical cytoskeleton. *American Journal of Physiology-Cell Physiology*. 283:C850–C865. doi:10.1152/ajpcell.00018.2002.

Cursiefen, C., L. Chen, L.P. Borges, D. Jackson, J. Cao, C. Radziejewski, P.A. D'Amore, M.R. Dana, S.J. Wiegand, and J.W. Streilein. 2004. VEGF-A stimulates lymphangiogenesis and hemangiogenesis in inflammatory neovascularization via macrophage recruitment. *Journal of Clinical Investigation*. 113:1040–1050. doi:10.1172/JCI20465.

Deng, Y., X. Zhang, and M. Simons. 2015. Molecular Controls of Lymphatic VEGFR3 Signaling. *Arterioscler. Thromb. Vasc. Biol.* 35:421–429. doi:10.1161/ATVBAHA.114.304881.

Egorov, V.I., I. V. Schastlivtsev, E. V. Prut, A.O. Baranov, and R.A. Turusov. 2002. Mechanical properties of the human gastrointestinal tract. *J. Biomech.* 35:1417–1425. doi:10.1016/S0021-9290(02)00084-2.

Eser, S., N. Reiff, M. Messer, B. Seidler, K. Gottschalk, M. Dobler, M. Hieber, A. Arbeiter, S. Klein, B. Kong, C.W. Michalski, A.M. Schlitter, I. Esposito, A.J. Kind, L. Rad, A.E. Schnieke, M. Baccarini, D.R. Alessi, R. Rad, R.M. Schmid, G. Schneider, and D. Saur. 2013. Selective Requirement of PI3K/PDK1 Signaling for Kras Oncogene-Driven Pancreatic Cell Plasticity and Cancer. *Cancer Cell*. 23:406–420. doi:10.1016/j.ccr.2013.01.023.

Fernandes, L.M., D. Griswold-Wheeler, J.D. Tresemer, A. Vallejo, N. Vishlaghi, B. Levi, A. Shapiro, J.P. Scallan, and M.T. Dellinger. 2025. A single-cell atlas of normal and KRASG12D-malformed lymphatic vessels. *JCI Insight*. 10. doi:10.1172/jci.insight.185181.

Friess, A.E. 1977. Macrophage-lymphocyte cluster formation in the medullary sinus of lymph node after immunization with sheep red blood cells (SRBC). *Cell Tissue Res.* 180. doi:10.1007/BF00220171.

Fujimoto, N., Y. He, M. D'Addio, C. Tacconi, M. Detmar, and L.C. Dieterich. 2020. Single-cell mapping reveals new markers and functions of lymphatic endothelial cells in lymph nodes. *PLoS Biol.* 18:e3000704. doi:10.1371/journal.pbio.3000704.

Furuhashi, M., and G.S. Hotamisligil. 2008. Fatty acid-binding proteins: role in metabolic diseases and potential as drug targets. *Nat. Rev. Drug Discov.* 7:489–503. doi:10.1038/nrd2589.

Furuya, M., S.B. Kirschbaum, A. Paulovich, B.U. Pauli, H. Zhang, J.S. Alexander, A.G. Farr, and A. Ruddell. 2010. Lymphatic Endothelial Murine Chloride Channel Calcium-Activated 1 Is a Ligand for Leukocyte LFA-1 and Mac-1. *The Journal of Immunology*. 185:5769–5777. doi:10.4049/jimmunol.1002226.

Gandhi, R., R.C. Elble, A.D. Gruber, K.D. Schreur, H.-L. Ji, C.M. Fuller, and B.U. Pauli. 1998. Molecular and Functional Characterization of a Calcium-sensitive Chloride Channel from Mouse Lung. *Journal of Biological Chemistry*. 273:32096–32101. doi:10.1074/jbc.273.48.32096.

Gannon, B.J., and C.J. Carati. 2003. Endothelial Distribution of the Membrane Water Channel Molecule Aquaporin-1: Implications for Tissue and Lymph Fluid Physiology? *Lymphat. Res. Biol.* 1:55–66. doi:10.1089/15396850360495709.

Garlanda, C., B. Bottazzi, A. Bastone, and A. Mantovani. 2005. Pentraxins at the Crossroads between Innate Immunity, Inflammation, Matrix Deposition, and Female Fertility. *Annu. Rev. Immunol.* 23:337–366. doi:10.1146/annurev.immunol.23.021704.115756.

Geldhof, V., L.P.M.H. de Rooij, L. Sokol, J. Amersfoort, M. De Schepper, K. Rohlenova, G. Hoste, A. Vanderstichele, A.-M. Delsupehe, E. Isnaldi, N. Dai, F. Taverna, S. Khan, A.-C.K. Truong, L.-A. Teuwen, F. Richard, L. Treps, A. Smeets, I. Nevelsteen, B. Weynand, S. Vinckier, L. Schoonjans, J. Kalucka, C. Desmedt, P. Neven, M. Mazzone, G. Floris, K. Punie, M. Dewerchin, G. Eelen, H. Wildiers, X. Li, Y. Luo, and P. Carmeliet. 2022. Single cell atlas identifies lipid-processing and immunomodulatory endothelial cells in healthy and malignant breast. *Nat. Commun.* 13:5511. doi:10.1038/s41467-022-33052-y.

Ghanta, S., D.A. Cuzzone, J.S. Torrisi, N.J. Albano, W.J. Joseph, I.L. Savetsky, J.C. Gardenier, D. Chang, J.C. Zampell, and B.J. Mehrara. 2015. Regulation of inflammation and fibrosis by macrophages in lymphedema. *American Journal of Physiology-Heart and Circulatory Physiology*. 308:H1065–H1077. doi:10.1152/ajpheart.00598.2014.

González-Loyola, A., J. Bernier-Latmani, I. Roci, T. Wyss, J. Langer, S. Durot, O. Munoz, B. Prat-Luri, M. Delorenzi, M.P. Lutolf, N. Zamboni, G. Verdeil, and T. V. Petrova. 2022. c-MAF coordinates enterocyte zonation and nutrient uptake transcriptional programs. *Journal of Experimental Medicine*. 219. doi:10.1084/jem.20212418.

González-Loyola, A., E. Bovay, J. Kim, T.W. Lozano, A. Sabine, F. Renevey, S. Arroz-Madeira, A. Rapin, T.P. Wypych, G. Rota, S. Durot, D. Velin, B. Marsland, G. Guarda, M. Delorenzi, N. Zamboni, S.A. Luther, and T. V. Petrova. 2021. FOXC2 controls adult lymphatic endothelial specialization, function, and gut lymphatic barrier preventing multiorgan failure. *Sci. Adv.* 7. doi:10.1126/sciadv.abf4335.

Gordon, E.J., S. Rao, J.W. Pollard, S.L. Nutt, R.A. Lang, and N.L. Harvey. 2010. Macrophages define dermal lymphatic vessel calibre during development by regulating lymphatic endothelial cell proliferation. *Development*. 137:3899–3910. doi:10.1242/dev.050021.

Goto, N., S. Goto, S. Imada, S. Hosseini, V. Deshpande, and Ö.H. Yilmaz. 2022. Lymphatics and fibroblasts support intestinal stem cells in homeostasis and injury. *Cell Stem Cell*. 29:1246-1261.e6. doi:10.1016/j.stem.2022.06.013.

Gu, Z., R. Eils, and M. Schlesner. 2016. Complex heatmaps reveal patterns and correlations in multidimensional genomic data. *Bioinformatics*. 32:2847–2849. doi:10.1093/bioinformatics/btw313.

Hallbäck, D.A., M. Jodal, M. Mannischeff, and O. Lundgren. 1991. Tissue osmolality in intestinal villi of four mammals in vivo and in vitro. *Acta Physiol. Scand.* 143:271–277. doi:10.1111/j.1748-1716.1991.tb09232.x.

Hao, Y., S. Hao, E. Andersen-Nissen, W.M. Mauck, S. Zheng, A. Butler, M.J. Lee, A.J. Wilk, C. Darby, M. Zager, P. Hoffman, M. Stoeckius, E. Papalexi, E.P. Mimitou, J. Jain, A. Srivastava, T. Stuart, L.M. Fleming, B. Yeung, A.J. Rogers, J.M. McElrath, C.A. Blish, R. Gottardo, P. Smibert, and R. Satija. 2021. Integrated analysis of multimodal single-cell data. *Cell*. 184:3573-3587.e29. doi:10.1016/j.cell.2021.04.048.

Hasegawa, M., T. Osaka, K. Tawaratsumida, T. Yamazaki, H. Tada, G.Y. Chen, S. Tsuneda, G. Núñez, and N. Inohara. 2010. Transitions in Oral and Intestinal Microflora Composition and Innate Immune Receptor-Dependent Stimulation during Mouse Development. *Infect. Immun.* 78:639–650. doi:10.1128/IAI.01043-09.

Hernández Vásquez, M.N., M.H. Ulvmar, A. González-Loyola, I. Kritikos, Y. Sun, L. He, C. Halin, T. V Petrova, and T. Mäkinen. 2021. Transcription factor FOXP2 is a flow-induced regulator of collecting lymphatic vessels. *EMBO J.* 40. doi:10.15252/embj.2020107192.

Honda, M., B.G.J. Surewaard, M. Watanabe, C.C. Hedrick, W.-Y. Lee, K. Brown, K.D. McCoy, and P. Kubes. 2020. Perivascular localization of macrophages in the intestinal mucosa is regulated by Nr4a1 and the microbiome. *Nat. Commun.* 11:1329. doi:10.1038/s41467-020-15068-4.

Hong, S.P., M.J. Yang, H. Cho, I. Park, H. Bae, K. Choe, S.H. Suh, R.H. Adams, K. Alitalo, D. Lim, and G.Y. Koh. 2020. Distinct fibroblast subsets regulate lacteal integrity through YAP/TAZ-induced VEGF-C in intestinal villi. *Nat. Commun.* 11:4102. doi:10.1038/s41467-020-17886-y.

Jakobsson, L., C.A. Franco, K. Bentley, R.T. Collins, B. Ponsioen, I.M. Aspalter, I. Rosewell, M. Busse, G. Thurston, A. Medvinsky, S. Schulte-Merker, and H. Gerhardt. 2010. Endothelial cells dynamically compete for the tip cell position during angiogenic sprouting. *Nat. Cell Biol.* 12:943–953. doi:10.1038/ncb2103.

Jantsch, J., V. Schatz, D. Friedrich, A. Schröder, C. Kopp, I. Siegert, A. Maronna, D. Wendelborn, P. Linz, K.J. Binger, M. Gebhardt, M. Heinig, P. Neubert, F. Fischer, S. Teufel, J.-P. David, C. Neufert, A. Cavallaro, N. Rakova, C. Küper, F.-X. Beck, W. Neuhofer, D.N. Muller, G. Schuler, M. Uder, C. Bogdan, F.C. Luft, and J. Titze. 2015. Cutaneous Na+ Storage Strengthens the Antimicrobial Barrier Function of the Skin and Boosts Macrophage-Driven Host Defense. *Cell Metab.* 21:493–501. doi:10.1016/j.cmet.2015.02.003.

Jung, S., S. Cheong, Y. Lee, J. Lee, J. Lee, M.-S. Kwon, Y.S. Oh, T. Kim, S. Ha, S.J. Kim, D.H. Jo, J. Ko, and N.L. Jeon. 2024. Integrating Vascular Phenotypic and Proteomic Analysis in an Open Microfluidic Platform. *ACS Nano*. 18:24909–24928. doi:10.1021/acsnano.4c05537.

Kalucka, J., L.P.M.H. de Rooij, J. Goveia, K. Rohlenova, S.J. Dumas, E. Meta, N. V. Conchinha, F. Taverna, L.-A. Teuwen, K. Veys, M. García-Caballero, S. Khan, V. Geldhof, L. Sokol, R. Chen, L. Treps, M. Borri, P. de Zeeuw, C. Dubois, T.K. Karakach, K.D. Falkenberg, M. Parys, X. Yin, S. Vinckier, Y. Du, R.A. Fenton, L. Schoonjans, M. Dewerchin, G. Eelen, B. Thienpont, L. Lin, L. Bolund, X. Li, Y. Luo, and P. Carmeliet. 2020. Single-Cell Transcriptome Atlas of Murine Endothelial Cells. *Cell*. 180:764-779.e20. doi:10.1016/j.cell.2020.01.015.

Karlsen, T. V., M.J. Karkkainen, K. Alitalo, and H. Wiig. 2006. Transcapillary fluid balance consequences of missing initial lymphatics studied in a mouse model of primary lymphoedema. *J. Physiol.* 574:583–596. doi:10.1113/jphysiol.2006.108308.

Karlsson, T., A. Bolshakova, M.A.O. Magalhães, V.M. Loitto, and K.-E. Magnusson. 2013. Fluxes of Water through Aquaporin 9 Weaken Membrane-Cytoskeleton Anchorage and Promote Formation of Membrane Protrusions. *PLoS One*. 8:e59901. doi:10.1371/journal.pone.0059901.

Kataru, R.P., K. Jung, C. Jang, H. Yang, R.A. Schwendener, J.E. Baik, S.H. Han, K. Alitalo, and G.Y. Koh. 2009. Critical role of CD11b+ macrophages and VEGF in inflammatory lymphangiogenesis, antigen clearance, and inflammation resolution. *Blood*. 113:5650–5659. doi:10.1182/blood-2008-09-176776.

Kim, K.E., H. Sung, and G.Y. Koh. 2007. Lymphatic development in mouse small intestine. *Developmental Dynamics*. 236:2020–2025. doi:10.1002/dvdy.21200.

Knight, C.H., E. Maltz, and A.H. Docherty. 1986. Milk yield and composition in mice: Effects of litter size and lactation number. *Comp. Biochem. Physiol. A Physiol.* 84:127–133. doi:10.1016/0300-9629(86)90054-X.

Kondrychyn, I., L. He, H. Wint, C. Betsholtz, and L.-K. Phng. 2025. Combined forces of hydrostatic pressure and actin polymerization drive endothelial tip cell migration and sprouting angiogenesis. *Elife*. 13. doi:10.7554/eLife.98612.

Korff, T., and H.G. Augustin. 1999. Tensional forces in fibrillar extracellular matrices control directional capillary sprouting. *J. Cell Sci.* 112:3249–3258. doi:10.1242/jcs.112.19.3249.

Lee, E., S.-L. Chan, Y. Lee, W.J. Polacheck, S. Kwak, A. Wen, D.-H.T. Nguyen, M.L. Kutys, S. Alimperti, A.M. Kolarzyk, T.J. Kwak, J. Eyckmans, D.R. Bielenberg, H. Chen, and C.S. Chen. 2023. A 3D biomimetic model of lymphatics reveals cell–cell junction tightening and lymphedema via a cytokine-induced ROCK2/JAM-A complex. *Proceedings of the National Academy of Sciences*. 120. doi:10.1073/pnas.2308941120.

Louie, D.A.P., and S. Liao. 2019. Lymph Node Subcapsular Sinus Macrophages as the Frontline of Lymphatic Immune Defense. *Front. Immunol.* 10. doi:10.3389/fimmu.2019.00347.

Love, M.I., W. Huber, and S. Anders. 2014. Moderated estimation of fold change and dispersion for RNA-seq data with DESeq2. *Genome Biol.* 15:550. doi:10.1186/s13059-014-0550-8.

Luks, V.L., N. Kamitaki, M.P. Vivero, W. Uller, R. Rab, J.V.M.G. Bovée, K.L. Rialon, C.J. Guevara, A.I. Alomari, A.K. Greene, S.J. Fishman, H.P.W. Kozakewich, R.A. Maclellan, J.B. Mulliken, R. Rahbar, S.A. Spencer, C.C. Trenor, J. Upton, D. Zurakowski, J.A. Perkins, A. Kirsh, J.T. Bennett, W.B. Dobyns, K.C. Kurek, M.L. Warman, S.A. McCarroll, and R. Murillo. 2015. Lymphatic and Other Vascular Malformative/Overgrowth Disorders Are Caused by Somatic Mutations in PIK3CA. *J. Pediatr.* 166:1048-1054.e5. doi:10.1016/j.jpeds.2014.12.069.

Ma, T., H. Gao, X. Fang, and H. Yang. 2011. Expression and function of aquaporins in peripheral nervous system. *Acta Pharmacol. Sin.* 32:711–715. doi:10.1038/aps.2011.63.

Ma, T., S. Jayaraman, K.S. Wang, Y. Song, B. Yang, J. Li, J.A. Bastidas, and A.S. Verkman. 2001. Defective dietary fat processing in transgenic mice lacking aquaporin-1 water channels. *American Journal of Physiology-Cell Physiology*. 280:C126–C134. doi:10.1152/ajpcell.2001.280.1.C126.

Mäkinen, T., T. Veikkola, S. Mustjoki, T. Karpanen, B. Catimel, E.C. Nice, L. Wise, A. Mercer, H. Kowalski, D. Kerjaschki, S.A. Stacker, M.G. Achen, and K. Alitalo. 2001. Isolated lymphatic endothelial cells transduce

growth, survival and migratory signals via the VEGF-C/D receptor VEGFR-3. *EMBO J.* 20:4762–73. doi:10.1093/emboj/20.17.4762.

Martinez-Corral, I., L. Stanczuk, M. Frye, M.H. Ulvmar, R. Diéguez-Hurtado, D. Olmeda, T. Makinen, and S. Ortega. 2016. Vegfr3-CreER T2 mouse, a new genetic tool for targeting the lymphatic system. *Angiogenesis*. 19:433–445. doi:10.1007/s10456-016-9505-x.

Martinez-Corral, I., Y. Zhang, M. Petkova, H. Ortsäter, S. Sjöberg, S.D. Castillo, P. Brouillard, L. Libbrecht, D. Saur, M. Graupera, K. Alitalo, L. Boon, M. Vikkula, and T. Mäkinen. 2020. Blockade of VEGF-C signaling inhibits lymphatic malformations driven by oncogenic PIK3CA mutation. *Nat. Commun.* 11:2869. doi:10.1038/s41467-020-16496-y.

Nelson, W.J., and R. Nusse. 2004. Convergence of Wnt, beta-Catenin, and Cadherin Pathways. *Science (1979).* 303:1483–1487. doi:10.1126/science.1094291.

Niec, R.E., T. Chu, M. Schernthanner, S. Gur-Cohen, L. Hidalgo, H.A. Pasolli, K.A. Luckett, Z. Wang, S.R. Bhalla, F. Cambuli, R.P. Kataru, K. Ganesh, B.J. Mehrara, D. Pe'er, and E. Fuchs. 2022. Lymphatics act as a signaling hub to regulate intestinal stem cell activity. *Cell Stem Cell*. 29:1067-1082.e18. doi:10.1016/j.stem.2022.05.007.

Nielsen, S., B.L. Smith, E.I. Christensen, and P. Agre. 1993. Distribution of the aquaporin CHIP in secretory and resorptive epithelia and capillary endothelia. *Proceedings of the National Academy of Sciences*. 90:7275–7279. doi:10.1073/pnas.90.15.7275.

Norden, P.R., A. Sabine, Y. Wang, C.S. Demir, T. Liu, T. V Petrova, and T. Kume. 2020. Shear stimulation of FOXC1 and FOXC2 differentially regulates cytoskeletal activity during lymphatic valve maturation. *Elife*. 9. doi:10.7554/eLife.53814.

Norrmén, C., W. Vandevelde, A. Ny, P. Saharinen, M. Gentile, G. Haraldsen, P. Puolakkainen, E. Lukanidin, M. Dewerchin, K. Alitalo, and T. V. Petrova. 2010. Liprin β1 is highly expressed in lymphatic vasculature and is important for lymphatic vessel integrity. *Blood*. 115:906–909. doi:10.1182/blood-2009-03-212274.

Nurmi, H., P. Saharinen, G. Zarkada, W. Zheng, M.R. Robciuc, and K. Alitalo. 2015. VEGF-C is required for intestinal lymphatic vessel maintenance and lipid absorption. *EMBO Mol. Med.* 7:1418–1425. doi:10.15252/emmm.201505731.

Oliver, G., J. Kipnis, G.J. Randolph, and N.L. Harvey. 2020. The Lymphatic Vasculature in the 21st Century: Novel Functional Roles in Homeostasis and Disease. *Cell*. 182:270–296. doi:10.1016/j.cell.2020.06.039.

Salikuqi, B., J. Rispal, E.A. Reyes, D. Vaka, D. Boffelli, and O. Klein. 2022. Lymphangiocrine signals are required for proper intestinal repair after cytotoxic injury. *Cell Stem Cell*. 29:1262-1272.e5. doi:10.1016/j.stem.2022.07.007.

Papadopoulos, M.C., S. Saadoun, and A.S. Verkman. 2008. Aquaporins and cell migration. *Pflugers Arch.* 456:693–700. doi:10.1007/s00424-007-0357-5.

Petkova, M., I. Ferby, and T. Mäkinen. 2024. Lymphatic malformations: mechanistic insights and evolving therapeutic frontiers. *Journal of Clinical Investigation*. 134. doi:10.1172/JCI172844.

1335 Petkova, M., M. Kraft, S. Stritt, I. Martinez-Corral, H. Ortsäter, M. Vanlandewijck, B. Jakic, E. Baselga, S.D. Castillo,
1336 M. Graupera, C. Betsholtz, and T. Mäkinen. 2023. Immune-interacting lymphatic endothelial subtype at
1337 capillary terminals drives lymphatic malformation. *Journal of Experimental Medicine*. 220.
1338 doi:10.1084/jem.20220741.

1339 Petrova, T. V, T. Karpanen, C. Norrmén, R. Mellor, T. Tamakoshi, D. Finegold, R. Ferrell, D. Kerjaschki, P.
1340 Mortimer, S. Ylä-Herttuala, N. Miura, and K. Alitalo. 2004. Defective valves and abnormal mural cell
1341 recruitment underlie lymphatic vascular failure in lymphedema distichiasis. *Nat. Med.* 10:974–981.
1342 doi:10.1038/nm1094.

1343 Petrova, T. V., and G.Y. Koh. 2018. Organ-specific lymphatic vasculature: From development to pathophysiology.
1344 *Journal of Experimental Medicine*. 215:35–49. doi:10.1084/jem.20171868.

1345 Platanitis, E., D. Demiroz, A. Schneller, K. Fischer, C. Capelle, M. Hartl, T. Gossenreiter, M. Müller, M.
1346 Novatchkova, and T. Decker. 2019. A molecular switch from STAT2-IRF9 to ISGF3 underlies interferon-
1347 induced gene transcription. *Nat. Commun.* 10:2921. doi:10.1038/s41467-019-10970-y.

1348 Rytowski, B., J. Goldman, K. Persaud, Y. Wu, L. Witte, D.J. Hicklin, M. Skobe, K.C. Boardman, and M.A. Swartz.
1349 2005. Complete and Specific Inhibition of Adult Lymphatic Regeneration by a Novel VEGFR-3 Neutralizing
1350 Antibody. *JNCI Journal of the National Cancer Institute*. 97:14–21. doi:10.1093/jnci/dji003.

1351 Rockson, S.G., V. Keeley, S. Kilbreath, A. Szuba, and A. Towers. 2019. Cancer-associated secondary lymphoedema.
1352 *Nat. Rev. Dis. Primers*. 5:22. doi:10.1038/s41572-019-0072-5.

1353 Saadoun, S., M.C. Papadopoulos, M. Hara-Chikuma, and A.S. Verkman. 2005. Impairment of angiogenesis and cell
1354 migration by targeted aquaporin-1 gene disruption. *Nature*. 434:786–792. doi:10.1038/nature03460.

1355 Sabine, A., E. Bovay, C.S. Demir, W. Kimura, M. Jaquet, Y. Agalarov, N. Zangger, J.P. Scallan, W. Graber, E.
1356 Gulpinar, B.R. Kwak, T. Mäkinen, I. Martinez-Corral, S. Ortega, M. Delorenzi, F. Kiefer, M.J. Davis, V.
1357 Djonov, N. Miura, and T. V. Petrova. 2015. FOXC2 and fluid shear stress stabilize postnatal lymphatic
1358 vasculature. *Journal of Clinical Investigation*. 125:3861–3877. doi:10.1172/JCI80454.

1359 Sala-Rabanal, M., Z. Yurtsever, K.N. Berry, and T.J. Brett. 2015. Novel Roles for Chloride Channels, Exchangers,
1360 and Regulators in Chronic Inflammatory Airway Diseases. *Mediators Inflamm.* 2015. doi:10.1155/2015/497387.

1361 Salmi, M., M. Karikoski, K. Elima, P. Rantakari, and S. Jalkanen. 2013. CD44 Binds to Macrophage Mannose
1362 Receptor on Lymphatic Endothelium and Supports Lymphocyte Migration via Afferent Lymphatics. *Circ. Res.*
1363 112:1577–1582. doi:10.1161/CIRCRESAHA.111.300476.

1364 Scarchilli, L., A. Camaioni, B. Bottazzi, V. Negri, A. Doni, L. Deban, A. Bastone, G. Salvatori, A. Mantovani, G.
1365 Siracusa, and A. Salustri. 2007. PTX3 Interacts with Inter-α-trypsin Inhibitor. *Journal of Biological Chemistry*.
1366 282:30161–30170. doi:10.1074/jbc.M703738200.

1367 Schulte-Merker, S., A. Sabine, and T. V. Petrova. 2011. Lymphatic vascular morphogenesis in development,
1368 physiology, and disease. *Journal of Cell Biology*. 193:607–618. doi:10.1083/jcb.201012094.

Gibler, E., Y. He, L. Ducoli, N. Keller, N. Fujimoto, L.C. Dieterich, and M. Detmar. 2021. Single-Cell Transcriptional Heterogeneity of Lymphatic Endothelial Cells in Normal and Inflamed Murine Lymph Nodes. *Cells*. 10:1371. doi:10.3390/cells10061371.

Singhal, R., and Y.M. Shah. 2020. Oxygen battle in the gut: Hypoxia and hypoxia-inducible factors in metabolic and inflammatory responses in the intestine. *Journal of Biological Chemistry*. 295:10493–10505. doi:10.1074/jbc.REV120.011188.

Sloas, D.C., S.A. Stewart, R.S. Sweat, T.M. Doggett, N.G. Alves, J.W. Breslin, D.P. Gaver, and W.L. Murfee. 2016. Estimation of the Pressure Drop Required for Lymph Flow through Initial Lymphatic Networks. *Lymphat. Res. Biol.* 14:62–69. doi:10.1089/lrb.2015.0039.

Srinivas, S., T. Watanabe, C.-S. Lin, C.M. William, Y. Tanabe, T.M. Jessell, and F. Costantini. 2001. Cre reporter strains produced by targeted insertion of EYFP and ECFP into the ROSA26 locus. *BMC Dev. Biol.* 1:4. doi:10.1186/1471-213X-1-4.

Srinivasan, R.S., X. Geng, Y. Yang, Y. Wang, S. Mukatira, M. Studer, M.P.R. Porto, O. Lagutin, and G. Oliver. 2010. The nuclear hormone receptor Coup-TFII is required for the initiation and early maintenance of Prox1 expression in lymphatic endothelial cells. *Genes Dev.* 24:696–707. doi:10.1101/gad.1859310.

Stuart, T., A. Butler, P. Hoffman, C. Hafemeister, E. Papalexi, W.M. Mauck, Y. Hao, M. Stoeckius, P. Smibert, and R. Satija. 2019. Comprehensive Integration of Single-Cell Data. *Cell*. 177:1888-1902.e21. doi:10.1016/j.cell.2019.05.031.

Suh, S.H., K. Choe, S.P. Hong, S. Jeong, T. Mäkinen, K.S. Kim, K. Alitalo, C.D. Surh, G.Y. Koh, and J. Song. 2019. Gut microbiota regulates lacteal integrity by inducing VEGF-C in intestinal villus macrophages. *EMBO Rep.* 20. doi:10.15252/embr.201846927.

Tacconi, C., Y. He, L. Ducoli, and M. Detmar. 2021. Epigenetic regulation of the lineage specificity of primary human dermal lymphatic and blood vascular endothelial cells. *Angiogenesis*. 24:67–82. doi:10.1007/s10456-020-09743-9.

Takeda, A., M. Hollmén, D. Dermadi, J. Pan, K.F. Brulois, R. Kaukonen, T. Lönnberg, P. Boström, I. Koskivuo, H. Irjala, M. Miyasaka, M. Salmi, E.C. Butcher, and S. Jalkanen. 2019. Single-Cell Survey of Human Lymphatics Unveils Marked Endothelial Cell Heterogeneity and Mechanisms of Homing for Neutrophils. *Immunity*. 51:561-572.e5. doi:10.1016/j.immuni.2019.06.027.

Tammela, T., G. Zarkada, E. Wallgard, A. Murtomäki, S. Suchting, M. Wirzenius, M. Waltari, M. Hellström, T. Schomber, R. Peltonen, C. Freitas, A. Duarte, H. Isoniemi, P. Laakkonen, G. Christofori, S. Ylä-Herttuala, M. Shibuya, B. Pytowski, A. Eichmann, C. Betsholtz, and K. Alitalo. 2008. Blocking VEGFR-3 suppresses angiogenic sprouting and vascular network formation. *Nature*. 454:656–660. doi:10.1038/nature07083.

The Gene Ontology Consortium. 2019. The Gene Ontology Resource: 20 years and still GOing strong. *Nucleic Acids Res.* 47:D330–D338. doi:10.1093/nar/gky1055.

Thiagarajah, J.R., and A.S. Verkman. 2002. Aquaporin Deletion in Mice Reduces Corneal Water Permeability and Delays Restoration of Transparency after Swelling. *Journal of Biological Chemistry*. 277:19139–19144. doi:10.1074/jbc.M202071200.

Tirosh, I., B. Izar, S.M. Prakadan, M.H. Wadsworth, D. Treacy, J.J. Trombetta, A. Rotem, C. Rodman, C. Lian, G. Murphy, M. Fallahi-Sichani, K. Dutton-Regester, J.-R. Lin, O. Cohen, P. Shah, D. Lu, A.S. Genshaft, T.K. Hughes, C.G.K. Ziegler, S.W. Kazer, A. Gaillard, K.E. Kolb, A.-C. Villani, C.M. Johannessen, A.Y. Andreev, E.M. Van Allen, M. Bertagnolli, P.K. Sorger, R.J. Sullivan, K.T. Flaherty, D.T. Frederick, J. Jané-Valbuena, C.H. Yoon, O. Rozenblatt-Rosen, A.K. Shalek, A. Regev, and L.A. Garraway. 2016. Dissecting the multicellular ecosystem of metastatic melanoma by single-cell RNA-seq. *Science (1979).* 352:189–196. doi:10.1126/science.aad0501.

Trimm, E., and K. Red-Horse. 2023. Vascular endothelial cell development and diversity. *Nat. Rev. Cardiol.* 20:197–210. doi:10.1038/s41569-022-00770-1.

Ulvmar, M.H., and T. Mäkinen. 2016. Heterogeneity in the lymphatic vascular system and its origin. *Cardiovasc. Res.* 111:310–321. doi:10.1093/cvr/cvw175.

Unthank, J.L., and H.G. Bohlen. 1988. Lymphatic pathways and role of valves in lymph propulsion from small intestine. *American Journal of Physiology-Gastrointestinal and Liver Physiology*. 254:G389–G398. doi:10.1152/ajpgi.1988.254.3.G389.

Wiggins, B.G., Y.-F. Wang, A. Burke, N. Grunberg, J.M. Vlachaki Walker, M. Dore, C. Chahrour, B.R. Pennycook, J. Sanchez-Garrido, S. Vernia, A.R. Barr, G. Frankel, G.M. Birdsey, A.M. Randi, and C. Schiering. 2023. Endothelial sensing of AHR ligands regulates intestinal homeostasis. *Nature*. 621:821–829. doi:10.1038/s41586-023-06508-4.

Xiang, M., R.A. Grosso, A. Takeda, J. Pan, T. Bekkhus, K. Brulois, D. Dermadi, S. Nordling, M. Vanlandewijck, S. Jalkanen, M.H. Ulvmar, and E.C. Butcher. 2020. A Single-Cell Transcriptional Roadmap of the Mouse and Human Lymph Node Lymphatic Vasculature. *Front. Cardiovasc. Med.* 7. doi:10.3389/fcvm.2020.00052.

Yu, G., L.-G. Wang, Y. Han, and Q.-Y. He. 2012. clusterProfiler: an R Package for Comparing Biological Themes Among Gene Clusters. *OMICS.* 16:284–287. doi:10.1089/omi.2011.0118.

Zampell, J.C., A. Yan, S. Elhadad, T. Avraham, E. Weitman, and B.J. Mehrara. 2012. CD4+ Cells Regulate Fibrosis and Lymphangiogenesis in Response to Lymphatic Fluid Stasis. *PLoS One*. 7:e49940. doi:10.1371/journal.pone.0049940.

Zarkada, G., X. Chen, X. Zhou, M. Lange, L. Zeng, W. Lv, X. Zhang, Y. Li, W. Zhou, K. Liu, D. Chen, N. Ricard, J. Liao, Y.-B. Kim, R. Benedito, L. Claesson-Welsh, K. Alitalo, M. Simons, R. Ju, X. Li, A. Eichmann, and F. Zhang. 2023. Chylomicrons Regulate Lacteal Permeability and Intestinal Lipid Absorption. *Circ. Res.* 133:333–349. doi:10.1161/CIRCRESAHA.123.322607.

Zhang, W., M. Freichel, F. van der Hoeven, P.P. Nawroth, H. Katus, F. Kälble, E. Zitron, and V. Schwenger. 2016. Novel Endothelial Cell-Specific AQP1 Knockout Mice Confirm the Crucial Role of Endothelial AQP1 in Ultrafiltration during Peritoneal Dialysis. *PLoS One*. 11:e0145513. doi:10.1371/journal.pone.0145513.

Zheng, W., T. Tammela, M. Yamamoto, A. Anisimov, T. Holopainen, S. Kaijalainen, T. Karpanen, K. Lehti, S. Ylä-Herttuala, and K. Alitalo. 2011. Notch restricts lymphatic vessel sprouting induced by vascular endothelial growth factor. *Blood*. 118:1154–1162. doi:10.1182/blood-2010-11-317800.

Figure legends

Figure 1

Characterization of intestinal LEC heterogeneity through integrated scRNA-seq analysis. A. Scheme illustrating the integration of scRNA-seq data from intestinal LECs from this study (samples 1-5) and three published studies (samples 6-8). LECs were defined as *Pecam1*$^{+}$, *Flt1*$^{-}$, *Prox1*$^{+}$, and *Flt4*$^{+}$ cells. Cells with similar transcriptional profiles were aligned and grouped to minimize batch effects, followed by unsupervised clustering, differential gene expression and GO enrichment. **B.** UMAP showing integrated cells, colored by cluster assignment at resolution 0.3. **C.** Dot plot displaying the top variably expressed genes per cluster. Dot size indicates the percentage of cells expressing the gene within each cluster; color reflects scaled average expression levels. **D.** AQP1 is expressed in lacteal LECs. Whole-mount immunofluorescence staining of small intestine for CD31 (green), LYVE1 (magenta), and AQP1 (cyan) in the merged image. Separate grayscale images show LYVE1 or AQP1 staining alone. **E.** FABP4 is expressed in lacteal LECs. Whole-mount immunofluorescence staining for LYVE1 (cyan), and FABP4 (red). Separate grayscale images show LYVE1 or FABP4 staining alone; the red dotted line in the zoomed inset outlines the lacteal. **F.** CLCA3A1 is mostly expressed in serosal LECs. Immunohistochemical staining of paraffin-embedded small intestine sections for CLCA3A1 (cyan), VEGFR3 (magenta) and DAPI (yellow). Separate grayscale image shows CLCA3A1 staining alone. **G.** The anatomical localization of the LEC clusters in small intestine, showing lacteal LECs (cluster 0), submucosal, muscular and serosal (S/S) LECs (cluster 1). **H.** Comparison of intestinal LEC clusters with LECs from other tissues. Heatmaps show the signature comparisons of three intestinal LEC clusters with LEC clusters from skin (Petkova et al., 2023), lymph node (Xiang et al., 2020), and mesentery (González-Loyola et al., 2021), respectively. Colors represent similarity scores (scaled median module scores). Scale bars: 25 μm.

Figure 2

AQP1 is essential for lacteal function. A. AQP1 is enriched at the lacteal tip. Image of a lacteal marking the tip and base. Paired AQP1 fluorescence intensity quantification at the tip and base of the same lacteal. n=5 mice, 10 lacteals per mouse; paired t-test. **B.** Generation of LEC-specific *Aqp1* knockout mice. Top: Schematic of the genetic model for conditional *Aqp1* deletion in LECs (*Aqp1*$^{i\Delta LEC}$), with loxP sites flanking exons 2 and 3 of *Aqp1* and CreERT2 expression under the *Prox1* promoter. Bottom: Timeline of tamoxifen injections over four weeks to induce deletion. **C.** Validation of AQP1 deletion in intestinal LECs. Staining for AQP1 (cyan) and LYVE1 (red) shows representative base-to-tip lacteals in *Aqp1*$^{fl/fl}$ and *Aqp1*$^{i\Delta LEC}$ mice. Grayscale images show individual staining. **D.** Lymphatic *Aqp1* deletion leads to lacteal shortening. Schematic illustrates measurement of lacteal length relative

to blood vessels. Violin plots show the distribution of relative lacteal length intervals as percentages of villus length in *Aqp1*$^{fl/fl}$ and *Aqp1*$^{i\Delta LEC}$ mice. n=10 mice, mixed sex; two-way repeated-measures ANOVA, followed by pairwise t-tests with Benjamini-Hochberg correction. **E.** Lymphatic *Aqp1* deletion blunts dietary lipid absorption. Timeline for olive oil gavage and blood sampling at indicated intervals. Line graph shows serum triglyceride (TG) levels over time. n=11 mice; two-way repeated-measures ANOVA, followed by two-sample t-tests with Holm–Sidak corrections for multiple comparisons. **F.** Plasma TG levels in control (*Aqp1*$^{fl/fl}$, n=4) and *Aqp1*$^{i\Delta LEC}$ mice (n=3) following oral gavage with olive oil in the presence of the lipoprotein lipase inhibitor Tyloxapol. Two-way ANOVA followed by two-sample t-tests with Holm-Sidak correction. **G.** Lymphatic *Aqp1* deletion prevents weight gain on HFD. Timeline for tamoxifen injections and HFD administration. Dot plot shows percentage weight gain from baseline (week two) after three weeks on HFD. control: *Aqp1*$^{fl/fl}$, n=6 mice and *Aqp1*$^{i\Delta LEC}$, n=4 mice; HFD: *Aqp1*$^{fl/fl}$ n=4 mice and *Aqp1*$^{i\Delta LEC}$ n=5 mice; Welsh's t-test for each diet. Data are shown as mean ±SD. Scale bars: 25 μm.

Figure 3

Postnatal AQP1 expression in lacteal LECs is induced by microbiota and VEGFR3 signaling. A. AQP1 expression emerges postnatally in lacteals. Staining for AQP1 (magenta) and LYVE1 (green) in lacteals from postnatal days P1-P5. Grayscale images show AQP1 alone. **B.** Quantification of AQP1 distribution along the lacteal. One mouse per timepoint: P1 (n = 53 lacteals), P2 (n = 51 lacteals), P3 (n = 55 lacteals), P4 (n = 5 lacteals), P5 (n = 68 lacteals). Scale bar: 20 μm. **C.** Microbiota depletion reduces AQP1 in lacteals. Immunofluorescence images of lacteals from control and antibiotic-treated mice stained for AQP1 (magenta) and LYVE1 (cyan). **D.** Quantification of AQP1 intensity per lacteal. control: n=5 mice, antibiotic: n=4 mice; Student's t-test. Scale bar: 25 μm. **E.** VEGFR3 blockade lowers AQP1 expression. Timeline for administration of VEGFR3-blocking (mF4-31C1) or control IgG2a antibody. Staining for AQP1 (magenta) and VEGFR3 (cyan). Scale bar: 20 μm. **F.** Quantification of AQP1 intensity per lacteal. n=3 mice; Student's t-test. Data are shown as mean ±SD.

Figure 4

AQP1 enables LEC migration in hyperosmotic microenvironments. A. Lentiviral constructs used to transduce human LECs. **B.** Validation of AQP1 overexpression *in vitro*. Western blot analysis of control and *AQP1*^{OE} LEC lysates for the indicated proteins. Representative of n=2 independent experiments. Blots in this panel and Fig. 5D are from the same membrane; the histone H3 panel is the same in both. **C.** AQP1 localization in transduced LECs. Staining for VE-Cadherin (green) and AQP1 (magenta). The yellow insets show magnified regions, with AQP1 shown in grayscale. Scale bars:

25 µm. **D.** Schematic of the spheroid sprouting assay. **E.** AQP1 overexpression promotes lymphatic sprouting under osmotic stress. Representative images of F-actin (grey) and DAPI (red) staining. Spheroid core, nucleated sprouts, and anucleated protrusions are indicated. The fuller set is shown in Fig. S4A (inverted grayscale). Scale bar: 50 µm. **F.** Quantification of sprout number per spheroid. **G.** Quantification of total sprout length per spheroid. **F-G.** Mean sprout number under eight conditions combining cell lines (control or *AQP1*^{OE}), VEGF-C (− or +), and medium (control or hyperosmotic). Dot colors indicate individual replicates (plates). n=4 (except AQP1, BSA, hyperosmotic n=3); three-way ANOVA, followed by Tukey's multiple comparisons test. p values from paired comparisons are shown in the plot. Representative significant comparisons are indicated; complete statistical results for all pairwise comparisons are provided in Table S2. **H.** Mosaic deletion of *Aqp1* in lacteals. Left: experimental scheme for mosaic deletion analysis. *Aqp1*$^{i\Delta LEC}$;*Rosa26-EYFP and* control *Rosa26-EYFP* mice received reduced tamoxifen (7.5 µg/g) to achieve mosaic deletion. Analysis performed 3 weeks post-injection. Right: representative whole-mount images of control and *Aqp1*$^{i\Delta LEC}$ mosaic lacteals. Left: LYVE1 (blue), PROX1 (green), YFP (magenta), DAPI (blue). Middle and right: PROX1 and YFP shown separately in grayscale. Dotted lines outline lacteal boundaries. Scale bar: 30 µm. **I.** Decreased proportion of YFP$^+$Prox1$^+$ cells in *Aqp1*$^{i\Delta LEC}$ lacteals. WT: n=3 mice, *Aqp1*$^{i\Delta LEC}$: n=4 mice; Mann-Whitney test. **J.** Decreased proportion of YFP$^+$ cells at lacteal tips. WT: n=3 mice, *Aqp1*$^{i\Delta LEC}$: n=4 mice; Mann-Whitney test. **K.** Spatial distribution of YFP$^+$ LECs along lacteal length. *Aqp1*-deficient cells are enriched at the base (0-20%) and depleted from tip positions (80-100%). WT: n=3 mice, *Aqp1*$^{i\Delta LEC}$: n=4 mice; two-way repeated measures ANOVA followed by pairwise t-tests with Benjamini-Hochberg correction. **L.** Model summarizing *in vitro* and *in vivo* findings. Left: AQP1-expressing LECs migrate further than AQP1-deficient cells under hyperosmotic conditions in the presence of VEGF-C. Right: In lacteals, AQP1$^+$ LECs migrate toward the villus tip along the osmolarity gradient, while AQP1-deficient cells are excluded from high-osmolarity tip positions. Data are shown as mean ±SD.

Figure 5

AQP1 facilitates cytoskeletal and junctional remodeling under osmotic stress. A. Representative images stained for AQP1 (red), F-actin (white) and β-catenin (green) in control (*EBF*^{OE}) and *AQP1*^{OE} LECs under control (300 mOsm) and hyperosmotic (500 mOsm) conditions. Yellow insets indicate regions magnified in panel B. **B.** F-actin distribution analysis. Top: Magnified insets from panel A showing measurement approach from cell periphery (P) through center (C) to periphery (P). Bottom: quantification of F-actin intensity distribution across the cell, in control and *AQP1*^{OE} cells at 300 mOsm and 500 mOsm. n=3 independent experiments with 20 cells per experiment; multiple unpaired t-tests comparing control vs *AQP1*^{OE} 300 mOsm at each position for 300 mOsm and 500 mOsm separately, with FDR correction (Q=5%). Bracket: positions with adjusted p<0.05 at both osmolarities. **C.**

Quantification of relative β-catenin area per cell. n=3 independent experiments; two-way ANOVA with Sidak's multiple comparison test. **D**. Increased β-catenin levels in *AQP1*^{OE} LECs. Western blot analysis and quantification of β-catenin and histone H3 (loading control). n=2 independent experiments. Blots in this panel and Fig. 4B are from the same membrane; the histone H3 panel is the same in both. **E.** AQP1 interacts with β-catenin. Representative images of proximity ligation assay (PLA) in WT, *CTNNB1*^{KD}, *AQP1*^{OE}, and *CTNNB1*^{KD} + *AQP1*^{OE} LECs under control and hyperosmotic conditions. DAPI (blue), PLA signal (red puncta). **F.** Quantification of data shown in E. n=10 cells per condition, representative of 2 independent experiments; one-way ANOVA with Tukey's post-hoc test. Data are mean ± SD. Scale bar: 20 μm.

Figure 6

AQP1 normalizes osmotic stress-induced transcriptional changes. A. Experimental scheme for bulk RNA barcoding and sequencing (BRB-seq). n=2. **B.** Volcano plot showing differential gene expression in control LECs under hyperosmotic stress (Control 500 mOsm vs Control 300 mOsm). Osmotic stress affects 1593 differentially expressed genes (adjusted p-value < 0.05, |log2 fold change| > 0.6). Selected genes are labeled. **C.** Volcano plot showing differential gene expression between *AQP1*^{OE} LECs at 300 mOsm and Control LECs at 300 mOsm (*AQP1*^{OE} 300 vs Control 300). **D.** Heatmap showing scaled expression of 1593 genes that are differentially expressed under osmotic stress and rescued by *AQP1* overexpression. Each row represents an individual gene. Gray and purple bars above columns indicate osmolarity conditions (gray: 300 mOsm; purple: 500 mOsm). Black bars on the right mark genes that are significantly differentially expressed between *AQP1*^{OE} LECs and Control LECs at 500mOsm (adjusted p-value < 0.05). **E.** AQP1 partially normalizes osmotic stress-induced transcriptional response. Of 1593 genes altered by osmotic stress in control cells, 724 genes are rescued in *AQP1*^{OE} LECs under stress (rescued genes), while 738 genes remain differentially expressed. 131 genes show normalization within 25-99% of baseline. **F.** Expression patterns of selected rescued genes across functional categories (Polarity, Adhesion, Migration Signaling, Guidance, ECM, and Cytoskeleton). Column 1: Ctrl: 500 vs 300 mOsm. Column 2: *AQP1*^{OE} 500 vs Ctrl 300 mOsm. Circle size indicates significance (p-adjusted); color indicates $\log_2$ fold change.

Figure 7

AQP1 is induced during inflammatory lymphangiogenesis. A. Number of cells that express varying levels of *Aqp1* levels in dermal LEC subpopulations from control and *Pik3ca*^{H1047R} mice scRNA-seq data re-analysed from (Petkova et al., 2023). Colors indicate *Aqp1* expression quartiles: 0–25%, 25–50%, 50–75%, 75–100%. **B.** AQP1 is induced in hypersprouting dermal lymphatics of *Pik3ca*^{H1047R}

mice. Left: Whole-mount ear staining (control and *Pik3ca*^{H1047R}) for AQP1 (red), VEGFR3 (green), and CD31 (blue). Grayscale images show individual channels. Scale bar: 50 µm. Right: Quantification of mean AQP1 intensity in VEGFR3$^+$ areas (control: n=3 mice; mutant: n=2 mice). **C.** AQP1 expression in medullary sinus LECs. Staining of medullary sinus LECs (control and inflamed LNs) for AQP1 (magenta), LYVE1 (green), PROX1 (cyan) and DAPI (blue). Grayscale images show AQP1 alone and AQP1 within LYVE1 mask. Scale bar: 50 µm. **D.** AQP1 is upregulated in secondary lymphedema (LD) model. Staining of skin from control and LD mice for VEGFR3 (green), AQP1 (magenta), and DAPI (blue). Dashed squares (1: control; 2: LD) indicate insets with separate grayscale images for VEGFR3 and AQP1. Scale bar: 100 µm. The dot plot quantifies the percentage of AQP1$^+$ area within VEGFR3$^+$ vessels (n = 5 mice). **E.** AQP1$^+$ LECs show increased proliferation. Skin sections (control and LD) stained for AQP1 (yellow), Ki67 (magenta) and PROX1 (cyan) or Ki67 (magenta), and PROX1 (cyan). Arrows indicate PROX1$^+$ Ki67$^+$ cells; arrowheads, PROX1$^+$ Ki67$^-$ cells; dashed lines outline lymphatic vessels. Scale bar: 50 µm. Left dot plot shows the percentage of PROX1$^+$ cells that are Ki67$^+$ (n = 4 mice). Right dot plot shows Ki67$^+$ PROX1$^+$ cells in LD tissues. Data are shown as mean ± SD; differences were assessed using Student's t-test.

Figure 8

AQP1 is dispensable for embryonic but required for stress-adaptive lymphangiogenesis. A. AQP1 is not expressed during embryonic lymphangiogenesis. Whole-mount staining E16.5 skin stained for CD31 (magenta), VEGFR3 (yellow), AQP1 (green); grayscale images show individual markers. Scale bar: 100 µm. **B.** AQP1 is absent in embryonic LN LECs. E17.5 LN sections stained for AQP1 (magenta), LYVE1 (green), PROX1 (cyan) and DAPI (blue); grayscale images show AQP1 alone and AQP1 masked by LYVE1 staining. Scale bar: 50 µm. **C.** AQP1 is induced in lymphatic valve sinuses of postnatal *Foxc2*^{lecko} mice. Left panels: immunofluorescence staining for PROX1 (cyan), LYVE1 (yellow), AQP1 (red), and DAPI (blue). Right panels show AQP1 alone (grayscale). Yellow dotted lines outline lymphatic vessels. Scale bar: 25 µm. **D.** AQP1 is not expressed in embryonic lymphatic vessels in the model of lymphedema-distichiasis *Foxc2*^{lecko} mice. E18.5 mesenteric lymphatic vessels from WT and *Foxc2*^{lecko} embryos stained for PROX1 (red), FOXC2 (yellow), AQP1 (cyan), and DAPI (blue). Right: AQP1 staining alone (grayscale). Yellow dotted lines outline lymphatic vessels (LV); green dotted lines outline blood vessels (BV). Scale bar: 25 µm. **E.** Loss of *Aqp1* reduces formation of collaterals in *Aqp1;Foxc2*^{lecko} mice. Staining for PROX1 (purple) and CD31 (white). Yellow dotted lines outline lymphatic vessels; red dotted lines mark sprouts from collecting vessels. **F.** Quantification of valves with sprouts. WT: n=15 mice, *Foxc2*^{lecko}: n=6 mice, *Aqp1;Foxc2*^{lecko}; n=7 mice. Data are mean ± SD. One-way ANOVA with unpaired t-tests.

Figure 9

Model: AQP1 facilitates lymphangiogenic response in hyperosmotic inflammatory environments. **A.** AQP1 expression marks stress-adaptive lymphangiogenesis. Left: VEGF-C/VEGFR3 signaling alone supports lymphatic development or maintenance in embryonic villus, homeostatic dermis and lymph node. Right: AQP1 is induced in adult lacteals, dermal lymphatics in lymphatic malformations, and inflamed lymph node, contexts sharing hyperosmolarity and macrophage infiltration. Medullary sinus *Ptx3*+ LECs represent a constitutively primed niche. VEGF-C is present in all contexts; elevated osmolarity and inflammatory signals define stress-adaptive environments. **B.** AQP1 enables LEC migration under hyperosmotic stress. In the presence of VEGF-C, both AQP1-negative and AQP1-positive LECs migrate under normosmotic conditions. However, under hyperosmotic stress, only AQP1-expressing LECs maintain migratory capacity. **C.** Molecular basis of AQP1 function under hyperosmotic stress. Without AQP1 (top), LECs accumulate cortical F-actin and stabilize adherens junctions, blocking migration despite active VEGFR3 signaling. With AQP1 (bottom), water flux is restored, stress fibers and junctional dynamics are maintained, and AQP1 interacts with β-catenin, allowing migration. Insets show resulting cellular phenotypes. Purple gradient, osmolarity (300–600 mOsm); yellow-green gradient, AQP1 expression. PM, plasma membrane.

Figure S1

Supplementary to Figure 1. A. UMAP of all integrated cells colored by their originating sample (dataset numbers per Fig. 1A; cell numbers in brackets). **B.** AQP1 expression is restricted to villus lacteals with minimal to no expression in serosal lymphatic vessels. Immunofluorescent staining of intestinal tissue. Left: merged image showing VEGFR3 (green), AQP1 (magenta), EMCN (yellow), and DAPI (blue). Middle: AQP1 staining alone. Right: AQP1 signal within VEGFR3 regions (mask). Green dotted lines outline serosal lymphatic vessels (middle and right panels). Scale bar: 50 µm. **C.** UMAP of integrated cells re-clustered after removing IFN-response genes (cluster 2 markers). Colors indicate original clustering (Cl.0-1-2; Fig.1B), with full or empty circles (symbol) distinguishing the re-clustering into Cl.0-1. **D.** Expression of cluster 0 and cluster 1 marker genes after reclustering without IFN-response genes. Dot plot showing expression of selected marker genes in cluster 0 (lacteal) and cluster 1 (S/S) following removal of IFN-response genes and reclustering. Dot size indicates percent of cells expressing each gene; color indicates scaled average expression. **E.** Heatmap of top GO biological processes per cluster, colored by enrichment score. **F.** Dot plot of the top 10 transcription factors with highest variability for regulon activity among clusters. Dot size shows Regulon Specificity Score (RSS), indicating specificity to a cluster; dot color reflects the regulon activity z-score, indicating the level of activity. **G.** Dot plot of the top 10 transcription factors with variable regulon activity. Dot size indicates the percentage of cells expressing each factor; color reflects scaled average expression. **H.** Number of

cells expressing varying levels of *Ptx3* expression levels in intestine LEC clusters. Colors indicate *Ptx3* expression quartiles: 0–25%, 25–50%, 50–75%, 75–100%.

Figure S2

Supplementary to Figure 2. A. AQP1 is expressed in lacteals throughout the intestine. Duodenum, jejunum and ileum stained for AQP1 (green) and CD31 (purple); grayscale images show AQP1 alone. Scale bar: 25 µm. **B.** AQP1 is detected in intestinal but not colon LECs. Paraffin sections of jejunum and color stained for AQP1 (magenta), EMCN (yellow), VEGFR3 (green), DAPI (blue); grayscale images show individual markers for insets. Scale bar: 20 µm. **C.** Flow cytometry gating for LEC isolation from the small intestine. Gating steps include exclusion of debris and doublets, gating of $DAPI^-$ live cells, exclusion of $CD45^+$ and $EpCAM^+$ cells, and finally sorting of $CD31^+PDPN^+$ LECs. **D.** Validation of *Aqp1* deletion. qPCR for *Aqp1* mRNA in $Aqp1^{fl/fl}$ and $Aqp1^{i\Delta LEC}$ mice, normalized to 18S rRNA. **E.** Representative images of LYVE1 (green) and FABP4 (magenta) in WT ($Aqp1^{fl/fl}$) and $Aqp1^{i\Delta LEC}$ mice. Right panels show FABP4 signal within $LYVE1^+$ vessel mask. Scale bar: 20 µm. **F.** Representative images of LYVE1+ (green) and PTX3 (magenta). Right panels show PTX3 signal within $LYVE1^+$ vessel mask + 5 µm. **G.** Quantification of mean FABP4 intensity in lacteals. WT: n=4 mice, $Aqp1^{i\Delta LEC}$: n=3; Welch's t-test. **H.** Quantification of mean PTX3 intensity. WT: n=4 mice, $Aqp1^{i\Delta LEC}$: n=3; Welch's t-test; ns, not significant. Scale bar: 20 µm. **I.** Dot plot showing expression of *Aqp1* and *Ptx3* across lamina propria cell types (ICCs, Villus SMCs, Fibin+, Crypt-, Prrx1+, Telocytes, Villus fibroblasts). Dot size indicates percent expression; color indicates average expression. Data reanalyzed from a published dataset (Bernier-Latmani et al., 2022), (GEO: GSE154821) **J.** Heatmap of gene expression (log2(cpm+1)) for *Epcam*, *Krt20*, *Aqp1*, *Pdgfra*, and *Ptx3* in epithelial cells. Data reanalyzed from a published dataset (González-Loyola et al., 2022), (GEO: GSE189852). Data are mean ± SD.

Figure S3

Supplementary to Figure 3. A. Representative images of $LYVE1^+$ lacteals in control and antibiotic-treated mice. **B.** Quantification of mean lacteal length. n=4 mice. **C.** Representative images of $LYVE1^+$ lacteals (green) and FABP4 (magenta) in control and antibiotic-treated mice. The right panels show the FABP4 signal within $LYVE1^+$ vessel mask. **D.** Quantification of mean FABP4 intensity. **E.** Representative images of $LYVE1^+$ lacteals (green) and PTX3 (magenta). The right panels show PTX3 signal within $LYVE1^+$ vessel mask. **F.** Quantification of mean PTX3 intensity shows trend toward reduction (p=0.086). n=3 mice. Data are mean ± SD. Differences were assessed using Welsh's t-test; ns, not significant. Scale bars: 20 µm.

Figure S4

Supplementary to Figures 4 and 5. A. Representative inverted grayscale images of F-actin in control (*EBFP*^{OE}) and *AQP1*^{OE} LECs, cultured in normosmotic, hyperosmotic, or hypoosmotic medium, with or without VEGF-C. **B.** Quantification of nuclei per 100 µm sprout length across conditions (cell type: Control vs *AQP1*^{OE}; treatment: BSA vs VEGF-C; osmolarity: Control vs Hyperosmotic). **C.** Quantification of protrusion number per spheroid across conditions. Data in B-C: n=4 independent experiments (except AQP1, BSA, hyperosmotic n=3). Three-way ANOVA followed by Tukey's multiple comparisons test. Representative significant comparisons are indicated; complete statistical results for all pairwise comparisons are provided in Table S2. **D.** Representative images of control and *AQP1*^{OE} LEC sprouting in vascular phenotypic and proteomic analysis (VPT) platform under control (300 mOsm) and hyperosmotic (500 mOsm) conditions. **E.** Quantification of relative sprout number, relative sprout length, and relative nuclei per sprout baseline. AQP1 overexpression increases sprout number and length at 500 mOsm. n=3 independent experiments; two-way ANOVA followed by Tukey's multiple comparisons test. **F.** AQP1 expression levels shown relative to RPL27 housekeeping gene expression in control and *AQP1*^{OE} LECs under increasing hydrostatic pressure (0, and 2mmHg). n=3 biological replicates. Two-way ANOVA followed by Sidak's multiple comparisons test. **G.** Representative images of control and *AQP1*^{OE} LECs under hydrostatic pressure showing DAPI (blue) and F-actin (white). **H.** F-actin intensity distribution under hydrostatic pressure (0 and 2 mmHg). Multiple unpaired t-test comparing control vs *AQP1*^{OE} at each position for each pressure condition, with FDR correction (Q=5%). n=3 biological replicates. Symbols: * adj. $p < 0.05$. Data are mean ± SD. Scale bars: 50 µm.

Figure S5

Supplementary to Figures 6-7. A. qPCR validation of LEC transcriptomics. Expression of selected genes (*AQP1*, *SGK1*, *ZFP36L1*, *PKN1*) in control and *AQP1*^{OE} LECs under control (300 mOsm) and hyperosmotic (500 mOsm) conditions relative to 18S. n=2. **B.** Quantification of AQP1 expression in lymph node LECs. Left bar chart: quantification of AQP1+ area within LYVE1+ mask in inguinal and popliteal lymph nodes at postnatal and adult stages (postnatal and adult inguinal n=4, inflamed inguinal and popliteal n=2 mice). Right bar chart: comparison of AQP1+ area in subcapsular sinus (SCS) versus medullary sinus at postnatal and adult stages (n=4 mice; 2 sections per animal for adult groups). Mann-Whitney U test. **C.** AQP1 is absent in subcapsular sinus LECs. Control and inflamed LN sections stained for AQP1 (magenta), LYVE1 (green), PROX1 (cyan), and DAPI (blue); grayscale images show AQP1 alone and AQP1 masked by LYVE1 staining. Scale bar: 50 µm. **D.** Macrophage infiltration increases in lymphedema (LD). Skin sections stained for VEGFR3 (green), CSF1R (magenta, macrophages), CD4 (yellow, T-cells), and DAPI (blue); grayscale images show CSF1R or CD4 alone. Scale bar:

50 µm. The dot plot quantifies the number of $CSF1R^+$ cells per mm^2. **E.** $AQP1^+$ lacteals are surrounded by macrophages. Paraffin sections of jejunum stained for LYVE1 (green), CSF1R (red), and DAPI (blue) (n=5 mice). Scale bar: 20 µm. **F.** AQP1 expression at valve-adjacent regions in lymphedema. Skin section from LD mouse stained for AQP1 (magent a), VEGFR3 (cyan), and DAPI (blue). Dashed box indicates magnified region shown in grayscale insets for VEGFR3 and AQP1. Magenta arrowheads indicate AQP1-high regions adjacent to valve leaflets; mint arrowheads indicate VEGFR3+ AQP1-low regions. Scale bar: 50 µm. **G.** AQP1 is upregulated in blood vessels in LD. Skin sections (control and LD) stained for AQP1 (magenta), VEGFR3 (cyan), and EMCN (green); grayscale images show AQP1 alone (n=5 mice). Scale bar: 50 µm. The dot plot shows the percentage of $AQP1^+$ area within $EMCN^+$ vessels. Data are mean ± SD. Differences were assessed using Student's t-test.

Figure 1

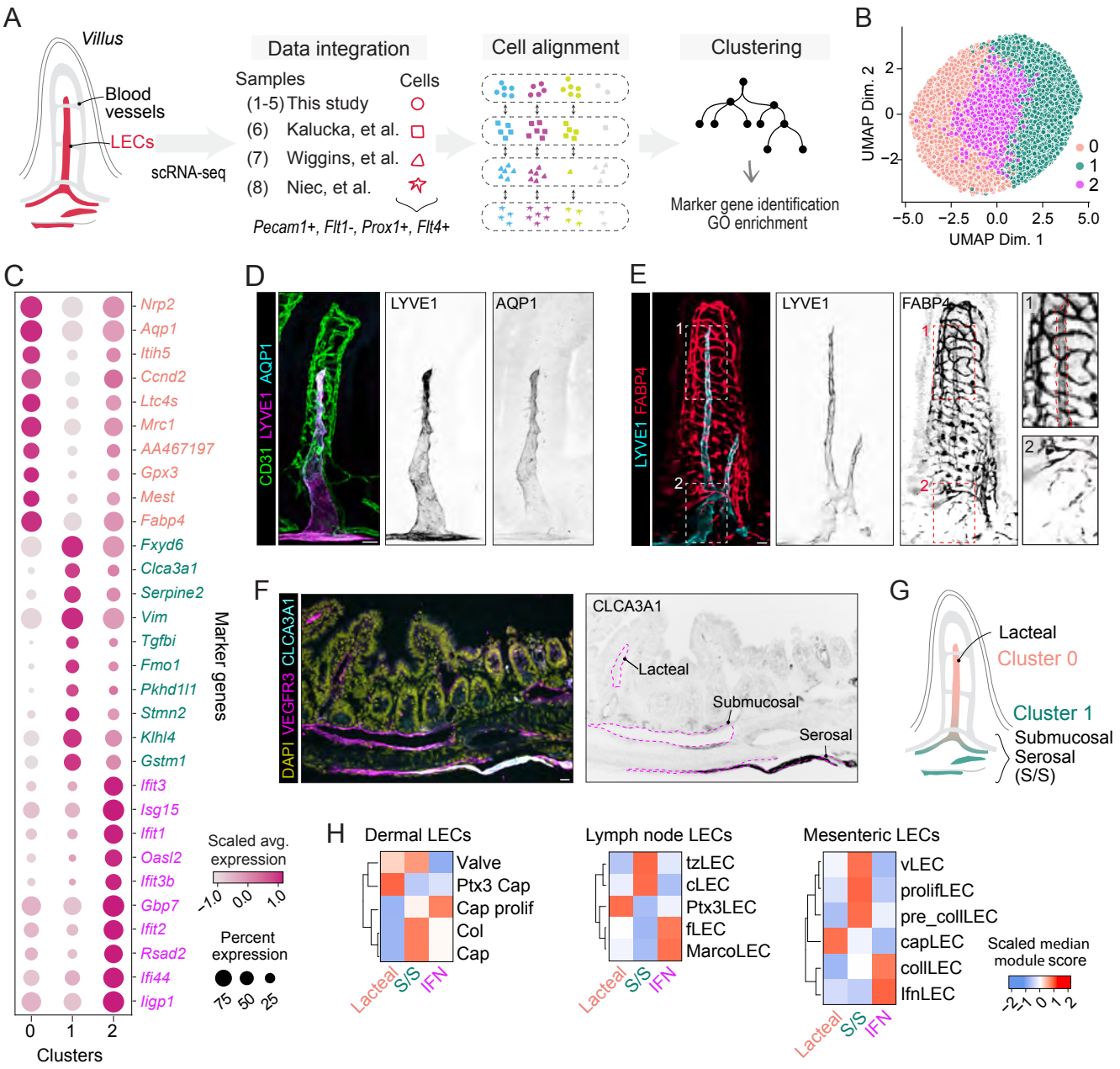
A
Villus
Blood vessels
LECs
scRNA-seq
Data integration
Samples
Cells
(1-5) This study
(6) Kalucka, et al.
(7) Wiggins, et al.
(8) Niec, et al.
Pecam1+, Flt1-, Prox1+, Flt4+
Cell alignment
Clustering
Marker gene identification
GO enrichment
B
UMAP Dim. 2
UMAP Dim. 1
C
Nrp2
Aqp1
Itih5
Ccnd2
Ltc4s
Mrc1
AA467197
Gpx3
Mest
Fabp4
Fxyd6
Clca3a1
Serpine2
Vim
Tgfbi
Fmo1
Pkhd1l1
Stmn2
Klhl4
Gstm1
Ifit3
Isg15
Ifit1
Oasl2
Ifit3b
Gbp7
Ifit2
Rsad2
Ifi44
Iigp1
Marker genes
Scaled avg. expression
Percent expression
Clusters
D
CD31 LYVE1 AQP1
LYVE1
AQP1
E
LYVE1 FABP4
LYVE1
FABP4
F
DAPI VEGFR3 CLCA3A1
CLCA3A1
Lacteal
Submucosal
Serosal
G
Lacteal
Cluster 0
Cluster 1
Submucosal
Serosal
(S/S)
H
Dermal LECs
Valve
Ptx3 Cap
Cap prolif
Col
Cap
Lymph node LECs
tzLEC
cLEC
Ptx3LEC
fLEC
MarcoLEC
Mesenteric LECs
vLEC
prolifLEC
pre_collLEC
capLEC
collLEC
IfnLEC
Lacteal
S/S
IFN
Scaled median module score

Figure 2

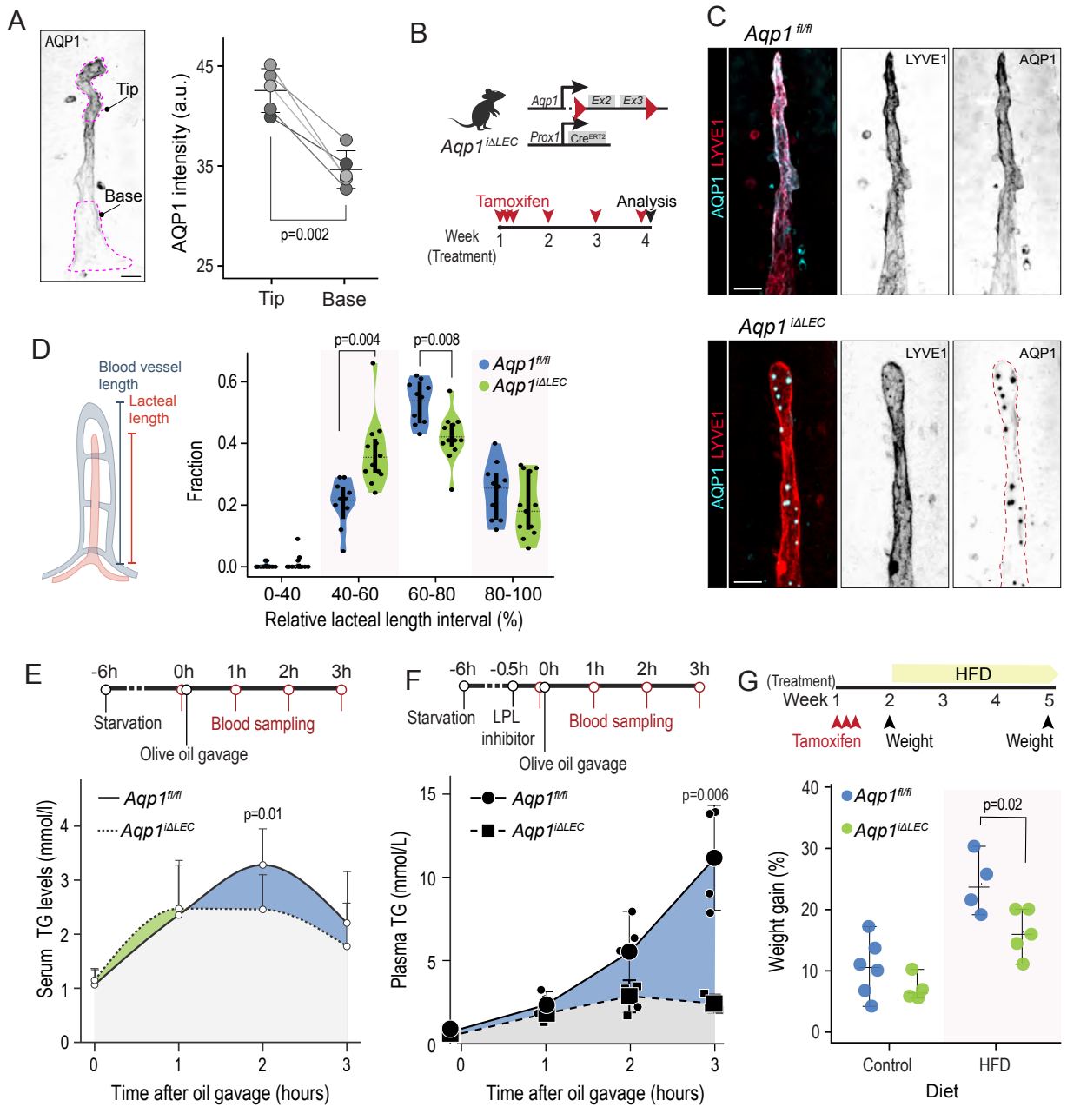
A
AQP1
Tip
Base
AQP1 intensity (a.u.)
45
35
25
p=0.002
Tip
Base
B
Aqp1 iΔLEC
Aqp1
Ex2
Ex3
Prox1
CreERT2
Tamoxifen
Analysis
Week (Treatment)
1
2
3
4
C
Aqp1 fl/fl
AQP1 LYVE1
LYVE1
AQP1
Aqp1 iΔLEC
D
Blood vessel length
Lacteal length
Fraction
p=0.004
p=0.008
Aqp1 fl/fl
Aqp1 iΔLEC
0.6
0.4
0.2
0.0
0-40
40-60
60-80
80-100
Relative lacteal length interval (%)
E
-6h
0h
1h
2h
3h
Starvation
Blood sampling
Olive oil gavage
Aqp1 fl/fl
Aqp1 iΔLEC
p=0.01
Serum TG levels (mmol/l)
Time after oil gavage (hours)
F
-6h
-0.5h
0h
1h
2h
3h
Starvation
LPL inhibitor
Blood sampling
Olive oil gavage
Aqp1 fl/fl
Aqp1 iΔLEC
p=0.006
Plasma TG (mmol/L)
Time after oil gavage (hours)
G
(Treatment)
HFD
Week 1
2
3
4
5
Tamoxifen
Weight
Weight
Aqp1 fl/fl
Aqp1 iΔLEC
p=0.02
Weight gain (%)
Control
HFD
Diet

Figure 3

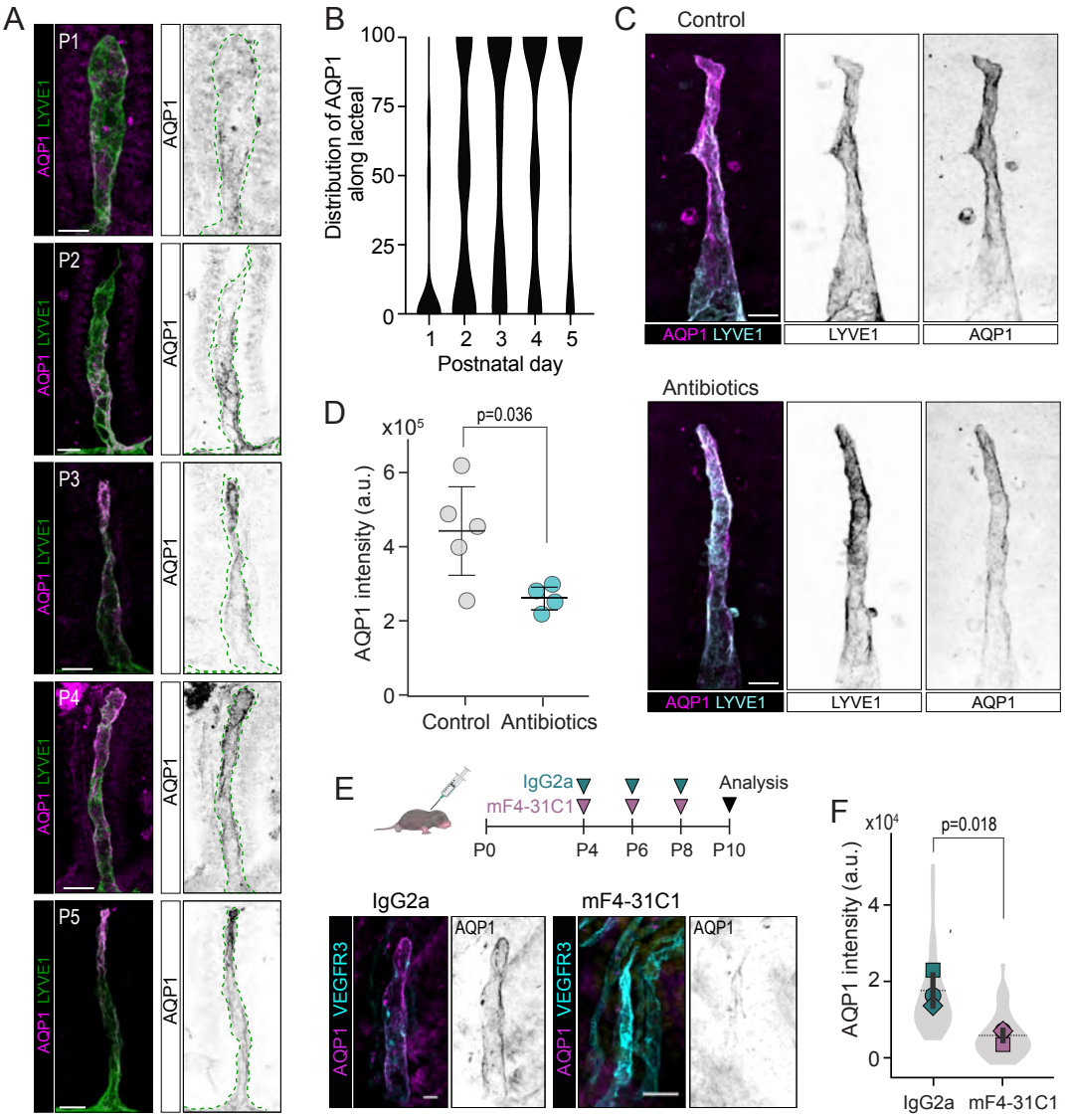
A
P1
P2
P3
P4
P5
AQP1 LYVE1
AQP1
B
Distribution of AQP1 along lacteal
100
75
50
25
0
1 2 3 4 5
Postnatal day
C
Control
AQP1 LYVE1
LYVE1
AQP1
Antibiotics
D
x10⁵
p=0.036
AQP1 intensity (a.u.)
6
4
2
0
Control Antibiotics
E
IgG2a
mF4-31C1
Analysis
P0 P4 P6 P8 P10
IgG2a
mF4-31C1
AQP1 VEGFR3
AQP1
F
x10⁴
p=0.018
AQP1 intensity (a.u.)
4
2
0
IgG2a mF4-31C1

Figure 4

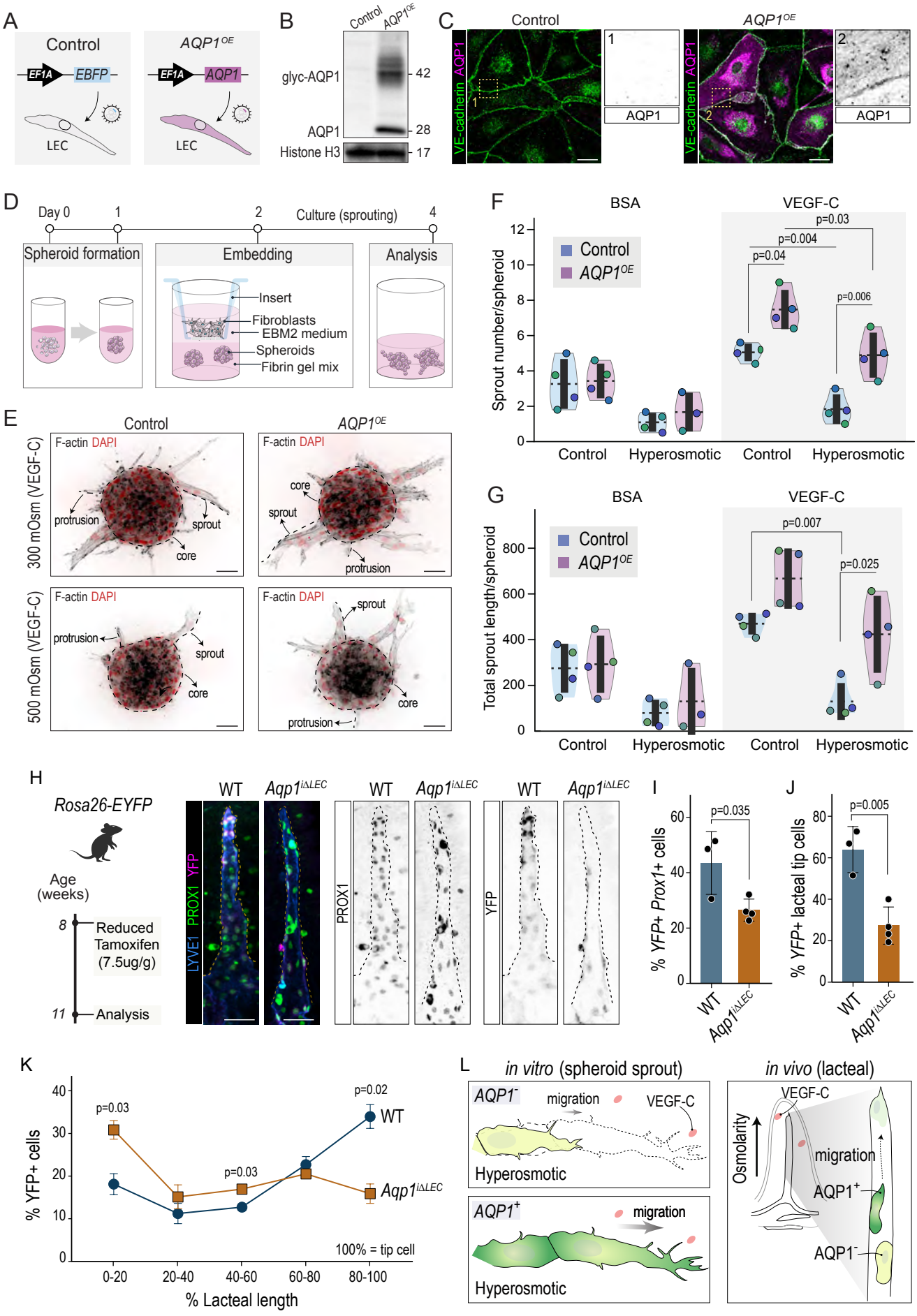
A
Control
AQP1OE
EF1A
EBFP
AQP1
LEC
B
Control
AQP1OE
glyc-AQP1
AQP1
Histone H3
42
28
17
C
Control
AQP1OE
VE-cadherin AQP1
AQP1
D
Day 0
1
2
Culture (sprouting)
4
Spheroid formation
Embedding
Analysis
Insert
Fibroblasts
EBM2 medium
Spheroids
Fibrin gel mix
E
Control
AQP1OE
300 mOsm (VEGF-C)
500 mOsm (VEGF-C)
F-actin DAPI
protrusion
sprout
core
F
BSA
VEGF-C
Control
AQP1OE
Sprout number/spheroid
p=0.03
p=0.004
p=0.04
p=0.006
Control
Hyperosmotic
G
BSA
VEGF-C
Total sprout length/spheroid
p=0.007
p=0.025
H
Rosa26-EYFP
Age (weeks)
8
Reduced Tamoxifen (7.5ug/g)
11
Analysis
WT
Aqp1iΔLEC
LYVE1 PROX1 YFP
PROX1
YFP
I
% YFP+ Prox1+ cells
p=0.035
J
% YFP+ lacteal tip cells
p=0.005
K
% YFP+ cells
p=0.03
p=0.02
p=0.03
WT
Aqp1iΔLEC
100% = tip cell
0-20
20-40
40-60
60-80
80-100
% Lacteal length
L
in vitro (spheroid sprout)
AQP1-
migration
VEGF-C
Hyperosmotic
AQP1+
migration
Hyperosmotic
in vivo (lacteal)
VEGF-C
Osmolarity
migration
AQP1+
AQP1-

Figure 5

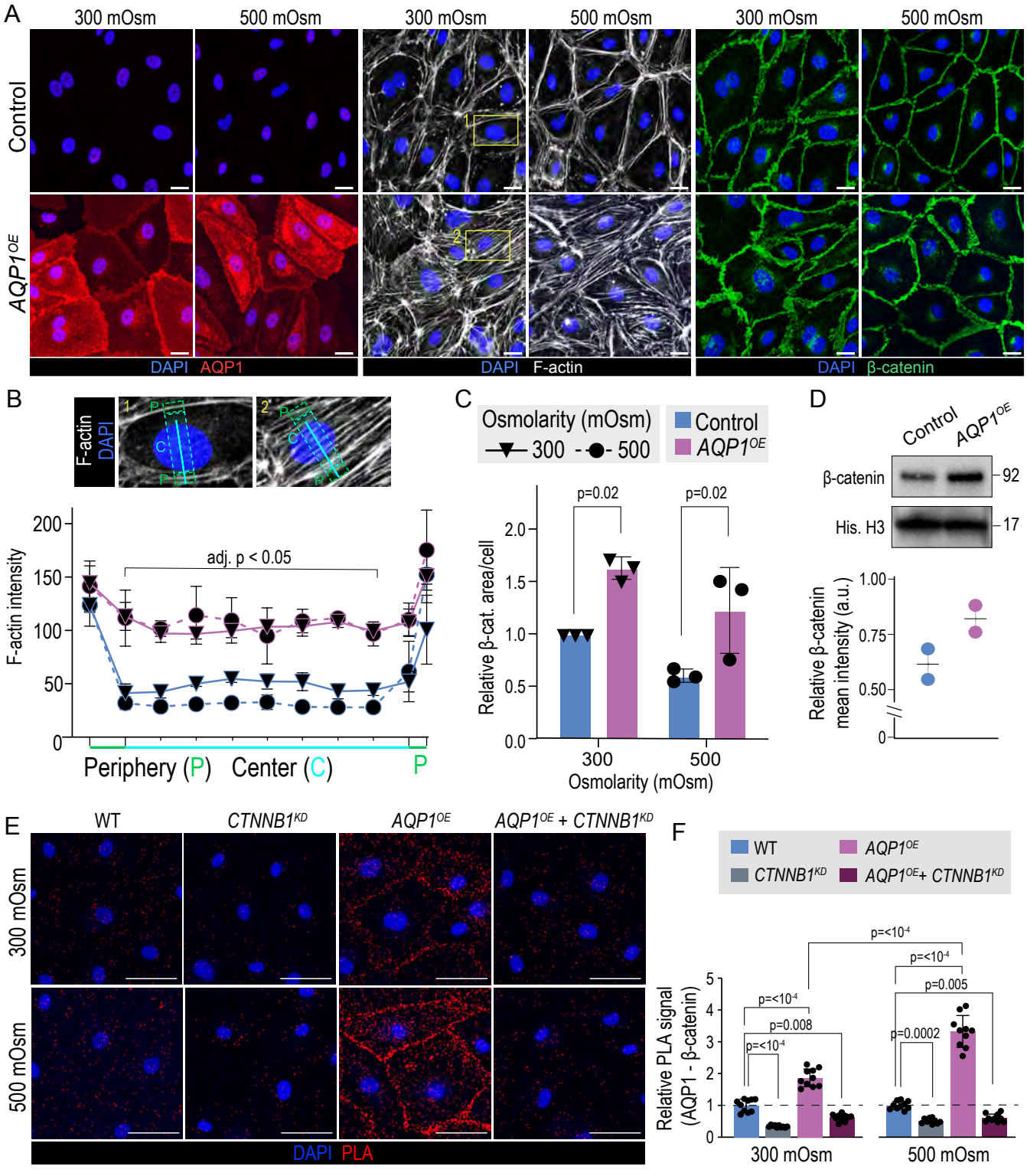
A
300 mOsm
500 mOsm
300 mOsm
500 mOsm
300 mOsm
500 mOsm
Control
AQP1OE
DAPI AQP1
DAPI F-actin
DAPI β-catenin
B
F-actin
DAPI
adj. p < 0.05
F-actin intensity
Periphery (P) Center (C) P
C
Osmolarity (mOsm)
300 500
Control
AQP1OE
p=0.02
p=0.02
Relative β-cat. area/cell
Osmolarity (mOsm)
D
Control
AQP1OE
β-catenin
92
His. H3
17
Relative β-catenin mean intensity (a.u.)
E
WT
CTNNB1KD
AQP1OE
AQP1OE + CTNNB1KD
300 mOsm
500 mOsm
DAPI PLA
F
WT
AQP1OE
CTNNB1KD
AQP1OE+ CTNNB1KD
p=<10-4
p=<10-4
p=0.005
p=<10-4
p=0.008
p=0.0002
p=<10-4
Relative PLA signal (AQP1 - β-catenin)
300 mOsm
500 mOsm

Figure 6

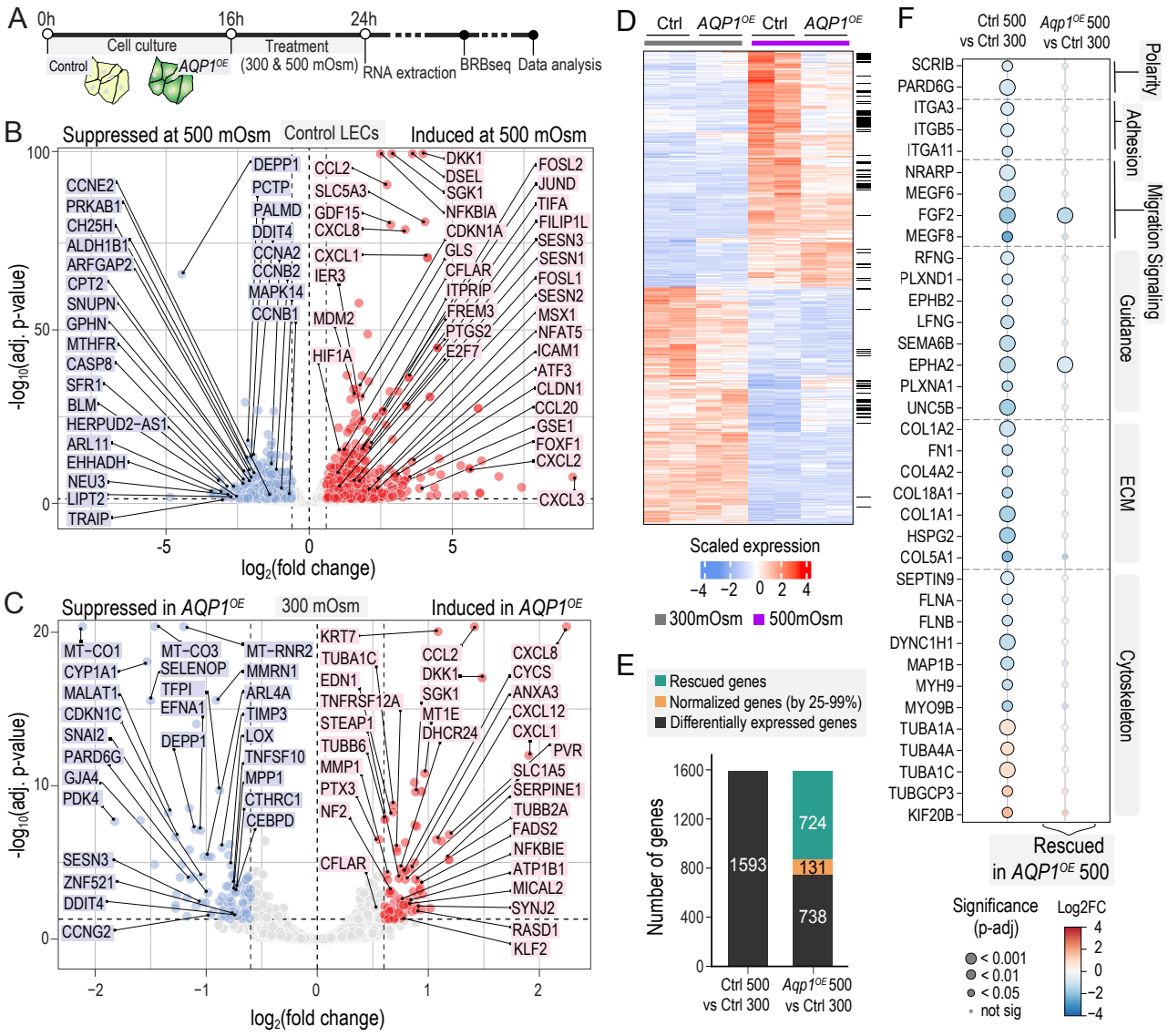
A
0h
16h
24h
Cell culture
Treatment
(300 & 500 mOsm)
Control
AQP1OE
RNA extraction
BRBseq
Data analysis
B
Suppressed at 500 mOsm
Control LECs
Induced at 500 mOsm
-log10(adj. p-value)
log2(fold change)
C
Suppressed in AQP1OE
300 mOsm
Induced in AQP1OE
-log10(adj. p-value)
log2(fold change)
D
Ctrl
AQP1OE
Ctrl
AQP1OE
Scaled expression
300mOsm
500mOsm
E
Rescued genes
Normalized genes (by 25-99%)
Differentially expressed genes
Number of genes
1593
724
131
738
Ctrl 500 vs Ctrl 300
Aqp1OE 500 vs Ctrl 300
F
Ctrl 500 vs Ctrl 300
Aqp1OE 500 vs Ctrl 300
Polarity
Adhesion
Migration Signaling
Guidance
ECM
Cytoskeleton
Rescued in AQP1OE 500
Significance (p-adj)
< 0.001
< 0.01
< 0.05
not sig
Log2FC

Figure 7

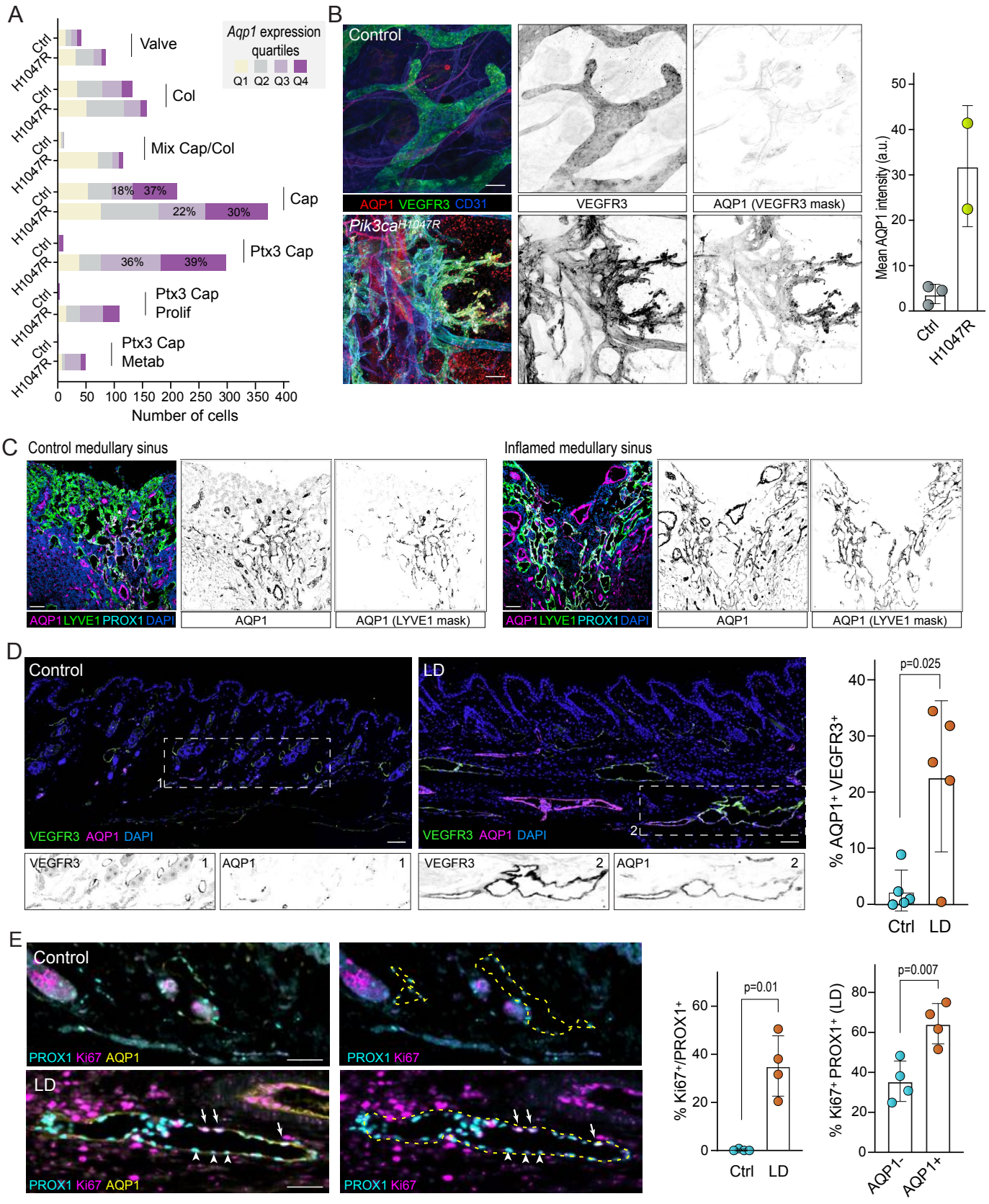
A
Aqp1 expression quartiles
Q1 Q2 Q3 Q4
Valve
Col
Mix Cap/Col
Cap
Ptx3 Cap
Ptx3 Cap Prolif
Ptx3 Cap Metab
Ctrl
H1047R
18%
37%
22%
30%
36%
39%
0 50 100 150 200 250 300 350 400
Number of cells
B
Control
Pik3ca H1047R
AQP1 VEGFR3 CD31
VEGFR3
AQP1 (VEGFR3 mask)
Mean AQP1 intensity (a.u.)
0 10 20 30 40 50
Ctrl
H1047R
C
Control medullary sinus
Inflamed medullary sinus
AQP1 LYVE1 PROX1 DAPI
AQP1
AQP1 (LYVE1 mask)
D
Control
LD
VEGFR3 AQP1 DAPI
1
2
VEGFR3
AQP1
% AQP1+ VEGFR3+
p=0.025
0 10 20 30 40
Ctrl LD
E
Control
LD
PROX1 Ki67 AQP1
PROX1 Ki67
% Ki67+/PROX1+
p=0.01
0 20 40 60
Ctrl LD
% Ki67+ PROX1+ (LD)
p=0.007
0 20 40 60 80
AQP1- AQP1+

Figure 8

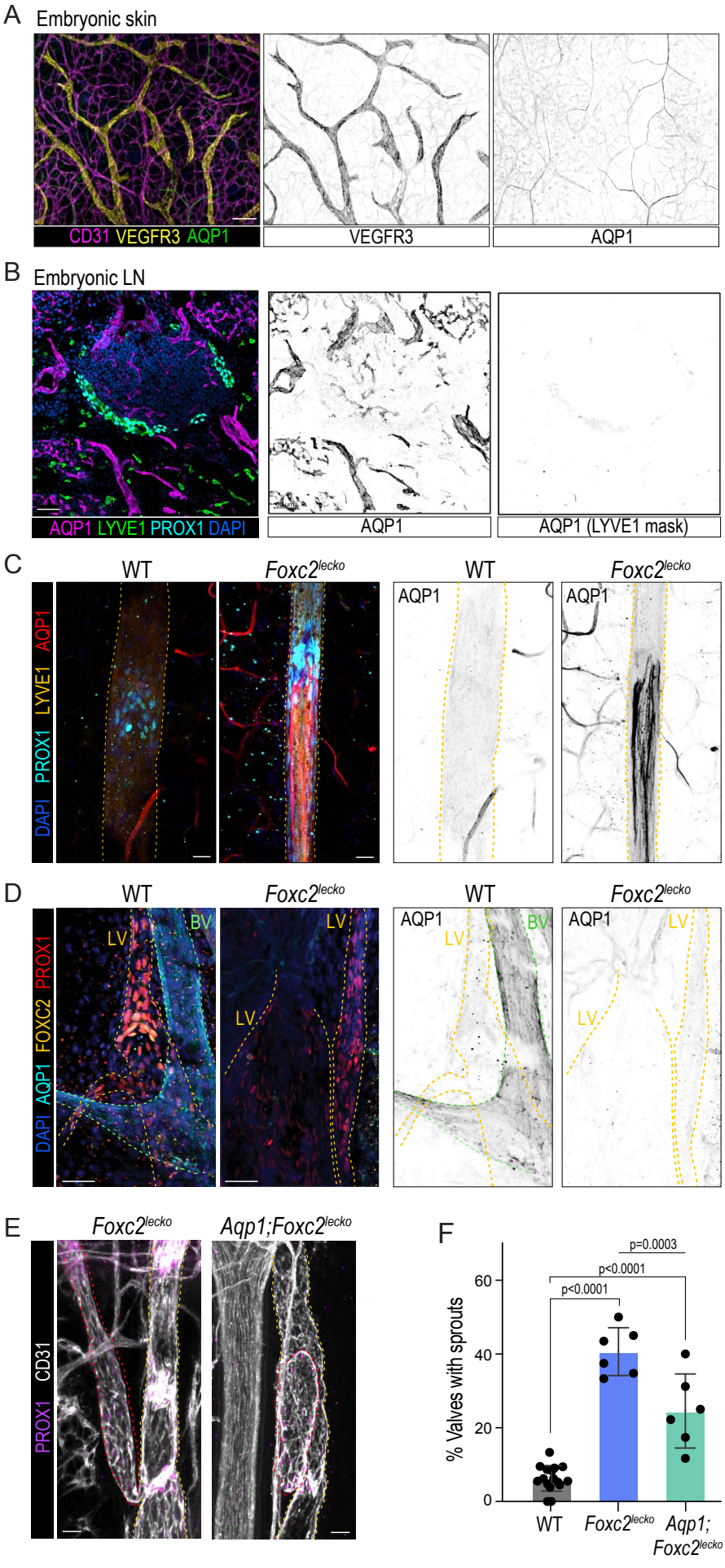
A
Embryonic skin
CD31 VEGFR3 AQP1
VEGFR3
AQP1
B
Embryonic LN
AQP1 LYVE1 PROX1 DAPI
AQP1
AQP1 (LYVE1 mask)
C
WT
Foxc2lecko
WT
Foxc2lecko
DAPI PROX1 LYVE1 AQP1
AQP1
AQP1
D
WT
Foxc2lecko
WT
Foxc2lecko
DAPI AQP1 FOXC2 PROX1
LV
BV
LV
AQP1
LV
BV
AQP1
LV
LV
LV
E
Foxc2lecko
Aqp1;Foxc2lecko
PROX1 CD31
F
p=0.0003
p<0.0001
p<0.0001
% Valves with sprouts
60
40
20
0
WT
Foxc2lecko
Aqp1; Foxc2lecko

Figure 9

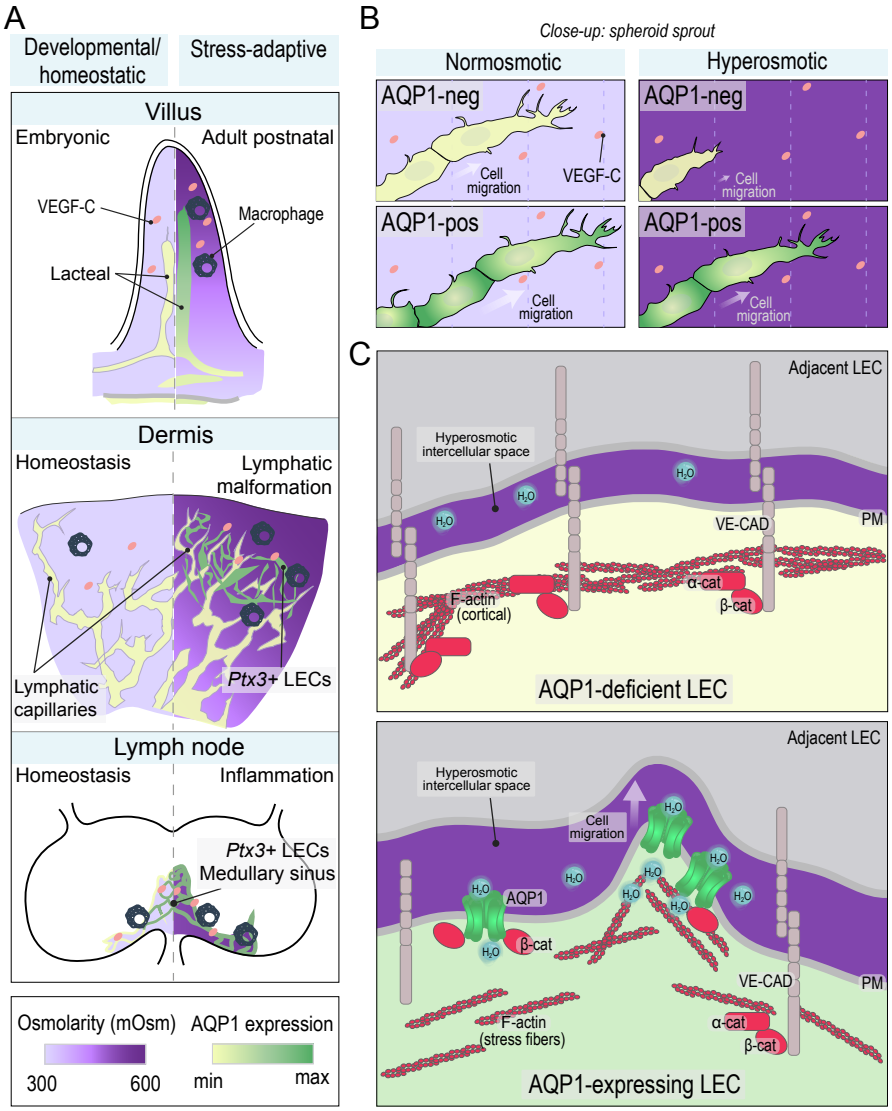
A
Developmental/ homeostatic
Stress-adaptive
Villus
Embryonic
Adult postnatal
VEGF-C
Macrophage
Lacteal
Dermis
Homeostasis
Lymphatic malformation
Lymphatic capillaries
Ptx3+ LECs
Lymph node
Homeostasis
Inflammation
Ptx3+ LECs
Medullary sinus
Osmolarity (mOsm)
300
600
AQP1 expression
min
max
B
Close-up: spheroid sprout
Normosmotic
Hyperosmotic
AQP1-neg
Cell migration
VEGF-C
AQP1-pos
C
Adjacent LEC
Hyperosmotic intercellular space
H2O
VE-CAD
PM
α-cat
β-cat
F-actin (cortical)
AQP1-deficient LEC
AQP1
F-actin (stress fibers)
AQP1-expressing LEC

Figure S1

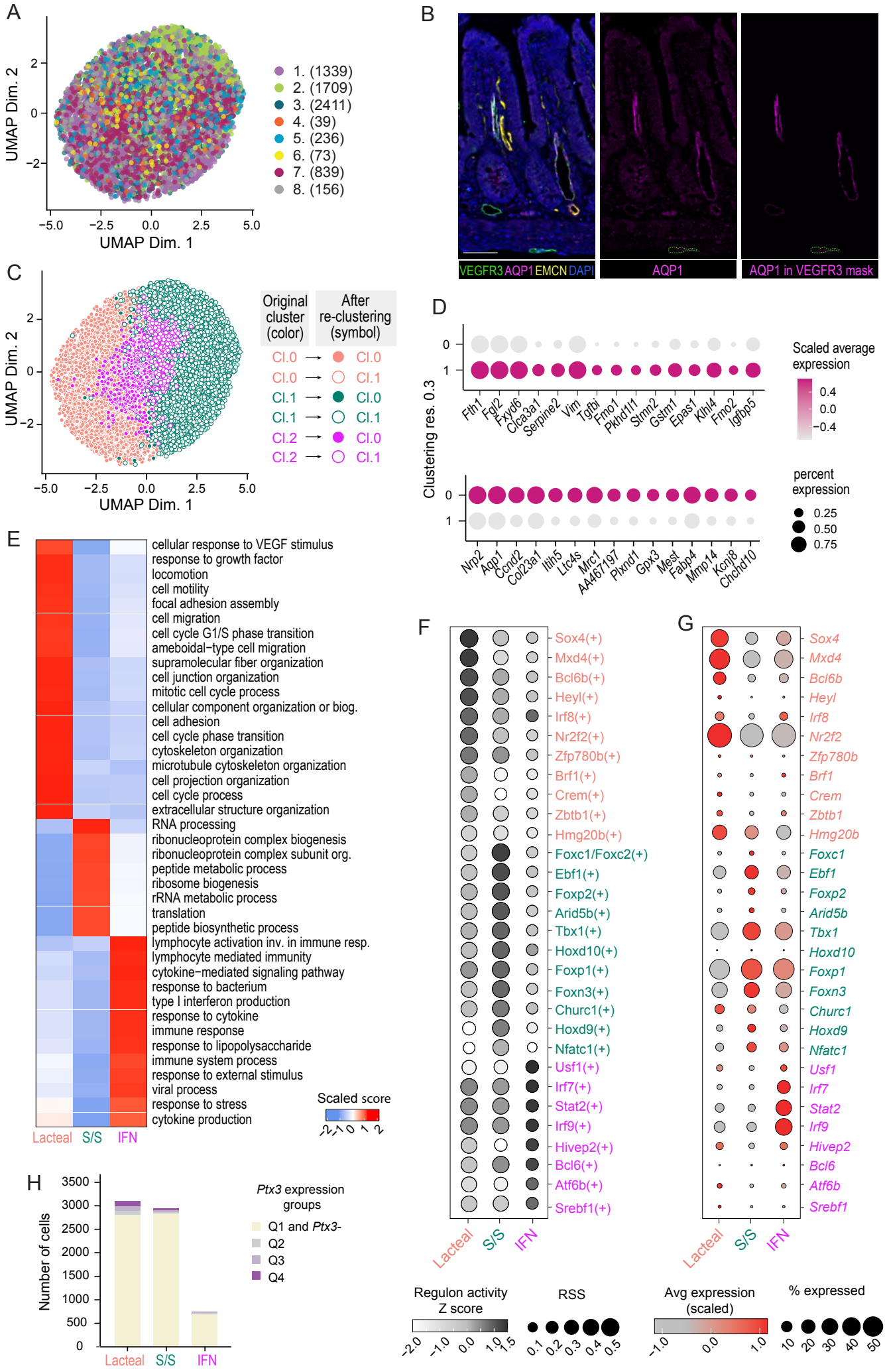
A
UMAP Dim. 2
UMAP Dim. 1
1. (1339)
2. (1709)
3. (2411)
4. (39)
5. (236)
6. (73)
7. (839)
8. (156)
B
VEGFR3 AQP1 EMCN DAPI
AQP1
AQP1 in VEGFR3 mask
C
Original cluster (color)
After re-clustering (symbol)
Cl.0 → Cl.0
Cl.0 → Cl.1
Cl.1 → Cl.0
Cl.1 → Cl.1
Cl.2 → Cl.0
Cl.2 → Cl.1
D
Clustering res. 0.3
Scaled average expression
percent expression
Fth1 Fgl2 Fxyd6 Clca3a1 Serpine2 Vim Tgfbi Fmo1 Pkhd1l1 Stmn2 Gstm1 Epas1 Klhl4 Fmo2 Igfbp5
Nrp2 Aqp1 Ccnd2 Col23a1 Itih5 Ltc4s Mrc1 AA467197 Plxnd1 Gpx3 Mest Fabp4 Mmp14 Kcnj8 Chchd10
E
cellular response to VEGF stimulus
response to growth factor
locomotion
cell motility
focal adhesion assembly
cell migration
cell cycle G1/S phase transition
ameboidal−type cell migration
supramolecular fiber organization
cell junction organization
mitotic cell cycle process
cellular component organization or biog.
cell adhesion
cell cycle phase transition
cytoskeleton organization
microtubule cytoskeleton organization
cell projection organization
cell cycle process
extracellular structure organization
RNA processing
ribonucleoprotein complex biogenesis
ribonucleoprotein complex subunit org.
peptide metabolic process
ribosome biogenesis
rRNA metabolic process
translation
peptide biosynthetic process
lymphocyte activation inv. in immune resp.
lymphocyte mediated immunity
cytokine−mediated signaling pathway
response to bacterium
type I interferon production
response to cytokine
immune response
response to lipopolysaccharide
immune system process
response to external stimulus
viral process
response to stress
cytokine production
Lacteal S/S IFN
Scaled score
F
Sox4(+)
Mxd4(+)
Bcl6b(+)
Heyl(+)
Irf8(+)
Nr2f2(+)
Zfp780b(+)
Brf1(+)
Crem(+)
Zbtb1(+)
Hmg20b(+)
Foxc1/Foxc2(+)
Ebf1(+)
Foxp2(+)
Arid5b(+)
Tbx1(+)
Hoxd10(+)
Foxp1(+)
Foxn3(+)
Churc1(+)
Hoxd9(+)
Nfatc1(+)
Usf1(+)
Irf7(+)
Stat2(+)
Irf9(+)
Hivep2(+)
Bcl6(+)
Atf6b(+)
Srebf1(+)
Lacteal S/S IFN
Regulon activity Z score
RSS
G
Sox4
Mxd4
Bcl6b
Heyl
Irf8
Nr2f2
Zfp780b
Brf1
Crem
Zbtb1
Hmg20b
Foxc1
Ebf1
Foxp2
Arid5b
Tbx1
Hoxd10
Foxp1
Foxn3
Churc1
Hoxd9
Nfatc1
Usf1
Irf7
Stat2
Irf9
Hivep2
Bcl6
Atf6b
Srebf1
Lacteal S/S IFN
Avg expression (scaled)
% expressed
H
Number of cells
Lacteal S/S IFN
Ptx3 expression groups
Q1 and Ptx3-
Q2
Q3
Q4

Figure S2

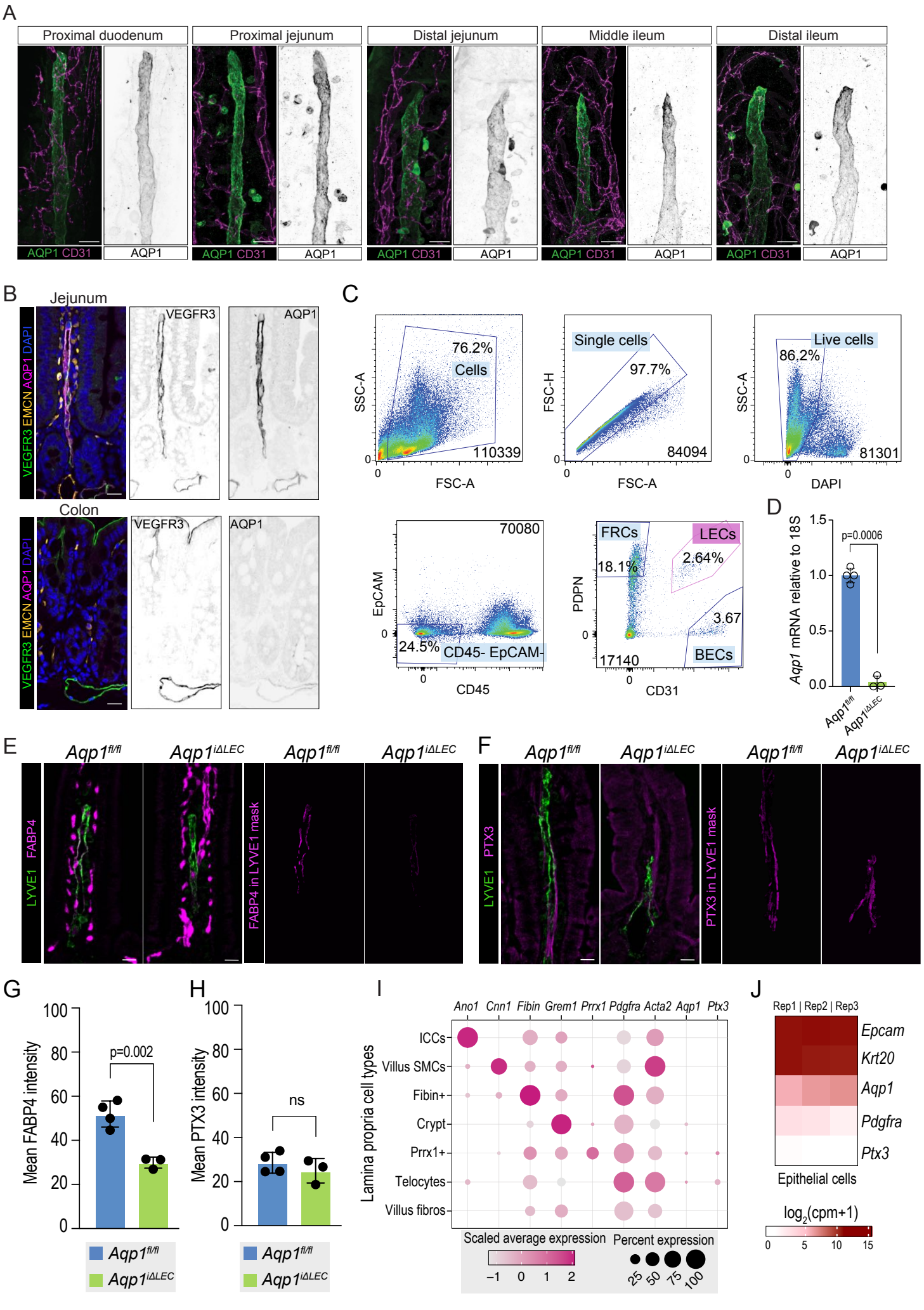
A
Proximal duodenum
Proximal jejunum
Distal jejunum
Middle ileum
Distal ileum
AQP1 CD31
AQP1
B
Jejunum
Colon
VEGFR3 EMCN AQP1 DAPI
VEGFR3
AQP1
C
76.2%
Cells
110339
SSC-A
FSC-A
Single cells
97.7%
84094
FSC-H
Live cells
86.2%
81301
DAPI
70080
EpCAM
24.5%
CD45- EpCAM-
CD45
FRCs
LECs
18.1%
2.64%
3.67
17140
BECs
PDPN
CD31
D
Aqp1 mRNA relative to 18S
p=0.0006
Aqp1fl/fl
Aqp1iΔLEC
E
Aqp1fl/fl
Aqp1iΔLEC
LYVE1 FABP4
FABP4 in LYVE1 mask
F
LYVE1 PTX3
PTX3 in LYVE1 mask
G
Mean FABP4 intensity
p=0.002
H
Mean PTX3 intensity
ns
I
Ano1 Cnn1 Fibin Grem1 Prrx1 Pdgfra Acta2 Aqp1 Ptx3
ICCs
Villus SMCs
Fibin+
Crypt
Prrx1+
Telocytes
Villus fibros
Lamina propria cell types
Scaled average expression
Percent expression
J
Rep1 | Rep2 | Rep3
Epcam
Krt20
Aqp1
Pdgfra
Ptx3
Epithelial cells
log2(cpm+1)

Figure S3

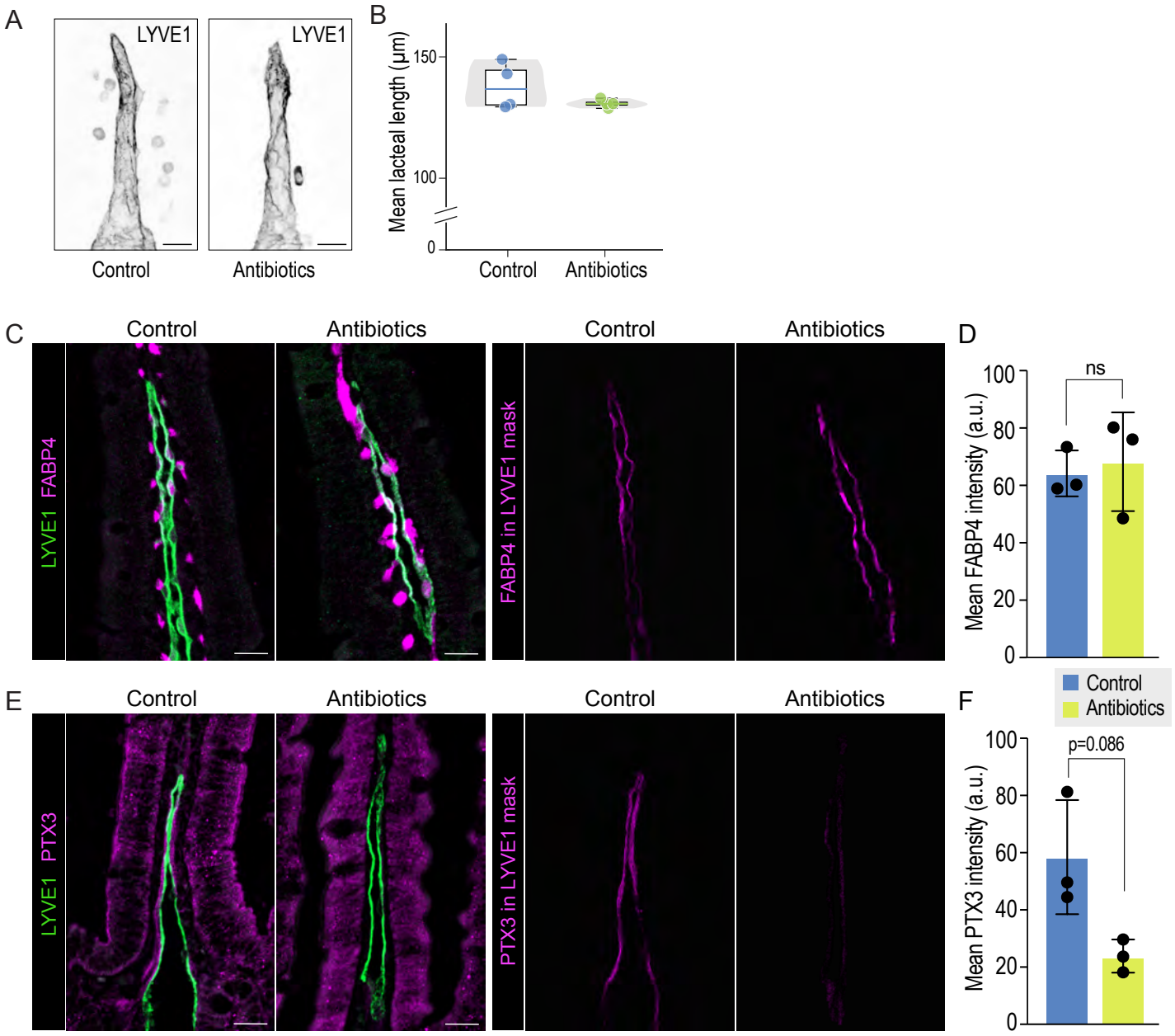
A
LYVE1
LYVE1
Control
Antibiotics
B
Mean lacteal length (µm)
150
100
0
Control
Antibiotics
C
Control
Antibiotics
Control
Antibiotics
LYVE1 FABP4
FABP4 in LYVE1 mask
D
Mean FABP4 intensity (a.u.)
100
80
60
40
20
0
ns
E
Control
Antibiotics
Control
Antibiotics
LYVE1 PTX3
PTX3 in LYVE1 mask
F
Control
Antibiotics
Mean PTX3 intensity (a.u.)
100
80
60
40
20
0
p=0.086

Figure S4

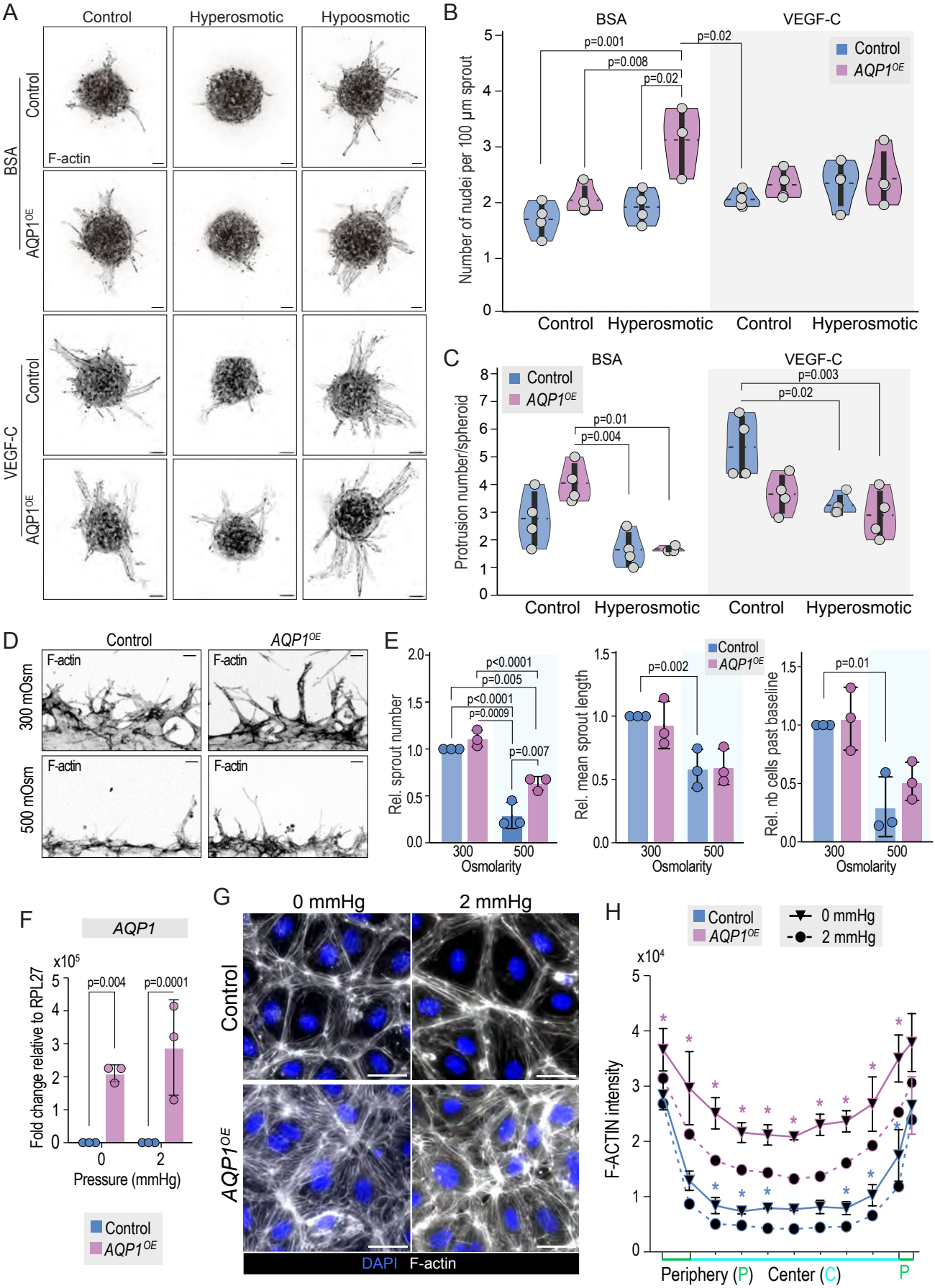
A
Control
Hyperosmotic
Hypoosmotic
BSA
Control
AQP1OE
F-actin
VEGF-C
Control
AQP1OE
B
BSA
VEGF-C
Control
AQP1OE
p=0.001
p=0.008
p=0.02
p=0.02
Number of nuclei per 100 µm sprout
Control
Hyperosmotic
Control
Hyperosmotic
C
BSA
VEGF-C
Control
AQP1OE
p=0.01
p=0.004
p=0.003
p=0.02
Protrusion number/spheroid
Control
Hyperosmotic
Control
Hyperosmotic
D
Control
AQP1OE
300 mOsm
500 mOsm
F-actin
E
p<0.0001
p=0.005
p<0.0001
p=0.0009
p=0.007
Rel. sprout number
Osmolarity
p=0.002
Rel. mean sprout length
p=0.01
Rel. nb cells past baseline
F
AQP1
x10^5
p=0.004
p=0.0001
Fold change relative to RPL27
Pressure (mmHg)
Control
AQP1OE
G
0 mmHg
2 mmHg
Control
AQP1OE
DAPI
F-actin
H
Control
AQP1OE
0 mmHg
2 mmHg
x10^4
F-ACTIN intensity
Periphery (P)
Center (C)
P